Near-wall Motion of Inertial Particles in Turbulent Channel Flows

by

Masoud Ebrahimian

A thesis submitted in partial fulfillment of the requirements for the degree of

Doctor of Philosophy

Department of Mechanical Engineering
University of Alberta

Abstract

Erosive wear due to particle–wall collision is an important challenge for slurry pipelines and solving this challenge requires a detailed understanding of particle motion near the wall. The complex phenomenology of the near-wall motion of particles in turbulent flows and the lack of a comprehensive theoretical or numerical approach to characterize it, highlight the need for experimental studies in this field. The objective of this research is to advance the current understanding of the near-wall motion of particles in turbulent flows and to study the effect of Reynolds number (Re), particle shape, size, and concentration on their motion using experimental methods. The analysis started with the investigation of particle dynamics and wall-collision in turbulent flows using Lagrangian particle tracking (LPT) techniques. It was found that the viscous forces decelerate near-wall particles in the streamwise direction, while the near-wall lift forces pushed the particles away from the wall. The change of Re affected the mean acceleration of particles and their collision with the wall. The effect of Re on particles acceleration reduced by increasing the distance from the wall. The analysis also showed the effect of particle size and shape on particles' dynamics and their collision with the wall. In addition, investigations showed that increasing the concentration of particles reduced their kinetic energy and acceleration in the streamwise direction while it increased these two parameters in the wall-normal direction. Finally, the motion of particles in a drag-reduced polymer solution was investigated. The results demonstrated the potential of polymer additives in reducing erosive wear in slurry pipelines.

Preface

The results from Chapter 5 of this thesis has been published in the *Journal of Fluid Mechanics* as

M. Ebrahimian, R. S. Sanders, and S. Ghaemi. Dynamics and wall collision of inertial particles in a solid–liquid turbulent channel flow. *J. Fluid Mech.*, 881:872–905, 2019.

The results from Chapter 8 of this thesis has been published in the *Experiments in Fluids* journal as

M. Ebrahimian, R. S. Sanders, and S. Ghaemi. Near-wall motion of inertial particles in a drag-reduced non-Newtonian turbulent flow. *Exp. Fluids*, 60:117, 2019.

All of the experiments, data analysis and interpretation of results of this thesis were performed by Masoud Ebrahimian.

Dedication

To my dear friend and brother, **Mohammad Mahdi Elyasi**,

the passenger of the paradise flight (PS752).

Acknowledgments

Foremost, I would like to express my gratitude and appreciation to the love of my life Maryam, for her encouragement and persistent care over the years. In the last four years, we have shared many joys and sorrows and hand in hand, we have overcome one challenge after another. Without her support and encouragement along the way, I wouldn't be able to make it. I learned courage, perseverance, and kindness from her and I am sure that side by side and with our love, we will successfully continue the adventurous journey of life.

I have to thank my dear parents Mahin and Mehdi for their love and support throughout my life. Thank you for giving me the strength to chase my dreams.

I also would like to thank my lifetime academic mentors Prof. Hassan Haddadpour and Dr. Mohammad Ali Noorian. From them, I learned humanity and the right way to respect others especially students, which will be the guide in my future professional academic career.

I am also thankful to my dear friends Dr. Mohammad Mohammadtabar and Farzad Ahmadi who supported me during my research. I also would like to thank my friends and colleagues Dr. Wagih Abu Rowin, Sadek Shaban, Dr. David Breakey, Dr. Reza Sabbagh, Lisa Kinsale, Reza Azadi, Dr. Hamidreza Karami and Dr. Bayode Owolabi for all of their help and support during my research.

I must thank the kind-hearted people of Canada who welcomed me and gave me the opportunity to study in this beautiful country. The people who supported me and my family in times of hardship and gave us hope. I learned from them that I must give others my honesty, respect, help, care, experience, passion, and hope. The more we give, the better world we have. Heather Good, Bert de Gier, and Dr. Iyad Alqishawi are some of these incredible people who we owe them a lot.

I also would like to thank Nora Lambrecht and Lubna Ahmad from the International Services Centre of the University of Alberta, and Shari Klassen from the Student Financial Support Center of the University of Alberta who helped my family a lot during difficult times.

Contents

List of Tables

List of Figures

Chapter 1

Introduction

1.1 Motivation

Slurry pipelines are economical and conventional means of material transportation (Neville et al., 2007; Parent and Li, 2013). The existence of inertial solid particles in the turbulent flows inside these pipelines increases the pressure drop (Wasp et al., 1977; Kaushal et al., 2005), requiring higher power to pump the mixture. In addition, the kinetic energy that the particles absorb from the carrier phase dissipates through their inelastic collision with the wall (Joseph et al., 2001) and other particles (Morgado and Oppenheim, 1997). The higher pumping power and erosive wear due to particle-wall collision are among the important remaining challenges of slurry pipelines (Karabelas, 1978; Kosel, 1992; Gupta et al., 1995).

To study the pipe erosion, we can investigate a piece of a pipe wall which has been exposed by particle-wall collision in a specific flow condition. The erosive wear rate of the pipe can be estimated by performing mass loss measurement (Ramesh et al., 2009). Scanning the sample using a microscope can reveal details about the erosion patterns (Alam et al., 2016; Okonkwo et al., 2016). These methods provide information about the resistance of pipe material against different types of wear mechanisms that can be helpful to modify the pipe material or predict its lifetime. However, they do not provide detailed information about the mechanism of particle-wall interaction. To understand the mechanism of particle-wall interaction, the motion of particles in the vicinity of the wall and the factors that affect it need to be investigated.

The dynamics of an inertial particle in a turbulent flow is different from the carrier phase due to its different inertia and is typically modeled by Maxey-Riley equation of motion (Maxey and Riley, 1983; Bec et al., 2006; Ireland et al., 2016a,b). In numerical approaches, for implementing the equation of motion, typically (not always) particles that are smaller than Kolmogorov length scale, η, and have large density ratio with respect to the fluid, r_ρ (e.g., Vreman 2007; Baker et al. 2017; Kasbaoui et al. 2019) are considered. In addition, the interaction of particles with each other and with the wall is either neglected (e.g., Cencini et al. 2006; Marchioli et al. 2008; Lavezzo et al. 2010; Salazar and Collins 2012) or assumed to be perfectly elastic (e.g., Sundaram and Collins 1997; Zamansky et al. 2011; Mehrabadi et al. 2018; Lee and Lee 2019). Moreover, particle shear-induced, rotation-induced, and wall-induced lift forces (known as Saffman, Magnus, and wall-repulsive forces, respectively) are typically neglected (e.g., Goswami and Kumaran 2010; Salazar and Collins 2012; Daitche 2015; Yu et al. 2016). The simulation of inertial particle motion in turbulent flows can be very costly and time consuming without considering these simplifications.

In many applications including slurry pipelines, however, particles are bigger than η, their r_ρ is on the order of unity (e.g. solid particles in liquid), and their interactions with each other and with the wall are not perfectly elastic. The particle lift forces are also important, particularly in near-wall turbulent flows where the velocity gradient is high (Soldati and Marchioli, 2009) and particle rotation is significant under the effect of shear flow (Jeffery, 1922) and particle-wall collision (Cherukat and McLaughlin, 1994).

The motion of a particle in a fluid has also been modeled using a numerical algorithm called interface-resolved DNS (Uhlmann, 2008; Costa et al., 2018, 2020). In this algorithm, the fluid motion is modeled using the continuity and Navier-Stokes equations. These equations are solved together with the Newton-Euler equations that govern the particle motion. The fluid and particle equations are coupled by the no-slip and no-penetration boundary conditions at the surface of the particle. The boundary of the particle is replaced by a force field defined on a number of mesh points following the immersed boundary method presented by Peskin (1972). Despite the recent achievements of the interface-resolved DNS

in modeling particle-laden turbulent flows, the implementation of this algorithm has been limited to a small fluid volume, low Re, and small number of particles immersed in the fluid due to its high computational cost. Therefore, experimental studies are still necessary not only to validate the numerical simulations, but also to investigate the characteristics of particle motion which are costly to find numerically, such as particle acceleration and their interaction with other particles and the wall.

1.2 Objectives

This thesis aims to improve our understanding of inertial particle motion in the near-wall region of particle-laden turbulent flows. In this regard, the distribution, velocity and acceleration of particles in turbulent flows, and their interaction with turbulence, other particles, and the wall will be investigated. The influence of important factors including Re, the size, shape, and concentration of particles, and the fluid rheology on these interactions also will be studied.

1.3 Thesis overview

This thesis contain nine chapters and the rest of it is organized as follows:

- Chapter 2 provides the essential background and basic concepts about the turbulence and particle interaction with turbulence, other particles, and the wall.
- Chapter 3 describes the experimental setup used for performing the experiments of this thesis. The chapter includes a discussion of the flow facility, the carrier fluid, the flow tracers, and the inertial particles.
- Chapter 4 explains the measurement systems used in this thesis including two- and three-dimensional LPT systems, the rheometer, and the pressure measurement system. The data processing steps and the uncertainty of the LPT systems are also discussed in this chapter.

- Chapter 5 advances the current understanding of particle dynamics and wall collision in a near-wall turbulent flow. The velocity and acceleration of particles are measured and the contribution of the turbulent motions that affect particle dynamics are discussed.

- Chapter 6 investigates the effect of Re and particle concentration on distribution, velocity, and acceleration of particles and their interaction with the wall and other particles.

- Chapter 7 compares the near-wall motion of spherical and non-spherical particles in a turbulent flow and investigates the effect of particle size on the velocity and acceleration statistics of particles and their interaction with the wall.

- Chapter 8 examines the effect of a polymer drag reducer on particle kinematics in near-wall turbulent flows and discusses its potential in reducing erosive wear in particle-laden pipelines. Polymers with large molecular weight are well known to be effective in reducing drag and pumping power in unladen turbulent liquid flow (Virk et al., 1970; Luchik and Tiederman, 1988; Warholic et al., 1999). However, their effect on the kinematics of particles in turbulent flows is not known yet.

- Chapter 9 summarizes the conclusions of this thesis and discusses proposed future studies.

Chapters 5 to 8 include the introduction, experimental design, and the discussion necessary to follow their corresponding objectives.

Chapter 2

Background

This chapter provides the required background to understand the physics governing the motion of a particle in a turbulent flow. The first part of this chapter starts with the fundamental equations of fluid dynamics, i.e. the continuity and the Navier-Stokes equations, followed by describing the flow classification based on the Reynolds number and explaining laminar and turbulent flows. Next, the fundamental concept of turbulence, i.e. the cascade of energy, and the Kolmogorov time and length scales are briefly discussed. The specifications of turbulent channel flow are explained afterward along with the associated continuity and Navier-Stokes equations. In the second part of this chapter, the governing equation for the motion of a particle in a fluid, i.e. Maxey-Riley equation, is presented and its limitations are explained. Finally, the motion of particles in particle-laden turbulent channel flows is discussed, reviewing the numerical and experimental investigations on the interaction of particles with turbulence, other particles, and the wall. The first part of this chapter is mainly adapted from Çencel and Cimbala (2006), Pope (2000), and Chen et al. (2010) and the theoretical background of the second part of this chapter is mostly based on Crowe et al. (2012).

2.1 Fluid dynamics

The dynamics of fluid is governed by the fundamental principles of classical physics: the conservation of mass and the conservation of momentum. The conservation of mass implies

that the change of the mass of a closed fluid volume in a given time must be equal to the mass that passes through its boundaries, resulting in the continuity equation in fluid dynamics expressed as

$$\frac{\partial \rho_f}{\partial t} + \nabla \cdot (\rho_f \mathbf{U}_f) = 0, \tag{2.1}$$

where ρ_f is the fluid density, t is time, $\mathbf{U}_f$ is the fluid instantaneous velocity vector, and ∇ is the gradient operator.

The principle of momentum conservation dictates that the momentum of a closed fluid volume must remain constant over time when it is not affected by external loads. Based on Newton's second law, the rate of change of momentum of the fluid volume is equal to the resultant force applied to it. In fluid dynamics, Newton's second law and the principle of momentum conservation are applied through the Navier-Stokes equation presented as

$$\frac{\partial \mathbf{U}_f}{\partial t} + \mathbf{U}_f \cdot \nabla \mathbf{U}_f = \frac{-\nabla p}{\rho_f} + \nu \nabla^2 \mathbf{U}_f + \frac{\mathbf{F}}{\rho_f}, \tag{2.2}$$

where p is the instantaneous pressure, ν is the fluid kinematic viscosity, and $\mathbf{F}$ represents the vector of body forces.

The ratio between the inertial forces to the viscous forces is known as Reynolds number, Re. At a low Re the viscous forces dominate the Navier-Stokes equation, resulting in stable flow streamlines. This type of flow is known as a laminar flow. At a high Re, the inertial forces become dominant and cause perturbations in the flow. These perturbations are not completely damped by the viscous forces and make the flow chaotic. This type of flow is called a turbulent flow.

2.1.1 Turbulent flow

A turbulent flow consists of swirling fluid elements, known as "eddy", with different sizes. The size of the largest eddy in a turbulent flow is on the order of the largest dimension of the flow boundaries. Due to the unstable nature of turbulence, the large eddies break up into smaller eddies and this procedure continues until the eddies become small enough that the

viscous forces can dissipate their energy into heat. This concept is known as the "cascade of energy" in turbulent flows which was introduced by Kolmogorov (1941a,b). Based on Kolmogorov's theory, the smallest scale in turbulent flows can be determined using the scale of the eddies with $Re = 1$. Considering ϵ to be the amount of energy transferred from the largest eddies to the smallest eddies per unit mass and unit time, the smallest length scale in turbulence, known as Kolmogorov length scale, is defined as $\eta = (\nu/\epsilon)^{1/4}$. Based on this concept, the Kolmogorov time scale is defined as $t_\eta = \sqrt{\nu/\epsilon}$. In this thesis, the variables that are nondimensionalized using the Kolmogorov scales are denoted by the subscript 'η'.

2.1.2 Turbulent channel flow

An internal flow between parallel plates, as seen in figure 2.1, is called channel flow. Figure 2.1 presents the schematic of a channel with a rectangular cross-section of $Wi \times 2H$, along with the coordinate system located at the channel entrance showing the positive streamwise, x, wall-normal, y, and spanwise, z, directions. The components of the instantaneous velocity vector of the flow in the x, y, and z directions are represented by U, V, and W, respectively. The Re for a channel flow is typically defined as

$$Re_H = \frac{2\rho_f U_b H}{\mu}, \tag{2.3}$$

where U_b is the flow bulk velocity, μ is the fluid dynamic viscosity, and H is the channel half-height. A channel flow with $Re_H > 4000$ is typically considered turbulent with no transitional effect.

In a turbulent channel flow, the mean velocity profile is independent of x when $(x/H) > 180$ (Coulson et al., 1999), known as fully developed turbulent flow. The mean velocity profile is also independent of z and the flow is two-dimensional in the $x - y$ plane when $(Wi/H) > 14$ (Vinuesa et al., 2014). In a fully developed two-dimensional turbulent channel flow, the mean streamwise velocity, $\langle U \rangle$ (where $\langle\ \rangle$ is the ensemble average operator over time), is maximum at the center-line, i.e. $y = H$, and gradually reduces to zero at the walls due to the no-slip boundary condition.

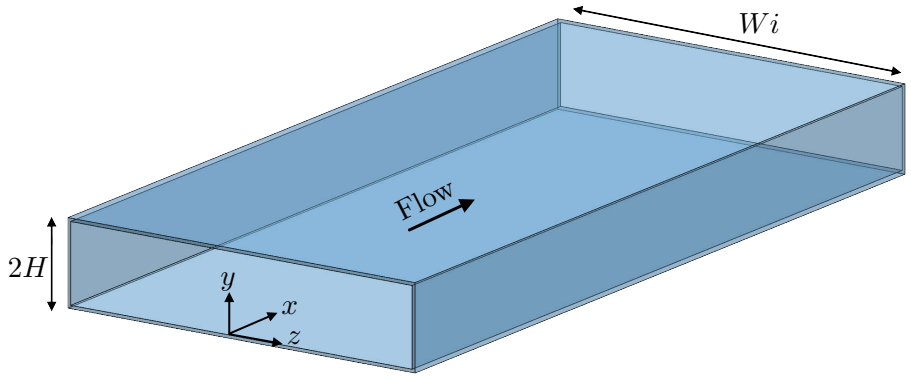

Figure 2.1: Schematic of a channel with a rectangular cross-section. The flow moves in the x direction.

The mean velocity profile between the wall and the channel center-line can be divided into four layers including viscous sublayer, buffer layer, log layer, and the outer layer. In the first layer next to the wall, the viscous sublayer, viscous forces are dominant. In this layer the wall-normal gradient of the mean streamwise velocity, i.e. $\partial\langle U\rangle/\partial y$, is constant. The viscous shear stress at the wall can be calculated based on the $\partial\langle U\rangle/\partial y$ in this layer as $\tau_w = \mu\partial\langle U\rangle/\partial y$. The τ_w can be used to determine a scaling velocity for the flow that is known as friction velocity and calculated as $u_\tau = \sqrt{\tau_w/\rho_f}$. Based on the u_τ, one can determine a scaling length and time for the flow as $\lambda = \nu/u_\tau$ and $t_\tau = \nu/u_\tau^2$, respectively. In turbulent channel flow studies, variables are normalized by u_τ, λ and t_τ (known as inner scaling) and denoted by the superscript '+'. The Reynolds number is also defined based on the friction velocity as $Re_\tau = u_\tau H/\nu$. The width of the viscous sublayer extends from the wall up to $y^+ \sim 5$, where $y^+ = y/\lambda$. In this layer, $U^+ = y^+$, where $U^+ = \langle U\rangle/u_\tau$. Beyond the viscous sublayer, the $\partial\langle U\rangle/\partial y$ is not constant anymore and it is a function of wall-normal location and fluid properties. At the buffer layer, $5 < y^+ < 35$, both viscous and inertial forces have a significant effect on the flow motion and provide large turbulence in this region. Farther from the wall in the log and outer layers ($y^+ > 35$), the contribution of viscous forces is significantly smaller than the inertial forces. In the log-layer, the U^+ has a logarithmic relationship with y^+ as $U^+ = \ln(y^+)/\kappa + B$, where κ is known as the von Kármán constant and B is the intercept of the log-layer velocity profile. For a Newtonian

turbulent boundary layer, $\kappa = 0.41$ and $B = 5.2$.

Due to the statistical homogeneity in the x and z directions and based on the no-penetration boundary condition at the walls, the continuity equation for a two-dimensional, fully developed, incompressible, steady turbulent channel flow results in $\langle V \rangle = 0$ and $\langle W \rangle = 0$, showing that the mean wall-normal and spanwise velocities of the flow are zero. The Navier-Stokes equation for this flow can be rewritten as

$$\mathbf{A}_f \equiv \frac{\partial \mathbf{U}_f}{\partial t} + \mathbf{U}_f \cdot \nabla \mathbf{U}_f = \frac{\nabla p}{\rho_f} + \nu \nabla^2 \mathbf{U}_f, \tag{2.4}$$

where $\mathbf{A}_f$ is the instantaneous acceleration vector of the flow. The instantaneous velocity vector can be decomposed into mean and fluctuating components based on the Reynolds decomposition as $\mathbf{U}_f = \langle \mathbf{U}_f \rangle + \mathbf{u}_f$, where $\mathbf{u}_f = [u, v, w]$ is the fluctuating velocity vector and u, v, and w are the fluctuating velocity components in x, y, and z directions, respectively. Using the decomposed velocity vector and the ensemble average operator, one can write the average of Equation 2.4 as

$$\langle \mathbf{A}_f \rangle \equiv \langle \mathbf{u}_f \cdot \nabla \mathbf{u}_f \rangle = \frac{-\nabla \langle p \rangle}{\rho_f} + \nu \nabla^2 \langle \mathbf{U}_f \rangle. \tag{2.5}$$

Equation 2.5 shows that the average acceleration of the turbulent channel flow is decomposed into a pressure-gradient term, $-\nabla \langle p \rangle / \rho_f$, known as irrotational acceleration and a viscous term, $\nu \nabla^2 \langle \mathbf{U}_f \rangle$, referred to as solenoidal acceleration. Based on Equation 2.5, the mean acceleration of a two-dimensional, fully developed, incompressible, steady turbulent channel flow in the streamwise, $\langle A_x \rangle$, wall-normal, $\langle A_y \rangle$, and spanwise, $\langle A_z \rangle$, directions are

$$\langle A_x \rangle \equiv \frac{\partial \langle uv \rangle}{\partial y} = \frac{-\partial \langle p \rangle}{\rho_f \partial x} + \nu \frac{\partial^2 \langle U \rangle}{\partial y^2}, \tag{2.6a}$$

$$\langle A_y \rangle \equiv \frac{\partial \langle v^2 \rangle}{\partial y} = \frac{-\partial \langle p \rangle}{\rho_f \partial y}, \tag{2.6b}$$

$$\langle A_z \rangle \equiv \frac{\partial \langle vw \rangle}{\partial y} = 0. \tag{2.6c}$$

Hereafter, the $\langle\ \rangle$ operator shows the average of the associated parameter in the streamwise and spanwise directions as well as in time.

2.2 Spherical particle motion in fluid

Stokes (1851) presented the first equation of motion for a point-like spherical particle moving in a creeping flow, i.e. a flow with $Re \ll 1$, as

$$m_p \frac{d\mathbf{U}_p}{dt} = 3\pi d_p \mu (\mathbf{U}_{f,p} - \mathbf{U}_p), \tag{2.7}$$

where m_p is the particle mass, d_p is the particle diameter, $\mathbf{U}_p$ is the particle velocity vector at the time t, and $\mathbf{U}_{f,p}$ is the fluid velocity vector at the particle location at the time t. The right-hand side term of Equation 2.7 is called the Stokes drag force. For the motion of a particle falling through a quiescent viscous fluid under gravity, Equation 2.7 is rewritten as

$$m_p \mathrm{g} = 3\pi d_p \mu V + m_f \mathrm{g}, \tag{2.8}$$

where g is the gravitational acceleration, V is the particle velocity, m_f is the mass of the fluid displaced by the particle and m_fg is the buoyancy force. For a particle with the density of ρ_p, Equation 2.8 can be solved for V as

$$V = t_p \mathrm{g}, \tag{2.9}$$

where t_p is known as particle response time and defined as

$$t_p = \frac{(\rho_p - \rho_f) d_p^2}{18\mu}. \tag{2.10}$$

The maximum velocity that is attainable for a particle falling through a quiescent fluid is known as its terminal settling velocity, V_t. For a spherical particle falling through a Newtonian fluid, V_t is calculated as

$$V_t = \sqrt{\frac{4\mathrm{g} d_p (\rho_p - \rho_f)}{3\rho_f C_d}}, \tag{2.11}$$

where C_d is the drag coefficient of the particle. The drag coefficient can be estimated using the particle Reynolds number calculated based on V_t. The particle Reynolds number based on V_t in a Newtonian fluid is defined as

$$Re_{pt} = \frac{V_t d_p}{\nu}. \tag{2.12}$$

In the literature, the particle Reynolds number is also defined based on its slip velocity with respect to the surrounding fluid, U_s, as

$$Re_{ps} = \frac{U_s d_p}{\nu}. \tag{2.13}$$

The terminal settling velocity is also used to calculate the Rouse number, Ro, a non-dimensional number that describes the transportation of particles in a flow (Rouse, 1937). The Rouse number determines the balance between settling velocity of a particle and its suspension by turbulence and is calculated as

$$Ro = \frac{V_t}{\kappa u_\tau}. \tag{2.14}$$

Since 1851, several studies have tried to extend the application of the particle equation of motion and capture the effect of different forces applied to a particle moving in a fluid (e.g. Basset 1888; Boussinesq 1903; Faxén 1922; Oseen 1927; Corrsin and Lumley 1956). Maxey and Riley (1983) derived the equation of motion for a point-like spherical particle moving in a creeping flow as

$$\begin{aligned} m_p \frac{d\mathbf{U}_p}{dt} = 3\pi\mu d_p(\mathbf{U}_{f,p} - \mathbf{U}_p) + m_f \frac{D\mathbf{U}_{f,p}}{Dt} + \frac{m_f}{2}\left(\frac{D\mathbf{U}_{f,p}}{Dt} - \frac{d\mathbf{U}_p}{dt}\right) \\ +(m_p - m_f)\mathbf{g} + \frac{3d_p^2\rho_f\sqrt{\pi\nu}}{2}\int_0^t \left(\frac{d(\mathbf{U}_{f,p} - \mathbf{U}_p)}{ds}\right)\frac{ds}{\sqrt{t-s}}, \end{aligned} \tag{2.15}$$

where D/Dt is the material derivative operator. Equation 2.15 is known as Maxey–Riley equation. The second term on the right-hand side of this equation represents the force applied to the particle by the undisturbed flow (also known as pressure gradient force) that is equivalent to the acceleration of the fluid element located at the position of the particle. The third term is known as the added mass and represents the force that is applied to the

particle due to the acceleration of the surrounding fluid when the particle moves. The fourth term is the buoyancy force and the last term is known as the Basset force that accounts for the time delay in the boundary layer development with changing the slip velocity of the particle. The point-particle model used for driving the Maxey–Riley equation is based on the assumption that this equation can perfectly model the perturbation of the flow around a moving particle (Maxey and Riley, 1983; Auton et al., 1983, 1988). This assumption is valid when the length scale of the eddies in the flow is larger than the particle size and $Re_{ps} \ll 1$.

Despite the contribution of several studies in extending the application of Maxey–Riley equation to finite-size spherical particles using Faxén corrections (e.g. Calzavarini et al. 2009) and to finite Reynolds numbers (e.g. Mei et al. 1991; Mei and Adrian 1992; Kim et al. 1998), results of simulations based on this equation still have some discrepancies with experimental investigations (Volk et al., 2008). For example, experimental studies of Voth et al. (2002) and Qureshi et al. (2007, 2008) in homogeneous isotropic turbulence (a turbulent flow far away from physical boundaries that the average of its properties, including pressure, velocity and acceleration statistics, are independent of position and direction) showed that the profile of probability density function (pdf) of particles acceleration normalized by the root-mean-square (rms) of their acceleration was not significantly dependent on $d_\eta = d_p/\eta$ and it could be fitted with an exponential function. However, the numerical simulation of particle motion based on Maxey–Riley equation corrected for finite-size particles by Calzavarini et al. (2009) showed that the tails of the normalized pdf of particles acceleration became narrower by increasing d_η.

The restrictions of the Maxey–Riley equation are not limited to the discrepancies of its results with the experimental findings. This equation only considers the effect of the flow on the particle and does not account for the effect of the particle on the flow. It also does not consider the particle lift forces including Saffman (due to pressure distribution on the particle) and Magnus (due to particle rotation) forces, which are known to be important for large particles in turbulent flows (Rubinow and Keller, 1961; Saffman, 1965; Kim and

Balachandar, 2012; Meller and Liberzon, 2015). In addition, the effect of particle interaction with the other particles and the physical boundaries of the flow on its motion is not considered in the Maxey–Riley equation. Besides all of these limitations, the implementation of Maxey–Riley equation for simulating the particle motion in a turbulent flow is computationally costly due to its complexities, specifically for large particles and using Faxén corrections. To reduce its complexities, simplified versions of Equation 2.15 are typically used in numerical approaches by simulating the motion of particles with $d_\eta \ll 1$ and $r_\rho \gg 1$, as discussed in section 1.1. However, these simplifications cannot be implemented for large particles with $r_\rho \sim \mathcal{O}(1)$, which are common in slurry pipelines. Therefore, to better model particle motion in turbulent flows and support the continued development of numerical approaches, high-quality experimental data of particle dynamics for such flows are required.

2.2.1 Spherical particle motion in particle-laden turbulent flow

The motion of a particle in a particle-laden turbulent channel flow depends on its interaction with turbulence, other particles, and the walls. These interactions are discussed in this section in the form of a brief literature review to summarize the current understanding of them.

2.2.1.1 Particle-turbulence interaction

In most previous studies, particle-turbulence interaction (PTI) has been characterized based on Stokes number, St, which is the ratio of t_p to the flow time scale. This number represents a comparison between the particle inertia and the viscous force in the flow. In the literature, St has been estimated in different ways, depending on the flow characteristic time used for its estimation. The St based on the characteristic time of energy-containing eddies, $t_e = l_e/u_e$, is defined as

$$St_e = \frac{t_p}{t_e}, \tag{2.16}$$

where l_e and u_e are the characteristic length and velocity of the eddies, respectively. The t_e can be roughly estimated as $t_e \approx \kappa t_\tau y^+$ (Tennekes and Lumley, 1972; Righetti and Romano,

2004). The Stokes number is also estimated based on the inner time-scale of the flow as

$$St^{+} = \frac{t_p}{t_\tau}, \tag{2.17}$$

or based on the Kolmogorov time scale as

$$St_\eta = \frac{t_p}{t_\eta}. \tag{2.18}$$

Although the St has been widely used in the literature to characterize PTI, some studies have argued that the interaction of finite-size particles with turbulence cannot be described by St only and the contribution of d_η and r_ρ must be simultaneously considered (e.g. Qureshi et al. 2007, 2008).

Particles with $St \ll 1$, can preferentially respond to fluid fluctuations. This mechanism is known as preferential sampling. Previous numerical investigations for sub-Kolmogorov spherical particles with large r_ρ showed that due to the preferential sampling mechanism, particles with small St have a higher kinetic energy compared to the particles with large St (Salazar and Collins, 2012; Ireland et al., 2016a) since they can follow eddies with high turbulent kinetic energy (Squires and Eaton, 1991). Salazar and Collins (2012) showed that for particles with $St < 0.2$, the kinetic energy of particles was even larger than the fluid and increased with increasing St. For $St > 0.2$, increasing the St reduced the ratio of particles kinetic energy to fluid kinetic energy (Salazar and Collins, 2012; Ireland et al., 2016a). Qureshi et al. (2008) argued that the effect of preferential sampling on a particle motion attenuates when the particle is bigger than the characteristic size of the active regions of the flow, which is 10 to 20 times bigger than η (Aliseda et al., 2002).

When St of a particle is on the order of unity or larger, its interaction with turbulence is affected by its inertia; it only responds to energetic flow turbulence and filters out the low energy eddies (Bec et al., 2006; Ayyalasomayajula et al., 2008). Particles with higher inertia typically have lower kinetic energy (Salazar and Collins, 2012) and lower acceleration (Ireland et al., 2016a) than particles with lower inertia. The numerical investigations of Zaichik and Alipchenkov (2008) and Ireland et al. (2016a) for sub-Kolmogorov spherical particles with large r_p in isotropic turbulence showed the reduction of acceleration variance

with increasing St. However, Qureshi et al. (2008) illustrated that this trend is not monotonic and depends on d_η and r_ρ. Their results showed that for $10 < r_\rho < 70$, increasing d_η from 16.5 to 21 increased the streamwise acceleration variance of particles. They argued that increasing d_η further exposed particles to energetic flow motions and increased their acceleration variance. The reviewed literature investigated the interaction of turbulent flow and particles with different St. However, particle motion in particle-laden flows can be also influenced by their interaction with each other.

2.2.1.2 Particle-particle interaction

Previous analytical and numerical studies indicated that particle-particle interaction (PPI) rate for spherical particles in homogeneous isotropic turbulence is proportional to d_p, particle number density, and the velocity of particles relative to each other, V_r, (e.g. Saffman and Turner 1956; Abrahamson 1975; Yuu 1984; Sundaram and Collins 1997; Wang et al. 2000). The dependence of PPI rate on the particle number density and V_r shows the important effect of particle concentration and PTI on the PPI rate. Due to this fact, the level of PPI effect on particle motion in particle-laden turbulent flows has been typically characterized based on particle concentration and St (Elghobashi, 1994). For sub-Kolmogorov particles with large r_ρ, Sundaram and Collins (1997) showed that at low St, the PPI rate sharply increased with increasing St, due to the preferential concentration of particles in high-shear regions and larger V_r. The PPI rate peaked at the St associated with $t_p \approx T_\mathrm{e}$, where T_e is the large-eddy turnover time, and decreased thereafter due to the reduction of V_r (Sundaram and Collins, 1997). Sundaram and Collins (1997) assumed perfectly elastic collision between particles and neglected the effect of the lubrication layer (the fluid layer between two particles that are moving toward each other). Results of their simulations for PPI rate were consistent with those of Saffman and Turner (1956) for $St \to 0$ and Abrahamson (1975) for $St \to \infty$. Sundaram and Collins (1997) also indicated that the PPI rate for sub-Kolmogorov particles with $St = 1$ follows a square dependence relative to d_η that changes to a cubic dependence when $d_\eta \to 0$. These investigations shed light on the

effect of the concentration and St of sub-Kolmogorov particles with large r_ρ on the PPI rate in isotropic turbulence. However, more studies are required to investigate the PPI rate and V_r of particles with $d_\eta > 1$ and $r_\rho \sim \mathcal{O}(1)$ in non-isotropic turbulence.

The effect of PPI on the distribution of particles and their velocity statistics in wall-bounded turbulent flows, which are non-isotropic close to the wall, has been previously investigated in several studies. The increment of PPI reduces the particle number density close to the wall and increases it away from the wall (Varaksin et al., 2000; Kussin and Sommerfeld, 2002; Sommerfeld, 2003). It also increases the particles' average streamwise velocity close to the wall and reduces it away from the wall (Laín et al., 2002; Lin and Chang, 2016; Li et al., 2016). By increasing PPI, the streamwise velocity fluctuation of particles increases away from the wall, but it may increase or decrease near the wall, depending on the particle concentration (Lin and Chang, 2016; Shokri et al., 2017). Previous investigations also showed that increasing PPI increases wall-normal and spanwise velocity fluctuations of particles (Lin and Chang, 2016; Sommerfeld, 2003; Li et al., 2016; Shokri et al., 2017), but reduces their Reynolds shear stress (Shokri et al., 2017). Despite the valuable contribution of these studies in elucidating the effect of PPI on particles kinematics and distribution, more experimental investigations are necessary to investigate particles dynamics and relative velocity in non-isotropic turbulence.

2.2.1.3 Particle-wall interaction

Another factor that affects particle motion in wall-bounded turbulent flows is their inelastic interaction with the wall, which reduces their kinetic energy (Laín et al., 2002) and affects their distribution (Sommerfeld and Huber, 1999; Sommerfeld, 2003). The effect of particle-wall interaction (PWI) on the kinematics of a particle has been typically characterized based on particle collision Stokes number, St_V, which for a spherical particle is defined as

$$St_V = \frac{\rho_p V_i d_p}{9\mu}, \tag{2.19}$$

where V_i is the particle wall-normal impact velocity. Investigations of particles restitution ratio, e_V, the ratio of particle wall-normal velocity after the collision to its V_i, in quiescent

fluids have shown larger e_V for higher St_V (Gondret et al., 2002; Joseph and Hunt, 2004; Stocchino and Guala, 2005; Legendre et al., 2006; Ardekani and Rangel, 2008; Ardekani et al., 2009). Previous studies have also investigated the effects of other factors on PWI including particle shape (Sommerfeld, 2002; Sommerfeld and Lain, 2018), wall roughness (Nguyen and Wells, 2005; Schade and Wozniak, 2010), fluid viscosity (Joseph et al., 2001; Stocchino and Guala, 2005), and impact angle/velocity (Salman et al., 1989; Sommerfeld, 1992). In particle-laden flows, PWI is also affected by PTI and PPI through their influence on impact angle/velocity of particles.

2.3 Non-spherical particle motion in fluid

The motion of a large non-spherical particle in a fluid is more complex and less known than a spherical particle since its interaction with the fluid depends not only on its Re but also on its shape and orientation. In the literature, the shape of non-spherical particles has been characterized based on different factors such as equivalent diameter, aspect ratio, sphericity, roundness, and dynamic shape factor. The equivalent diameter for a particle is defined as the diameter of a sphere with an equal volume of the particle (Jennings and Parslow, 1988). The aspect ratio of a particle is the ratio of its sizes in different dimensions. The sphericity for a particle is calculated as the ratio of the surface area of a sphere with the same volume as the particle to the surface area of the particle (Wadell, 1934). Roundness is defined as ratio of the averaged radius of curvature of convex regions of the particle to its circumscribed circle (Wadell, 1932). The dynamic shape factor for a particle moving in a fluid is determined as the ratio of the drag force experienced by the particle to the drag force that is applied to a volume-equivalent sphere moving in a similar fluid with the same velocity (Fuchs, 1964).

Similar to the equation of motion of spherical particles, the translational motion of a non-spherical particle in a fluid is described based on Newton's second law. However, in addition to the Stokes drag, pressure gradient, added mass, Buoyancy and Basset forces, non-spherical particles also experience a lift force even in Stokes flow. The rotational mo-

tion of a non-spherical particle can be described by Euler's equations. The net torque on a non-spherical particle is determined as the summation of the torques caused by the hydrodynamic forces, due to the non-coincident centers of mass and pressure of the particle, and the resistance torque applied to a rotating particle in a fluid, which acts to reduce the particle angular velocity.

Calculation of the forces and the torques applied to a large non-spherical particle in a fluid has the same challenges explained in Section 2.2 for spherical particles along with more complexities caused by particle shape and orientation. Previous studies have been mostly focused on determining the drag, lift, and moment coefficients of regularly-shaped particles such as ellipsoids, cylinders and cubes with different Reynolds numbers using analytical approaches (Jeffery, 1922; Brenner, 1964), empirical analysis (Ganser, 1993) or numerical simulations (Zastawny et al., 2012; Ouchene et al., 2016; Zarghami and Padding, 2018). In real applications, however, particles are typically non-spherical with irregular shapes and understanding their drag, lift and moment coefficients still needs more investigations and experimental data.

2.3.1 Non-spherical particle motion in particle-laden turbulent flow

Similar to spherical particles, the motion of non-spherical particles in wall-bounded particle-laden turbulent flows depends on their interactions with turbulence, other particles, and the wall. Investigation of these interactions is an area of active research and the effect of particle and flow characteristics on these interactions are not well characterized. Some recent numerical simulations, however, provide great insight on the motion of regularly-shaped non-spherical particles in turbulence. These simulations investigated the effect of particle shape on their rotation and orientation (e.g. Parsa et al. 2012; Marchioli and Soldati 2013; Parsa and Voth 2014; Challabotla et al. 2015), slip velocity (Zhao et al., 2014) and distribution and velocity statistics (van Wachem et al., 2015). Numerical studies provide a valuable contribution in characterizing the effect of particle shape on their kinematics and distribution in turbulent flows. However, to better simulate non-spherical particles

motion in turbulent flows and validate the outcomes of numerical studies, experimental investigations of non-spherical particles dynamics are in need.

Chapter 3

Experimental setup

This chapter describes the experimental setup that is used to perform the experiments of this thesis. The specifications of the flow facility, carrier fluids, flow tracers, and inertial particles used in the experiments are described in the following sections.

3.1 Flow facility

All the experiments were carried out in a horizontal closed flow loop shown in figure 3.1. The flow-loop had a 3 m long transparent channel with a rectangular cross-section with the dimensions of $(Wi \times 2H) = 120 \times 15$ mm^2. Measurements were conducted at $220H$ downstream from the channel entrance to ensure a fully developed turbulent flow inside the test section which had glass walls for optical access. Two gradual transition sections were used at the two ends of the channel to connect it to the 2-inch diameter pipe sections. The flow was circulated inside the loop by a centrifugal pump (LCC-Metal, GIW Industries Inc.). A Coriolis flow meter (Micro Motion F-Series, Emerson Industries) with mass flow accuracy of 0.2% was used to measure the flow rate and the fluid temperature. A double-pipe heat exchanger was used to keep the temperature constant during the experiments. The pressure ports with 1 m distance were located before the channel section to measure the pressure drop in the flow loop. The origin of the coordinate system was at the center of the bottom wall of the test section. The positive direction of the y-axis was toward the top wall.

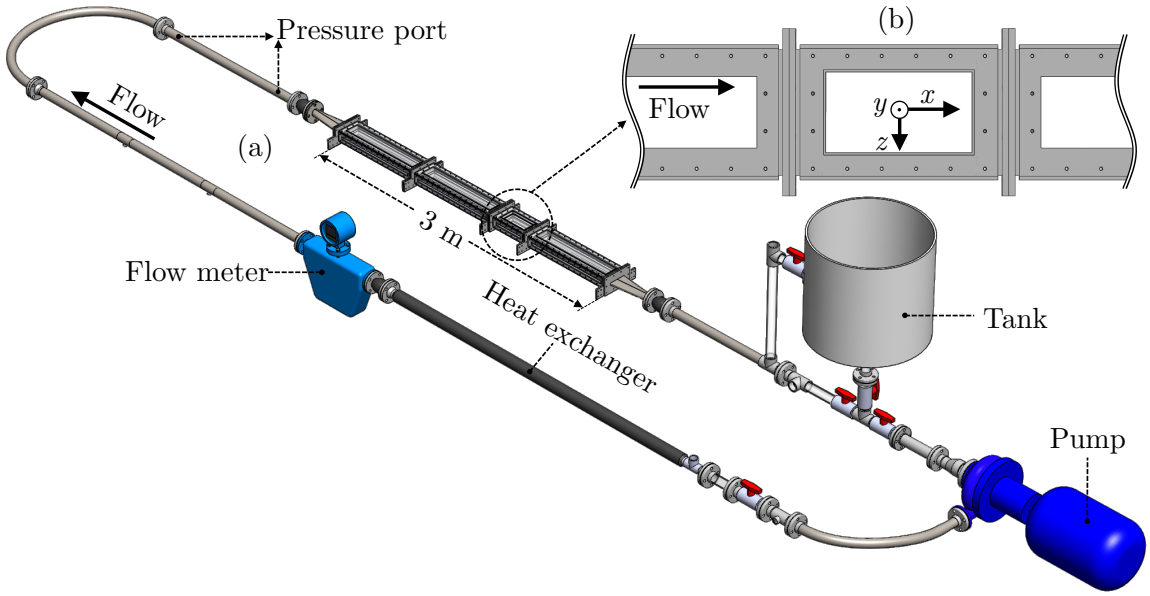

Figure 3.1: (a) Schematic of the horizontal flow loop showing the centrifugal pump, the Coriolis flow meter, the double-pipe heat exchanger, and the rectangular channel. (b) Schematic top view of the test section showing the flow direction and the coordinate system. The origin of the coordinate system was at the center of the bottom wall of the test section. The positive direction of the y-axis was toward the top wall.

3.2 Carrier fluid

The carrier fluid used in the experiments of Chapters 5 to 7 and the Newtonian flow experiments of Chapter 8 was water. For the non-Newtonian flow experiments of Chapter 8, a 90 ppm solution of an anionic polyacrylamide (APAM) polymer with high molecular weight and medium anionic charge density, known as Superfloc (SF) A-125V (Kemira Chemicals Inc.), was used. The polymer powder was weighed using a scale (Mettler Toledo, AB104-S) with 0.1 mg resolution to prepare a 90 ppm SF solution in water. This polymer concentration was chosen to obtain a high drag reduction with small mechanical degradation due to shear, as it will be discussed in Section 8.2. The polymer powder was gradually added to 210 liters of water in a mixing tank while a mixer (Lightnin Labmaster, L5U10F) was operating at 75 rpm. The mixer was equipped with a low-shear three-bladed marine impeller with a diameter of 250 mm. The impeller was located at about half depth of the solution in the tank as it is recommended by Tatterson (1991) and the mixture was mixed for 2 hours

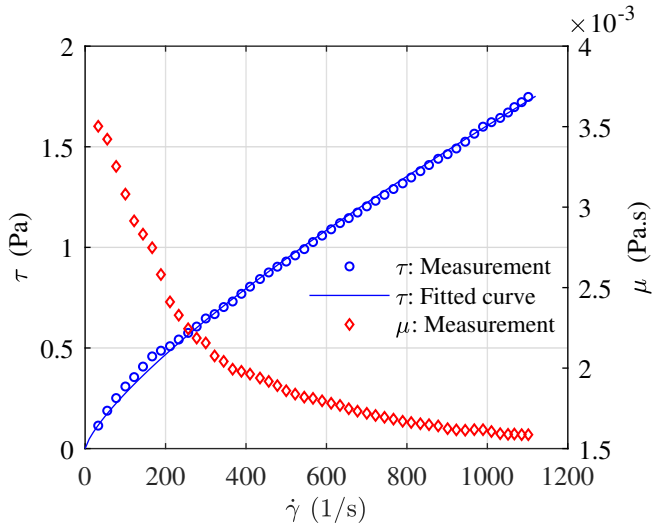

Figure 3.2: The measured τ and μ of the polymer solution at different $\dot{\gamma}$. The solid line shows the fitted curve on τ profile based on the Ostwald-de Waele model.

(Rowin et al., 2018). The difference between the densities of the water and SF solution was negligible.

The dynamic viscosity of the SF solution was measured using the rheometer described in Section 4.4. The shear stress (τ) that the rheometer applied to the polymer solution at different shear rates ($\dot{\gamma}$) is presented on the left vertical axis of Figure 3.2 along with the associated μ shown on the right vertical axis of the plot. The slope of τ versus $\dot{\gamma}$ gradually decreases up to about $\dot{\gamma} = 200$, which indicates a shear-thinning behavior of power-law fluids (Hatschek, 1939). This behavior can be described by Ostwald-de Waele model (Hatschek, 1939), $\tau = K(\dot{\gamma})^n$, where K and n are the flow consistency and behavior indices, respectively. These indices are estimated by fitting the Ostwald-de Waele model to the measured τ, as shown in Figure 3.2. For the 90 ppm SF solution $K = 8.05 \times 10^{-3}$ (Pa.s^n) and $n = 0.766$. In the case of higher $\dot{\gamma}$, the associated τ can be extrapolated using the fitted Ostwald-de Waele model.

3.3 Flow tracers

All the unladen flow measurements in this thesis were implemented by tracking 2 μm silver-coated tracers (SG02S40 Potters Industries), referred to as tracers hereinafter in this thesis, which were added to the flow. These tracers had a density of 3.6 g/cm^3 and a response time of ≈0.65 μs in water at 25°, calculated based on Equation 2.10. The small response time and the high scattering coefficient of these tracers made them appropriate for unladen flow measurements using LPT.

3.4 Spherical inertial particles

Spherical glass particles (Manus Abrasive Systems Inc.) with the density of $\rho_p \approx 2.6$ g/cm^3 were sieved using a sieve shaker and a series of sieves with the mesh size of 500, 420, 297, 250, 149, and 125 μm from top to bottom, respectively. The particles remained in the sieves with the mesh size of 125, 250, and 420 μm (referred to as G-125, G-250 and G-420 hereafter in this thesis, respectively) were used to investigate the near-wall motion of spherical inertial particles. Figure 3.3 indicates the pdf of the diameter of these particles obtained using 2D-LPT system explained in Section 4.2. Table 3.1 presents the specifications of these particles including their mean diameter, d_{50}, the standard deviation of their diameter σ_d and their t_p which was determined based on Equation 2.10 using d_{50} and the density and the dynamic viscosity of water at 25°.

Particle	ρ_p (g/cm^3)	d_{50} (μm)	σ_d (μm)	t_p (ms)
G-125	2.6	135	11	1.8
G-250	2.6	275	19	7.5
G-420	2.6	458	25	21.0

Table 3.1: Properties of glass particles used to study the near-wall motion of spherical inertial particles in turbulent flows. The value of t_p was determined based on Equation 2.10 using d_{50} and the density and the dynamic viscosity of water at 25°.

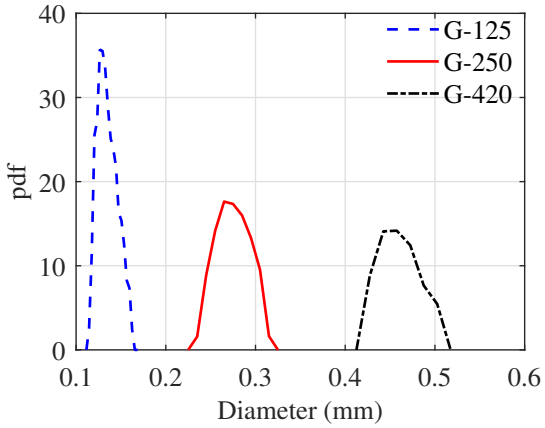

Figure 3.3: The pdf of the diameter of glass particles used to study the near-wall motion of spherical inertial particles in turbulent flows.

3.5 Non-spherical inertial particles

The near-wall motion of non-spherical inertial particles in turbulent channel flows is investigated in Chapter 7 of this thesis using quartz particles (Sil Industrial Minerals) with a density of $\rho_p \approx 2.6$ g/cm^3. The quartz particles were sieved using the same series of sieves described in Section 3.4 and the particles remained in the sieves with the mesh size of 125, 250, and 420 µm (referred to as Q-125, Q-250, and Q-420 hereafter in this thesis, respectively) were used to investigate the near-wall motion of non-spherical inertial particles in Chapter 7. Figure 3.4 illustrates three samples of 2D images of Q-250 particles. Figure 3.5 shows the pdf of the equivalent diameter of quartz particles calculated as the diameter of a circle with the same area as the projected area of the particle (Hinds, 1999). The projected area of the quartz particles was determined using the images recorded for two-dimensional measurements. Table 3.1 presents the specifications of these particles including their d_{50}, σ_d, and t_p which was determined based on Equation 2.10 using d_{50} and the density and the dynamic viscosity of water at 25°. The sphericity of the quartz particles was determined as the perimeter of a circle with the same area as the projected area of the particle to the perimeter of the particle (Zheng and Hryciw, 2015). Figure 3.6 shows the pdf of the sphericity for Q-125, Q-250, and Q-420. The average and the standard deviation of the sphericity of the quartz particles were approximately 0.85 and 0.05, respectively. The aspect ratio of

quartz particles was determined as the ratio of the length of their minor axis to the length of their major axis. Figure 3.7 shows the pdf of the aspect ratio for Q-125, Q-250, and Q-420. Figure 3.8 shows the pdf of the roundness for quartz particles determined as the ratio of the averaged radius of curvature of convex regions of a quartz particle to its circumscribed circle.

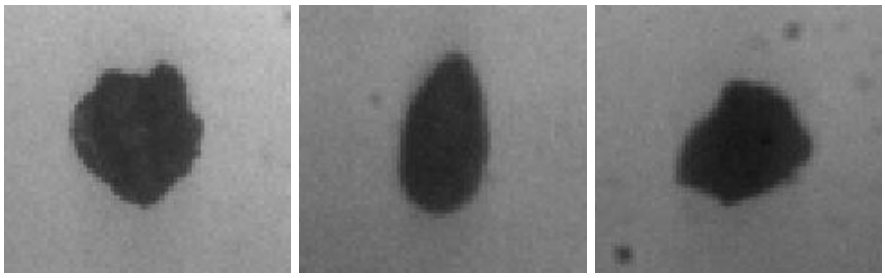

Figure 3.4: Sample of the 2D images of the Q-250 particles.

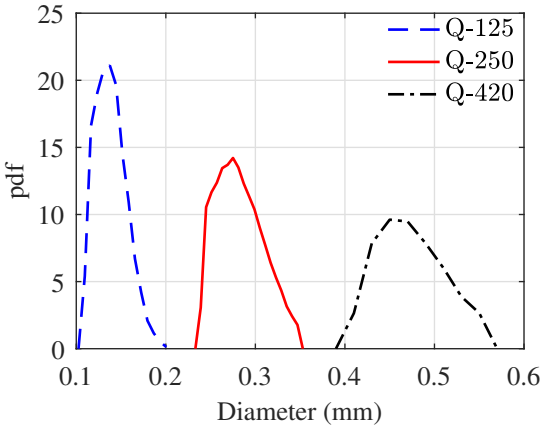

Figure 3.5: The pdf of the diameter of quartz particles used to study the near-wall motion of non-spherical inertial particles in turbulent flows.

Particle	ρ_p (g/cm^3)	d_{50} (µm)	σ_d (µm)	t_p (ms)
Q-125	2.6	138	17	1.9
Q-250	2.6	283	26	8.0
Q-420	2.6	473	37	22.3

Table 3.2: Properties of quartz particles used to study the near-wall motion of non-spherical inertial particles in turbulent flows. The value of t_p was determined based on Equation 2.10 using d_{50} and the density and the dynamic viscosity of water at 25°.

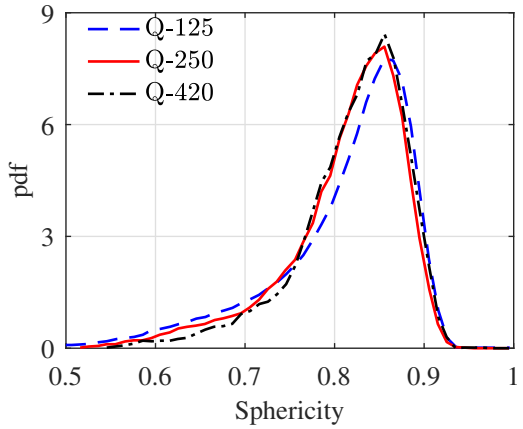

Figure 3.6: The pdf of the sphericity of quartz particles.

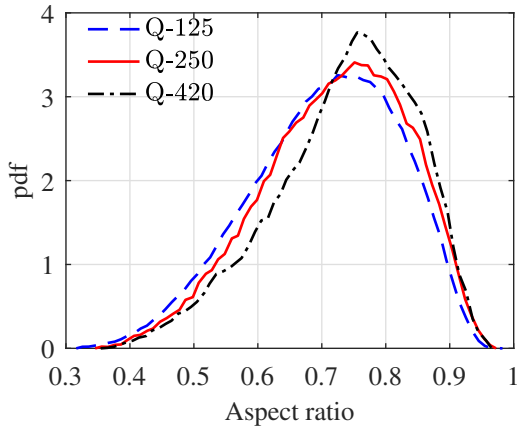

Figure 3.7: The pdf of the aspect ratio of quartz particles.

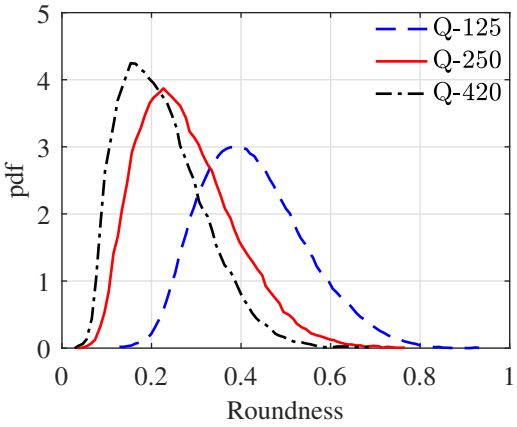

Figure 3.8: The pdf of the roundness of quartz particles.

Chapter 4

Measurement systems

This chapter describes the measurement systems used to fulfill the objectives of the thesis discussed in Section 1.2. The trajectory of tracers and particles were detected using LPT to study the instantaneous dynamics of the flow and particles. The required data to perform the analyses were provided using planar and three-dimensional LPT systems. The LPT measurement systems described in this chapter are organized based on their complexities. The first section of this chapter introduces the 2D-LPT system used for the experiments of Chapter 8. Section 4.2 describes the 2D-LPT system with backlight illumination used to perform the particle-laden measurements of Chapter 7. The specifications of the 3D-LPT system that was set up to conduct the experiments of Chapters 5 and 6 are provided in Section 4.3. The rheometer which was used to measure the viscosity of the polymer solution used for the experiments of Chapter 8 is introduced in Section 4.4. Finally, in the last section of this chapter, the pressure measurement system utilized to determine the pressure drop in drag-reduced turbulent polymeric flows for the experiments of Chapter 8 is explained.

4.1 Two-dimensional Lagrangian particle tracking

A 2D-LPT system was used to detect the Lagrangian trajectories of tracers and particles in the experiments of Chapter 8. In those experiments, the effect of a drag-reduced turbulent polymeric flow on the near-wall kinematics of particles and their dispersion was investigated.

4.1.1 Apparatus

Figure 4.1 illustrates a schematic of the 2D-LPT system with conventional illumination. The system included a dual-cavity Nd:YLF laser (DM20-527, Photonics Industries) with a wavelength of 527 nm. Each cavity of the laser had maximum energy of 20 mJ per pulse (at 1 kHz). A combination of cylindrical and spherical lenses was used to form a laser sheet with approximately 1 mm thickness. The laser sheet was directed from the bottom window and covered a streamwise-wall-normal plane ($x-y$) in the mid-span of the channel. The images were recorded by a CMOS high-speed camera (Phantom v611) with a pixel size of 20×20 μm^2 operated at a cropped sensor size of 896×348 pix. A Sigma SLR objective lens with a focal length of $f = 105$ mm at aperture size of $f/8$ was used to image at a magnification of 1.42, resulting in the field-of-view of 12.5×4.8 mm^2 with the digital resolution of 0.014 mm/pix and the depth-of-field of 0.5 mm. A programmable timing unit (HSC v2, LaVision GmbH) controlled by DaVis 8.4 (LaVision GmbH) was used to synchronize the laser with the camera.

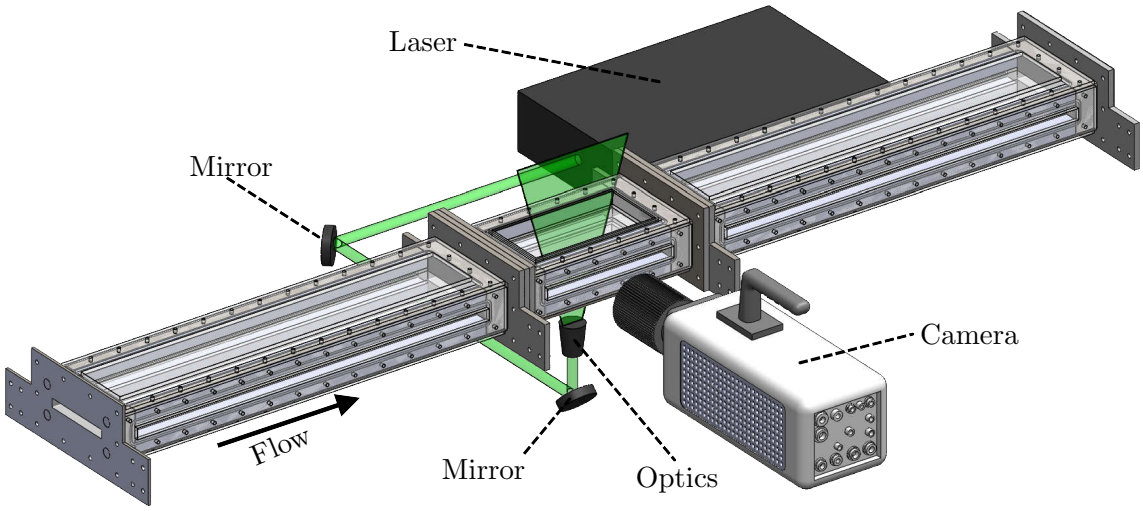

Figure 4.1: Schematic of the 2D-LPT system with conventional illumination used for the measurements of Chapter 8, showing the arrangement of the laser, optics, and the camera.

Time-resolved images were recorded at an acquisition rate of 17.6 kHz with each laser cavity operating at 8.8 kHz. The unladen flow measurements were implemented by tracking

the tracers, described in Section 3.3, which were added to the flow. The tracers had an image size of 3 pix and their number density in the frames was about 0.03 tracer per pixel, equivalent to 153 tracers/mm^2. The maximum displacement of the tracers in unladen flow measurement was about 10 pix between two consecutive frames. The particle-laden experiments of Chapter 8 were performed using G-250 particles, described in Section 3.4. These particles had an image diameter of about 18 pix, with a maximum displacement similar to that of the tracers. The specifications of the 2D-LPT setup are detailed in Table 4.1.

Field-of-view	12.5×4.8 mm^2
Magnification	1.43
Digital resolution	0.014 mm/pix
Depth of field	0.5 mm
Image size of tracers	3 pix
Image size of particles	18 pix
Image acquisition frequency	17.6 kHz

Table 4.1: The specifications of the 2D-LPT system used to perform the measurements of Chapter 8.

4.1.2 Image processing

To remove the background intensity caused by the reflection of the laser sheet and improve the signal-to-noise ratio of the images, the minimum intensity of the ensemble of images was subtracted from each image. The resulting images were multiplied by a constant to reach the maximum digital threshold and then they were normalized by the average intensity of the ensemble. The signal-to-noise ratio was also improved by subtracting the sliding minimum intensity within a kernel size of 3 pixels followed by normalization using local average intensity within a kernel of 10 pixels. A Gaussian filter with a kernel size of 3×3 pixel was also applied (Kähler et al., 2012). The trajectory of tracers in unladen and particle-laden experiments was processed by Davis 8.4 (LaVision GmbH). In processing the images of the particle-laden experiments, particles were separated from the tracers based on their size. The maximum change in tracers displacement was limited to 5 pixels and

the maximum relative velocity change to 50% between two temporally consecutive velocity vectors.

The trajectories of particles for the two-phase flow measurements were processed using a particle tracking algorithm developed in MATLAB (MathWorks Inc.). In the first step, the location of the particles in all the recorded frames was detected using circle Hough transforms (Yuen et al., 1990; Atherton and Kerbyson, 1999) and an interrogation window was defined around each particle. Based on the mean velocity profile, the algorithm predicted the location of each particle in the next image frame. Another interrogation window was defined around the predicted location and the precise location of the particle was determined from the correlation peak between the two interrogation windows. This process was continued by detecting and tracking particles in the subsequent frames to form time-resolved tracks (Ohmi and Li, 2000).

To reduce the noise of the trajectories and determine the streamwise and wall-normal instantaneous velocities (U and V) of the tracers and particles, a quadratic regression fit was applied on their trajectories. A quadratic regression over a long period, i.e. large temporal kernel (t_k), can filter out the high-frequency content of the data while a short t_k may not be effective in reducing the noise. Therefore, an optimal t_k needs to be used for the quadratic fit. The optimal t_k can be estimated by evaluating the rms of acceleration following the method used by Voth et al. (2002) and Gerashchenko et al. (2008). Voth et al. (2002) showed that the acceleration rms can be estimated as a summation of an exponential term (represents the contribution of turbulence) and a power-law term (represents the contribution of position noise). They argued that an estimation of the acceleration rms can be obtained by extrapolation of the exponential term to $t_k = 0$. The variation of the rms of the streamwise acceleration (a_x) with t_k at $y/H = 0.017$ (the first data point after the wall for particle-laden flows studied in Chapter 8) for the unladen water flow experiment in Chapter 8 is presented in Figure 4.2. The a_x is normalized by ν and the u_τ of the water flow. It is observed that the normalized a_x deviates from the fitted exponential function at $t_k \approx 1.7$ ms. This deviation indicates that the noise in the estimation of a_x rapidly

increases for shorter temporal kernels. Therefore, the t_k of 1.7 ms was selected as the optimum temporal kernel size following the method used by Gerashchenko et al. (2008). For consistency of the estimations, trajectories shorter than 1.7 ms were discarded.

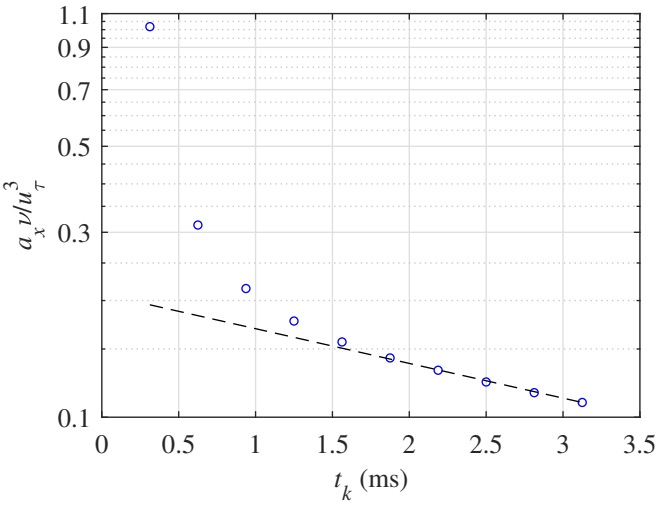

Figure 4.2: The variation of normalized a_x of the unladen water flow at $y/H = 0.017$ as a function of t_k (symbols). The dashed straight line shows the fitted exponential function based on the method presented by Voth et al. (2002).

More than 1.7×10^6 trajectories longer than 1.7 ms were detected in 40,000 images recorded for unladen water and polymeric flows. From 57,000 images recorded for particle-laden water flow experiments, more than 46,000 particle trajectories were detected while 18,000 of them were longer than 1.7 ms. For the particle-laden polymeric flow, 57,000 images were recorded, about 14,000 trajectories were detected and more than 2,000 of them were longer than 1.7 ms. As will be discussed in Section 8.3.2.1, the smaller number of particle trajectories in the near-wall region of polymeric particle-laden flow is due to the more uniform distribution of particles in the wall-normal direction, reducing their near-wall concentration. Samples of the particle trajectories in water and polymeric flows detected by the developed algorithm are presented in Figure 4.3.

4.1.3 Uncertainty evaluation

The random error of velocity statistics of unladen and particle-laden flows studied in Chapter 8 was determined based on the statistical convergence of the last 20% of data collected

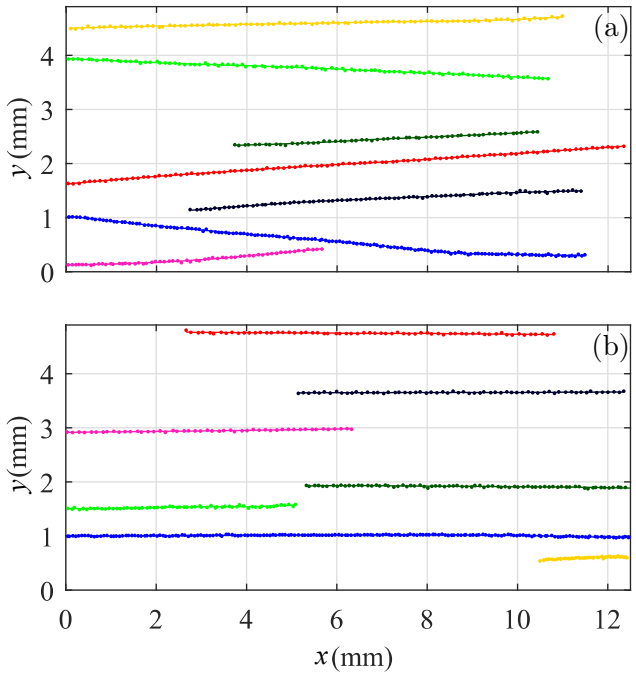

Figure 4.3: Samples of particle trajectories in (a) water and (b) polymeric flows. These trajectories were detected using the 2D-LPT algorithm. Symbols show the detected particle positions and the lines show the quadratic fit with the temporal kernel of 1.7 ms.

at $y/H = 0.017$ and are presented in Table 4.2.

Random error	$\langle U \rangle$ $\times 10^3$ m/s	$\langle V \rangle$ $\times 10^4$ m/s	$\langle u^2 \rangle$ $\times 10^3$ $(\mathrm{m/s})^2$	$\langle v^2 \rangle$ $\times 10^5$ $(\mathrm{m/s})^2$	$\langle uv \rangle$ $\times 10^5$ $(\mathrm{m/s})^2$
Unladen water flow	0.86	0.52	0.10	1.20	0.48
Unladen polymeric flow	0.55	0.05	0.03	0.23	0.15
particles in water flow	4.10	4.00	0.70	5.20	8.00
particles in polymeric flow	5.20	2.60	3.80	4.10	7.50

Table 4.2: The random error of the average velocity and Reynolds stresses of unladen and particle-laden flows of Chapter 8 based on the statistical convergence of the last 20% of data collected at $y/H = 0.017$.

4.2 Two-dimensional Lagrangian particle tracking with backlight illumination

A 2D-LPT system with backlight illumination was used to detect the Lagrangian trajectories of particles for the experiments of Chapter 7. In those experiments, the effect of particle shape and size on the near-wall dynamics of particles and their interaction with the wall was investigated. The particle-laden experiments of Chapter 7 were performed using glass and quartz particles described in Sections 3.4 and 3.5, respectively. The backlight illumination was used to provide a better contrast between the particles and the surrounding fluid compared to the traditional illumination, resulting in higher accuracy in detecting interface between particles and the fluid in the images. The unladen flow measurements of Chapter 7 were performed using the same 2D-LPT system but with a conventional illumination (see Figure 4.1) to images the 2 μm silver-coated tracers using their high scattering coefficient and avoid peak locking (Kähler et al., 2012).

4.2.1 Apparatus

Figure 4.4 illustrates a schematic of the 2D-LPT system with backlight illumination used for particle-laden experiments. The system included the same laser, camera, and programmable timing unit (controlled by DaVis 8.4, LaVision GmbH) used in the 2D-LPT system discussed in Section 4.1.1. The backlight illumination was provided by diffusing the laser beam using a 150 ppm solution of Rhodamine B (R6626, Sigma-Aldrich) in water, filled the chamber of a diffuser with the depth of 2 cm, following the method used by Jain et al. (2016). The images were recorded by a Phantom v611 camera operated at a cropped sensor size of 1280×312 pix. A Sigma SLR objective lens with a focal length of $f = 105$ mm at aperture size of $f/8$ was used with an extension to image the streamwise-wall-normal plane ($x - y$) in the mid-span of the channel at a magnification of 1.78, providing a field-of-view of 14.3×3.5 mm^2, the digital resolution of 0.011 mm/pix, and the depth-of-field of 0.4 mm. The unladen flow measurements were performed using the same 2D-LPT system (with the same magnification, field-of-view, digital resolution, and depth-of-field) but with a conventional illumination.

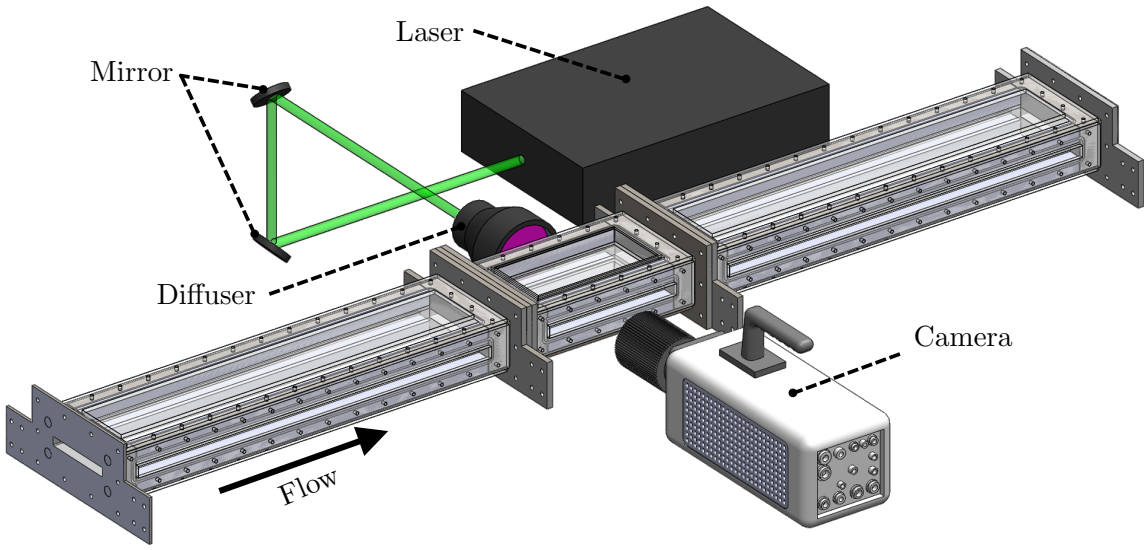

Figure 4.4: Schematic of the 2D-LPT system with backlight illumination used for the particle-laden flow measurements of Chapter 7, showing the arrangement of the laser, camera, and the diffuser.

Images were recorded at an acquisition rate of 8 kHz with each laser cavity operating at 4 kHz. The particle-laden experiments were performed using the spherical glass particles (G-125, G-250, and G-420) and the non-spherical quartz particles (Q-125, Q-250, and Q-420). The G-125, G-250, and G-420 particles had an image diameter of approximately 12, 24, and 40 pix, respectively. Experiments were performed at Re_τ of 770 and the maximum displacement of particles between two consecutive frames was approximately 20 pixels. The image size of tracers in the unladen flow measurements was about 4 pix and their number density in the images was about 0.03 tracer per pixel. The maximum displacement of tracers between two consecutive frames was similar to that of the particles.

4.2.2 Image processing

The image processing procedure for the unladen flow was similar to the procedure explained in Section 4.1.2 and conducted in Davis 8.4 (LaVision GmbH). The trajectories of tracers in unladen flow were also detected using Davis 8.4 (LaVision GmbH). The maximum change in tracers displacement was limited to 5 pixels and the maximum relative velocity change was limited to 50% between two temporally consecutive velocity vectors.

For the particle-laden flow images, first, their intensity was inverted and then the minimum intensity of the ensemble of images was subtracted from them to remove the background intensity and improve the signal-to-noise ratio. The resulting images were multiplied by a constant to reach the maximum digital threshold and then they were normalized by the average intensity of the ensemble, followed by subtracting the sliding minimum intensity within a kernel size of 3 pixels. Particle trajectories in the two-phase flow measurements were detected using the particle tracking algorithm developed in MATLAB (MathWorks Inc.), described in Section 4.1.2. However, instead of using circle Hough transforms for particle detection in this algorithm, particles were detected based on their contrast with the surrounding fluid.

Similar to Section 4.1.2, to reduce the noise in tracer and particle position and obtain their Lagrangian streamwise and wall-normal velocities, a quadratic regression fit was applied on their trajectories. The variation of acceleration rms (a) with t_k at $y/H = 0.017$ (the closest data point to the wall for the particle-laden measurements of Chapter 7) for the unladen water flow is presented in Figure 4.5. The optimal t_k was selected based on the same method explained in Section 4.1.2 and it was equal to 1 ms. For consistency of the estimations, all the tracer/particle trajectories shorter than 1 ms were discarded.

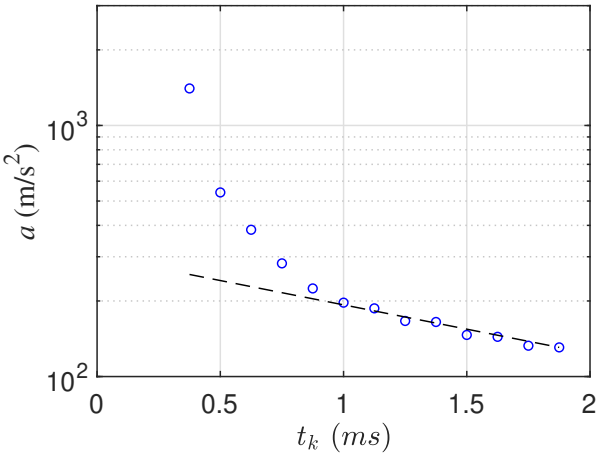

Figure 4.5: The variation of a of the unladen water flow at $y/H = 0.017$ as a function of t_k (symbols). The dashed straight line shows the fitted exponential function based on the method presented by Voth et al. (2002).

4.2.3 Uncertainty evaluation

The random error of the velocity and acceleration statistics of particle-laden flows studied in Chapter 7 were determined based on the statistical convergence of the last 20% of data collected at $y/H = 0.017$ and $y/H = 0.028$ (the closest data points to the wall for the analysis of the effect of particle shape and size on their motion, respectively) and presented in Tables 4.3 and 4.4, respectively.

Particle type	$\langle U \rangle$	$\langle u^2 \rangle$	$\langle v^2 \rangle$	$\langle uv \rangle$	$\langle A_x \rangle$	$\langle A_y \rangle$
G-250	0.18	0.40	0.90	0.57	0.78	0.58
Q-250	0.08	0.83	0.26	0.49	0.84	0.55

Table 4.3: The random error percentage of the average values of velocity and acceleration statistics for the measurements of Chapter 7, based on the standard deviation of the last 20% of data collected at $y/H = 0.017$ for G-250 and Q-250 particles.

Particle type	$\langle U \rangle$	$\langle u^2 \rangle$	$\langle v^2 \rangle$	$\langle uv \rangle$
G-125	0.11	0.50	0.26	0.81
G-250	0.15	0.43	0.51	0.66
G-420	0.11	0.85	2.52	3.57
Q-125	0.06	0.19	0.41	0.28
Q-250	0.11	0.48	0.28	0.46
Q-420	0.12	1.18	0.94	3.60

Table 4.4: The random error percentage of the average values of velocity statistics of Chapter 7, based on the standard deviation of the last 20% of data collected at $y/H = 0.028$.

4.3 Three-dimensional Lagrangian particle tracking

The Lagrangian 3D trajectories of tracers and particles required for the analysis of Chapters 5 and 6 were detected using the data provided by a 3D-LPT system. The analyses presented in Chapter 5 were performed to investigate the near-wall motion of spherical particles in turbulent channel flows. In Chapter 6, the effect of Re_τ and C_v on particle motion was investigated by performing the experiments at $Re_\tau = 410$ and 765 and volume concentrations

of $C_v = 0.03\%$ and 0.15%.

4.3.1 Apparatus

Figure 4.6 shows the schematic of the 3D-LPT system. The system consisted of four Phantom v611 cameras which were equipped with sigma SLR objective lenses with a focal length of $f = 105$ mm. The lenses were set to an aperture size of $f/16$ and connected to the cameras using Scheimpflug adapters. The cameras were positioned in a plus-like configuration as seen in the figure. The line-of-sight of each camera had a solid-angle of approximately 35° from the y-axis. The programmable timing unit (HSC v2, LaVision GmbH) commanded by DaVis 8.4 (LaVision GmbH) was used to synchronize the cameras with the Nd:YLF laser (DM20-527, Photonics Industries International Inc.). A collimator along with spherical and cylindrical lenses was used to change the laser beam to a laser sheet with cross-section of 50×4 mm^2 in the x and y directions. This laser sheet was directed in the spanwise direction through the glass side wall and flush to the bottom wall. A knife-edge was located outside the side wall to crop the laser sheet at $y = 4$mm and limit it to $0 \leq y \leq 4$ mm. A mirror was used after the test section, on the opposite side, to reflect the laser sheet back into the test section and increase the light intensity (Ghaemi and Scarano, 2010).

A dual-plane calibration plate was used to project the physical coordinate system on the image coordinate system using a third-order polynomial function. The mapping function was further improved using a volume self-calibration procedure at low seeding density to reduce the calibration errors (Wieneke, 2008). This process was carried out in DaVis 8.4 (LaVision GmbH). The mapping function showed that the 3D-LPT system had a magnification of 0.41 and a digital resolution of 0.049 mm/pixel. This magnification and the aperture size resulted in a depth-of-focus of 7.9 mm. The measurement volume was $50\times4\times30$ mm^3, equivalent to $1024\times82\times608$ pix^3.

Image acquisition was carried out in single-frame mode using a cropped sensor size of 1024×608 pixel, and with simultaneous operation of both laser cavities in each frame. For unladen experiments, cameras were operated at an acquisition rate of 6 kHz for 3 seconds

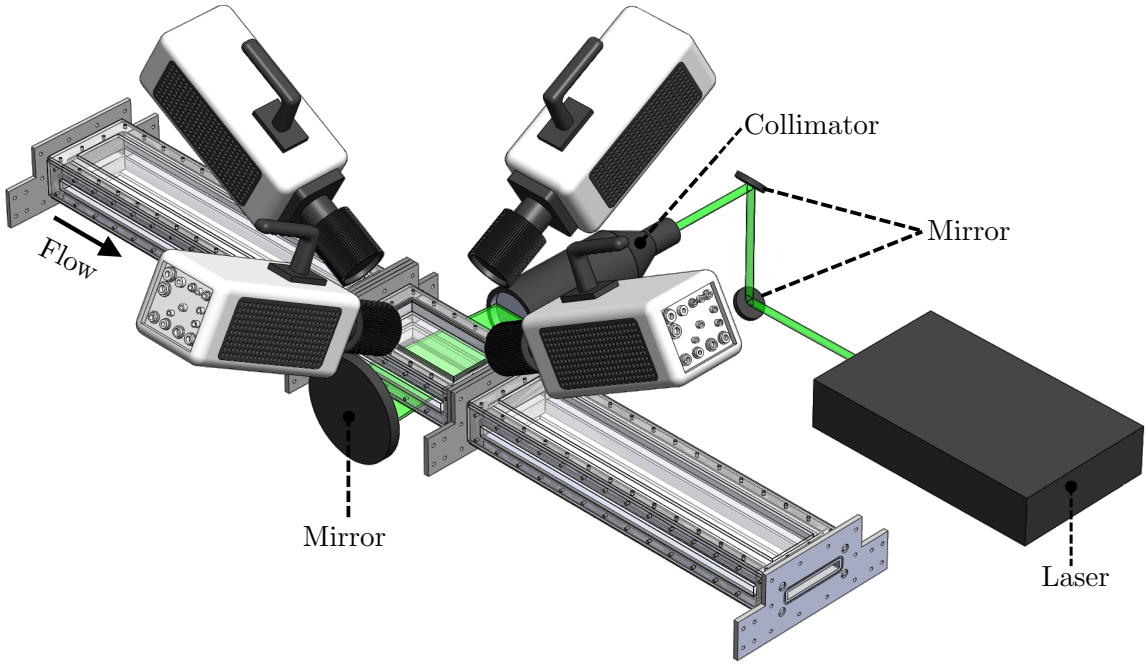

Figure 4.6: Schematic of the 3D-LPT system used for the measurements of Chapters 5 and 6, showing four high-speed cameras in a plus-like configuration and the illumination path. The collimator directs the laser sheet into the test section from the side wall. A mirror was used on the other side of the test section to reflect the output laser sheet back into the test section and equalize the cameras' image intensity in backward and forward scattering orientations (Ghaemi and Scarano, 2010).

(three discrete sets of one-second image recording) at each Re_τ. The unladen experiments were performed using the silver-coated tracers at the same mass flow rate of particle-laden experiments to verify the accuracy of the measurement system and the processing algorithm by comparing the measured velocity and acceleration statistics with direct numerical simulation (DNS) of unladen flows. The acquisition rate of the imaging system was set on 10 kHz for particle-laden experiments to better resolve particles motion in the vicinity of the wall and investigate particle-wall collisions. The particle-laden measurements were carried out for 5 seconds (five discrete sets of one-second image recording) at each Re_τ, without any tracers. The image of tracers and the particles both had a Gaussian intensity distribution with an image diameter of approximately 3 pixels. Tracers had an average image number density of 0.024 tracer per pixel. The maximum displacement of tracers for

the low and high Re_τ cases of unladen experiments was about 4 and 8 pixels, respectively. The number density of particles in the images at C_v of 0.03% and 0.15% was about 0.008 and 0.04 particles per pixel, respectively. The maximum particle displacement at Re_τ of 410 and 765 was not more than 3 and 6 pixels, respectively.

4.3.2 Image processing

The signal-to-noise ratio of the images was improved by subtracting the local minimum intensity of the ensemble of images from each image, followed by subtraction of the minimum intensity within a kernel of five pixels. The intensity of each pixel was also divided by the average intensity within a kernel of 50 pixels. The intensity of all images was also normalized relative to each other and a Gaussian filter with a kernel of 3×3 pixel was applied to avoid peak locking (Kähler et al., 2012).

The 3D Lagrangian trajectories of tracers in unladen experiments and particles in laden experiments were detected using shake-the-box (STB) algorithm (Schanz et al., 2016) carried out in DaVis 8.4 (LaVision, GmbH). This state-of-the-art LPT algorithm provides an accurate estimation of particles (or tracers) location using the temporal and spatial information of their trajectories. In this algorithm, the location of each particle was first determined based on its intensity with an allowed triangulation error of 0.5 pixel (25 μm). After detecting the trajectory of the particle for a certain number of time steps by image matching, a Wiener filter (Wiener, 1949) was applied on the detected trajectory to extrapolate it and predict the particle location in the next time step. The predicted location was corrected by shaking the particle image within a kernel of 0.1 pixel in the three dimensions (Wieneke, 2013). This procedure was performed for all the particles detected in the images and provided their Lagrangian 3D trajectories. The accurate detection of trajectories was also ensured by setting the maximum allowable displacement between two consecutive images to 6 and 9 pixels for tracers in unladen experiments and 4 and 7 pixels for particles in laden experiments for the low and high Re_τ cases, respectively. The maximum absolute change in the displacement of each tracer/particle between two consecutive images was set

to 2 pixels with the maximum relative change of 10%.

The location of the lower wall was obtained using the minimum intensity of all the images. This minimum image was mostly dark, except for a few glare points due to the reflection of the laser from the wall. To find the 3D position of the glare point, i.e. wall location, the minimum image was reconstructed into the 3D domain using the multiplicative algebraic reconstruction technique, known as MART, in DaVis 8.4 (Elsinga et al., 2006). The average intensity of the glaring points was determined in each reconstructed x–z plane. A Gaussian distribution was fitted on the wall-normal variation of glare points' intensity, as seen in Figure 4.7 , to obtain the wall location with subpixel accuracy. Based on this procedure the uncertainty of the wall location is 0.1 pixel which is equivalent to 4.9 µm.

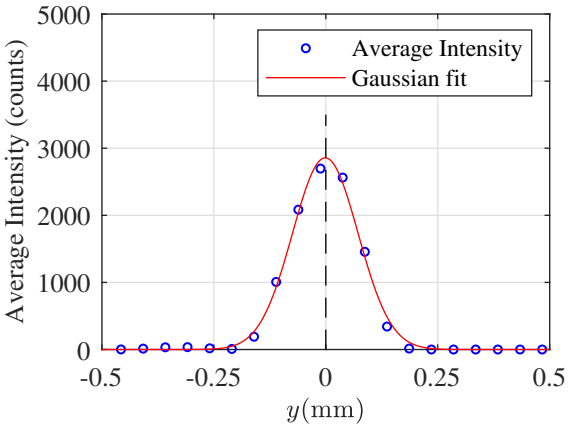

Figure 4.7: Average intensity of glaring points on the wall at different wall-normal locations.

The Lagrangian streamwise, wall-normal, and spanwise velocities (U, V, W) and accelerations (A_x, A_y, A_z) of each tracer/particle were determined by fitting a quadratic regression function on its trajectory. The optimal t_k for each measurement was selected based on the same method explained in Section 4.1.2. The variation of the acceleration rms with temporal kernel size at $y/H = 0.008$ (the first data point after the wall for particle-laden flows studied in Chapters 5 and 6) for the unladen and particle-laden experiments performed in Chapters 5 and 6 are presented in Figure 4.8. The first letter of the acronyms in the legends refers to low Re_τ (L) or high Re_τ (H) and the second letter refers to unladen (U), low C_v (L), or high C_v (H). The optimal temporal kernel was selected as the minimum

kernel size just before the increase in noise of acceleration rms following the method used by Gerashchenko et al. (2008) and it was 4.5 and 2 ms for the experiments at low and high Re_τ, respectively.

Six samples of particle's 3D trajectories detected by the STB algorithm at $Re_\tau = 765$ and $C_v = 0.03\%$ are presented in Figure 4.9(a). The variation of the wall-normal component of position, velocity, and acceleration vectors (y, V, and A_y, respectively) in time, t, for one of these trajectories are indicated in Figures 4.9(b-d), respectively. This trajectory shows large wall-normal displacement in the measurement domain and its wall-normal direction of motion changes at $t \approx 2$, 13, 26 ms. As expected, the V of the particle is consistent with the slop of the profile in Figure 4.9(b). The A_y of this trajectory shows its large magnitudes and fluctuation of wall-normal acceleration within the range of -300 to 300 m/s^2.

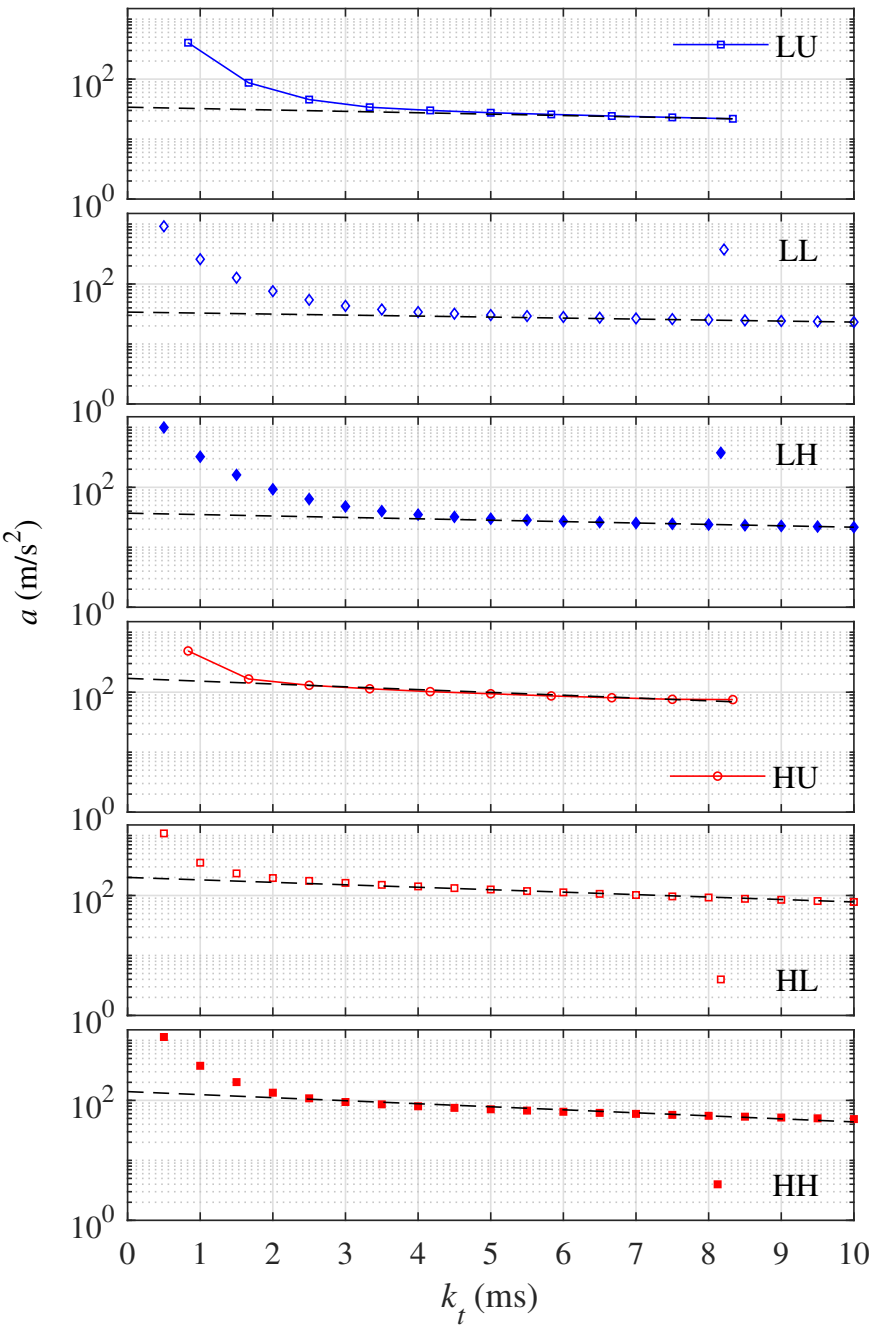

Figure 4.8: The variation of a at $y/H = 0.008$ with k_t. The straight dashed lines are fitted on the exponential part of the curves.

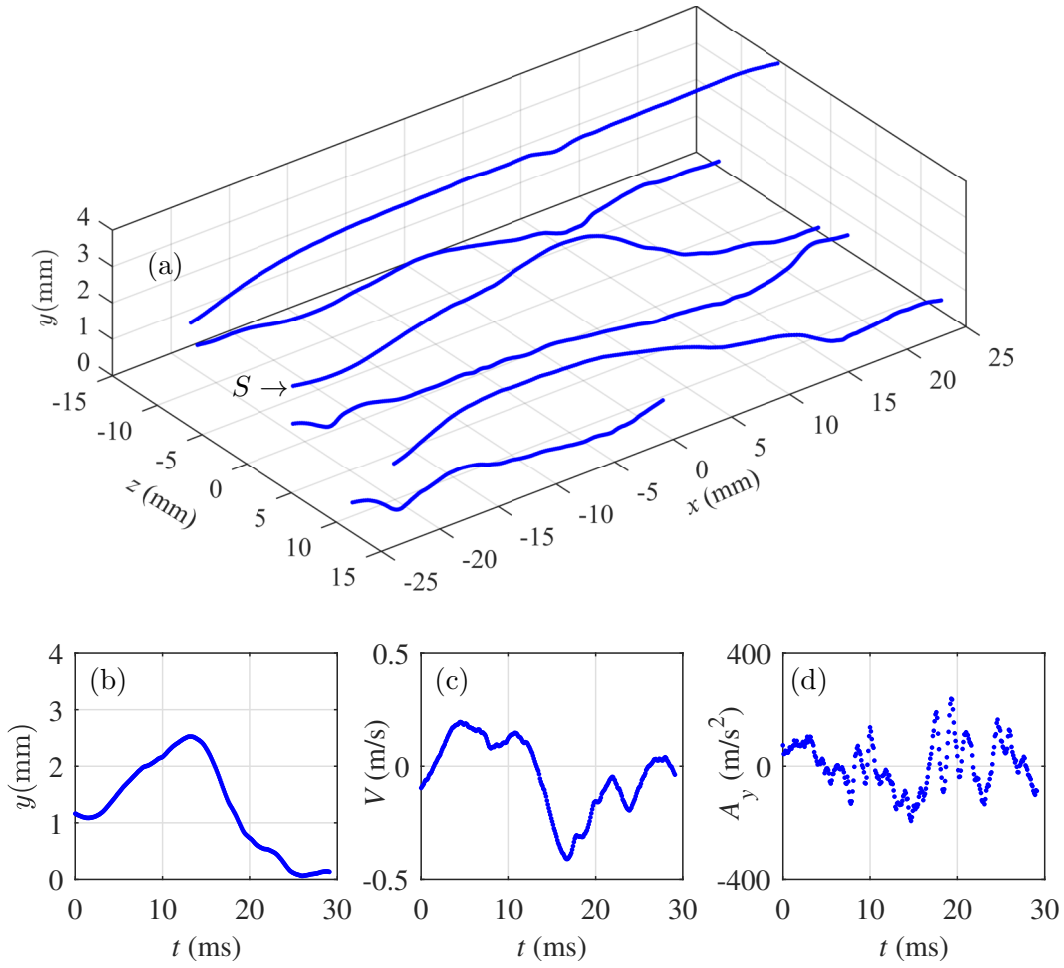

Figure 4.9: (a) Samples of particle trajectories at $Re_\tau = 765$ and $C_v = 0.03\%$ detected by the STB algorithm. The trajectories are colored according to the magnitude of their instantaneous total acceleration. The variation of (b) y, (c) V, and (d) A_y in time for the trajectory S in figure 4.9(a) shows its large acceleration fluctuation in all directions. Colors in (b-d) show the instantaneous wall-normal location of the particle.

4.3.3 Uncertainty evaluation

The level of the measurement noise of the 3D-LPT system in detecting the particles position and the performance of the regression function in reducing this noise are investigated in this section by evaluating the pre-multiplied linear spectral density (LSD) of particles position before and after applying the regression function, following the method of Gesemann et al. (2016). The pre-multiplied LSD of the components of the position vector is presented in figure 4.10 as a function of the frequency, normalized by the Nyquist frequency, $\bar{f}$. The flat

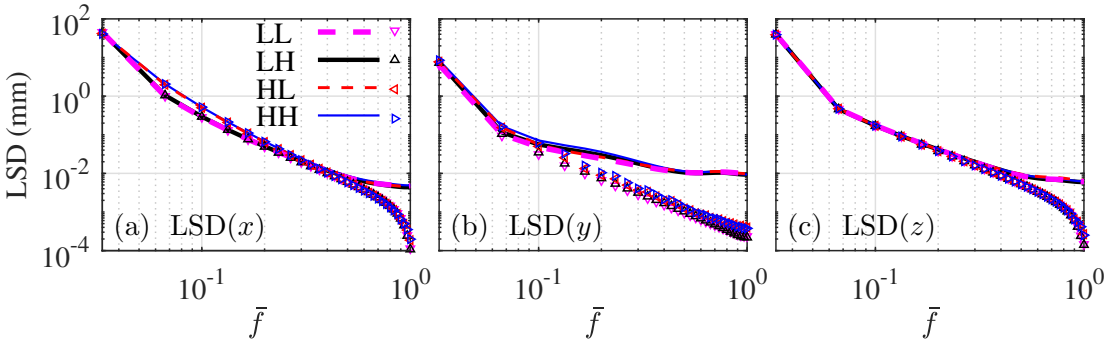

Figure 4.10: The pre-multiplied LSD of (a) x, (b) y, and (c) z components of particles' position before (lines) and after (symbols) applying the quadratic regression function.

part of the LSD profiles with high frequencies before applying the regression function shows the measurement noise level in estimating the particle location in the associated direction (Gesemann et al., 2016). Based on the LSD of the flat parts at $\bar{f} = 1$, the measurement noise level in x and z is approximately 5 and 6 µm, respectively, which is equivalent to 0.1 pixel. The level of the noise in the wall-normal direction is larger than the other directions and it is approximately 10 µm, equivalent to 0.2 pixel. The high-frequency spatial noise level is reduced to less than 0.5 µm in all directions, after applying the quadratic regression function on the trajectories.

The random error percentage of the average values of velocity and acceleration statistics at $y/H = 0.008$ are presented in table 4.5. The approximate number of the data points at this location, N_d, for calculating the average values is also reported for each experiment. The a_y and a_z in this table represents the rms of wall-normal and spanwise component of acceleration vector, respectively, and $\langle V_r \rangle$ is the mean relative velocity of particles with respect to each other.

4.4 Viscosity measurement

A rheometer (RheolabQC, Anton Paar USA, Inc.) equipped with a double-gap cylinder was used to measure μ of the polymer solution for the experiments of Chapter 8. Due to the

Acronym	N_d, $\times 10^{-6}$	$\langle U \rangle$	$\langle u^2 \rangle$	$\langle v^2 \rangle$	$\langle w^2 \rangle$	$\langle uv \rangle$	$\langle A_x \rangle$	$\langle A_y \rangle$	a_x	a_y	a_z	$\langle V_r \rangle$
LU	0.9	0.04	0.19	0.23	0.19	0.18	0.34	0.97	0.15	0.15	0.11	-
LL	6	0.11	0.38	0.32	0.30	0.43	0.57	0.77	0.20	0.29	0.57	0.99
LH	4	0.04	0.29	0.36	0.32	0.63	1.01	1.80	0.13	0.31	0.30	0.21
HU	0.5	0.31	0.53	0.52	0.70	0.46	0.82	0.98	0.15	0.33	0.35	-
HL	6	0.10	0.20	0.08	0.41	0.30	0.31	0.24	0.06	0.03	0.05	1.49
HH	4	0.05	0.10	0.09	0.42	0.30	0.28	0.09	0.09	0.07	0.17	1.99

Table 4.5: The random error percentages of the average values of velocity and acceleration statistics of Chapters 5 and 6, based on the standard deviation of the last 20% of data collected at $y/H = 0.008$ in each experiment.

small gap between the cylinders, the double-gap cylinder system can measure viscosity at a high shear rate, $\dot{\gamma}$, in a laminar flow by avoiding transition to turbulence, which reduces the measurement accuracy (Taylor, 1923).

4.5 Pressure measurement

The pressure measurement was utilized to determine the drag reduction, DR, of the polymer solution used for the experiments of Chapter 8. The drag reduction percentage, $DR\%$, is calculated as

$$DR\% = \left(1 - \frac{\Delta P_p}{\Delta P_w}\right) \times 100, \tag{4.1}$$

where ΔP_w and ΔP_p are pressure drops for water and polymeric flows, respectively. The pressure drop between two pressure ports with 1 m distance, see Figure 3.1, was measured using a Validyne DP-15 pressure transducer with 0.2 psi diaphragm and accuracy of 0.25% of the full-scale pressure. The demodulated signal of the pressure transducer was acquired by a data acquisition card with 12-bit resolution (National Instruments NI-9201 DAQ) at 100 Hz frequency. The uncertainty of the pressure measurement was approximately 3%, estimated by repeating the pressure drop measurement of the unladen water flow for five times.

Chapter 5

Dynamics and wall collision of spherical particles in near-wall turbulent channel flow

5.1 Introduction

One of the first measurements of the acceleration of inertial particles in a turbulent boundary layer was conducted by Gerashchenko et al. (2008). They recorded the two-dimensional trajectories of small (sub-Kolmogorov scale) airborne water droplets. The St_η of the droplets was in the range $0.035 \leq St_\eta \leq 1.2$ at a small mass loading of 0.01 %. The droplets close to the wall were characterized as having an average streamwise deceleration, i.e. $\langle A_x \rangle < 0$. Similar results were also obtained from numerical studies of turbulent particle-laden flows by Lavezzo et al. (2010), Zamansky et al. (2011) and Yu et al. (2016). These investigations used DNS for the fluid phase along with simplified versions of the Maxey–Riley equation for the solid phase. The numerical simulation of Lavezzo et al. (2010) was carried out for $0.87 \leq St_\eta \leq 11.8$, Zamansky et al. (2011) for $1 \leq St^+ \leq 25$ and Yu et al. (2016) at $St^+ = 35$. Each of these studies reported $\langle A_x \rangle < 0$ in the near-wall region and related it to the dominant effect of viscous force on the particles. There is, however, a discrepancy in the values of the average wall-normal acceleration, $\langle A_y \rangle$, as discussed below.

In the experiments of Gerashchenko et al. (2008), the droplets had $\langle A_y \rangle < 0$, with the positive axis pointing away from the wall. These droplets were sub-Kolmogorov and had

$r_\rho \sim 833$. Also, droplets did not rebound when they hit the wall, which is not the case for solid particles. The numerical simulations of Lavezzo et al. (2010) and Yu et al. (2016) also resulted in $\langle A_y \rangle < 0$ for both unladen and particle-laden flows in the near-wall region while the simulations of Zamansky et al. (2011) showed that $\langle A_y \rangle > 0$. All these numerical simulations assumed point-wise particles with $r_\rho \gg 1$ and neglected the pressure distribution on the particle, near-wall lift, added-mass, and Basset forces. These forces are important when the particles are larger than the smallest scale of the flow (Calzavarini et al., 2012). The aforementioned numerical studies also assumed elastic particle–wall interaction, and neglected wall repulsive forces and particle–particle collisions. Further development of the numerical simulations of turbulent particle-laden flows requires investigation of the effects of particle-related forces on their dynamics through collection and evaluation of experimental data.

The relationship between St and particle acceleration has been previously investigated in turbulent flows to understand particle dynamics. The investigations have shown the remarkable effect of St on the probability density function (pdf) and root-mean-square (rms) of particle acceleration, a. For example, Ayyalasomayajula et al. (2006) analyzed the effect of St_η on the acceleration distribution of droplets in grid turbulence, which is isotropic. It was found that increasing St_η from 0.09 to 0.15 narrowed the pdf of A_x and made its rms (i.e. a_x) smaller. This trend was also reported by Bec et al. (2006) who used DNS to investigate the effect of St_η on the pdf and rms of particles' acceleration with $St_\eta < 3.5$ in isotropic turbulent flows. The narrower tails of the acceleration pdf and its smaller a at higher St_η in isotropic turbulence have been related to the effect of particle inertia on its motion; inertial particles are less responsive to the fluid motion and more likely to move out of vortices (where there are high acceleration motions) to regions with higher strain (Eaton and Fessler, 1994; Ayyalasomayajula et al., 2006; Gerashchenko et al., 2008; Lavezzo et al., 2010).

In non-isotropic turbulence, as would occur near a wall, a different relationship between St_η and a_x has been reported. For example, in the experimental study mentioned earlier,

Gerashchenko et al. (2008) showed that increasing St_η from 0.07 to 0.47 increased a_x and suggested that this trend was because of the effect of gravity and mean shear on inertial particles. Lavezzo et al. (2010) conducted a DNS of particle-laden flow with and without gravity in non-isotropic turbulence to verify the effect of gravity on the relationship between St_η and a_x. The parameters of their simulation, including the r_ρ and St_η, were similar to those studied by Gerashchenko et al. (2008). In the study of Lavezzo et al. (2010), particles were able to collide with the wall and elastically rebound from it, in contrast to the droplets in the experiment of Gerashchenko et al. (2008). The comparison of the simulations of Lavezzo et al. (2010) with and without gravity confirmed that the increase in a_x with increasing St_η close to the wall is due to the combined effects of gravity and mean shear. They argued that the downward motion of the particles due to gravity exposes them to a strong deceleration due to the mean shear very close to the wall and causes high a_x. The analysis of Lavezzo et al. (2010) showed that with increasing St_η from 0.87 to 1.76, the a_x slightly increased even in the absence of gravity (although this increase was small compared with that obtained when gravity was considered), followed by a continuous decrease in the value of a_x as St_η was increased from 1.76 to 11.8. This non-monotonic variation of a_x with St in the absence of gravity was also found in the numerical study of Zamansky et al. (2011), who showed that in the near-wall, non-isotropic turbulence, the maximum value of a_x increased when St^+ increased from 1 to 5 and then decreased for higher St^+ (up to $St^+ = 25$). The results of the two numerical investigations indicate that other mechanisms in addition to gravity can decelerate the particles and increase a_x. In particular, the effects of particle–wall interaction on acceleration statistics of inertial particles must be investigated.

The effects of particle–wall interactions have been studied experimentally under quiescent and flowing conditions. Joseph et al. (2001) measured the wall-normal restitution coefficient, e_V, in fluids with different viscosities. Their experimental setup consisted of a spherical particle attached to a string. This pendulum was released from different initial angles and moved through a quiescent liquid until the particle hit a vertical wall with an impact angle of 90°. In their experiments, particle rebound did not occur (i.e. $e_V = 0$)

when St_V was below a critical value od $St_V \sim 10$. At values $10 < St_V < 30$, the e_V rapidly increased with increasing St_V (Joseph et al., 2001); however, with further increase in St_V, values of e_V increased more slowly and eventually asymptotically approached the value for dry collision (i.e. collision in the air). The dependency of e_V on St_V is also reported by Gondret et al. (2002), Stocchino and Guala (2005), and Legendre et al. (2006). Some other quiescent fluid studies also showed that e_V depends on the impact angle, θ_i, which is defined as the angle between the particle's velocity vector and the wall. For example, Salman et al. (1989) tested particle–wall collisions in the air and showed that an increase in θ_i reduced e_V. This reduction was also observed by Joseph and Hunt (2004). The dependence of e_V on θ_i in a turbulent flow of air was investigated by Sommerfeld and Huber (1999). They measured e_V, θ_i, and rebound angle, θ_r, of spherical particles in the air flowing through a horizontal rectangular channel. Their results also showed the reduction of e_V with increasing θ_i.

The dependence of e_V on θ_i shows the important role this angle plays in particle–wall collision in turbulent flows. The motion of particles in non-isotropic turbulent flows strongly depends on the turbulent structures interacting with the particles (Kaftori et al., 1995a,b; Marchioli and Soldati, 2002; Kiger and Pan, 2002). For example, sweep and ejection motions affect particles' flux toward and away from the wall (Ninto and Garcia, 1996; Soldati, 2005) and quasi-streamwise vortices are known to cluster small particles along low-speed streaks (Ninto and Garcia, 1996). Knowledge of the distributions of θ_i and e_V in a particle-laden turbulent flow is a key factor for modeling particle–wall interactions (Tsuji et al., 1987; Sommerfeld and Huber, 1999; Kosinski and Hoffmann, 2009; Sommerfeld and Lain, 2018).

In this chapter, the dynamics and wall-collision of inertial particles in a near-wall turbulent channel flow are investigated using 3D-LPT based on STB algorithm, detailed in Section 4.3. The STB algorithm was used to obtain the Lagrangian trajectories of the particles and determine their velocity and acceleration. The trajectories were also used to investigate the collision of the particles with the wall, with specific attention paid to θ_i, θ_r and particle momentum exchange with the wall.

The flow facility used for performing the experiments of this chapter is introduced in Sec-

tion 3.1. The measurement system, data processing, and uncertainty analyses are described in Section 4.3. The accuracy of the measurement system and the processing algorithm is also verified by comparing the measured velocity and acceleration statistics of unladen flow with DNS of unladen flow from Moser et al. (1999) and Yeo et al. (2010) in Section 5.3.1. The velocity and acceleration fields of the particles are investigated in Section 5.3.2. A quadrant analysis is performed to study the contribution of turbulent motions to Reynolds stresses and acceleration of the particles, detailed in Section 5.3.3. The collision of the particles with the wall is investigated in Section 5.3.5 using conditional averaging of particle velocity and acceleration based on the turbulent motions of particles and θ_i.

5.2 Experimental design

An unladen and a particle-laden experiment were performed with a similar mass flow rate of 1.76 kg/s and at a constant temperature of 20°, resulted in the $Re_H = 14,600$. The main parameters of the unladen flow, including U_b, inner scaling, and the Re_τ are shown in Table 5.1.

Re_τ	Re_H	U_b(m/s)	u_τ(m/s)	λ(μm)	t_τ(μs)
410	14,600	0.98	0.055	18.3	337

Table 5.1: The flow parameters describing the unladen flow. The inner scaling is calculated from the unladen velocity profile measured using the 3D-LPT.

The particle-laden flow consisted of G-125 particles dispersed in water at a volumetric concentration of $C_v = 0.03\%$, equivalent to a mass fraction of $C_m = 0.1\%$. For these glass particles and the test conditions under which they were studied, $St^+ = 4.5$. The U_s for particles was estimated as $U_s = |\langle U_f \rangle - \langle U_p \rangle|$. Using this estimation, the maximum Re_{ps} in the measurement domain was approximately 12.1. This Re_{ps} was an order of magnitude less than the threshold of $Re_{ps} = 110$, suggested for vortex shedding from spherical particles (Hetsroni, 1989). The properties of the particles studied here are summarized in Table 5.2. Particle–particle collisions were not expected to play a significant role at this concentration

(Elghobashi, 1994).

$d_p^+ = d_{50}/\lambda$	r_ρ	$C_v(\%)$	$C_m(\%)$	V_t (m/s)	Re_{ps}	t_p (ms)	St^+
7.4	2.6	0.03	0.1	0.015	12.1	1.50	4.5

Table 5.2: Properties of G-125 particles used in the particle-laden experiment. The V_t, Re_{ps}, t_p, and St^+ are determined based on the d_{50} of G-125 particles.

From a comparison of C_m and d_p^+ of the current investigation with previous studies, the effect of particles on the turbulent structures of the fluid phase is expected to be negligible, i.e. a marginal two-way coupling. The experimental results of Kulick et al. (1994) showed that 90μm glass particles with C_m of 2% and d_p^+ of 3 had a negligible effect on the turbulent intensity of the carrier phase. The numerical analysis of Nasr and Ahmadi (2007) for particles with d_p^+ of 2.2 and $C_m = 2\%$ also showed a negligible change of the flow turbulent kinetic energy and dissipation. In Kulick et al. (1994) and Nasr and Ahmadi (2007), the carrier phase was air, resulted in a higher r_ρ relative to the current study. Therefore, the smaller r_ρ of the present investigation is expected to result in an even smaller modulation of flow turbulence (Yu et al., 2017). Regarding the finite size of the particles, DNS of Luo et al. (2017) for particles with d_p^+ of 11.3 (without point-particle assumption), r_ρ of 3.3 and C_v of 0.1% showed a negligible effect on fluid turbulence. This observation was made in spite of turbophoresis and a larger near-wall particle concentration in their study.

The Lagrangian velocity and acceleration data were averaged in the streamwise and spanwise direction (in addition to time), due to homogeneity of the flow field in these directions. The wall-normal dimension of the averaging bins was one wall unit, λ, for the unladen flow. The bin size was larger and equal to 125μm for the particle-laden flow. More than 9×10^6 tracer trajectories for unladen flow from 27,000 images and approximately 2.3×10^6 particle trajectories in the particle-laden flow from 45,000 images were obtained using the STB algorithm. The random error of the velocity and acceleration statistics of unladen flow and particles were investigated based on the standard deviation of the last 20% of data collected at $y/H = 0.008$ (equivalent to $y^+ = 3.4$) and presented in Table 4.5.

The mean duration of particle trajectories was relatively constant and was approximately 20 ms for $y^+ > 20$. For smaller y^+, the mean trajectory duration gradually shortened to approximately 13 ms.

5.3 Results and discussion

5.3.1 Unladen turbulent channel flow

The unladen flow field statistics and the uncertainty of the 3D-LPT technique are evaluated by comparing the velocity statistics with the DNS results of Moser et al. (1999) at $Re_\tau = 395$ and the acceleration statistics with a separate DNS study of Yeo et al. (2010) at $Re_\tau = 410$. The normalized mean streamwise velocity (U^+), where $U^+ = \langle U \rangle / u_\tau$, is shown here as Figure 5.1(a). The 3D-LPT measurement agrees well with the DNS results of Moser et al. (1999) from the first data point at $y^+ = 3.4$ in the viscous sublayer up to the border of the measurement volume at $y^+ = 218$ ($y = 4$ mm) in the logarithmic region. The logarithmic law, $U^+ = (1/\kappa)\ln(y^+) + B$, with $\kappa = 0.4$ and $B = 5.2$ is also shown in this figure.

The non-zero components of the Reynolds stress tensor, $\langle u_i u_j \rangle$, determined from 3D-LPT measurement, are shown in Figure 5.1(b). The mean streamwise Reynolds stress profile, $\langle u^2 \rangle$, at the near-wall region of $y^+ \leq 12$ is slightly larger (4 % in the peak) than the DNS results, and the maximum is also closer to the wall by $\sim 2\lambda$. The difference can be partly attributed to the fact that the measurement was made at $Re_\tau = 410$ which results in a thinner inner layer and slightly larger values of $\langle u^2 \rangle / u_\tau^2$ than the Moser et al. (1999) simulation, where $Re_\tau = 395$. The profiles of mean wall-normal Reynolds stress, $\langle v^2 \rangle$, and mean spanwise Reynolds stress, $\langle w^2 \rangle$, overlap the DNS results and reach their maximum values at $y^+ = 70$ and 40, respectively. The mean Reynolds shear stress, $\langle uv \rangle$, also agrees well with the DNS data, and the minimum value is reached at $y^+ = 35$. The good agreement of the measurement with the DNS results also provides evidence indicating that (i) fully developed channel flow is established and (ii) the 3D-LPT can resolve the mean and second-order velocity statistics in the region $3.5 \leq y^+ \leq 218$.

The ability of the 3D-LPT technique in resolving the mean and second-order acceleration

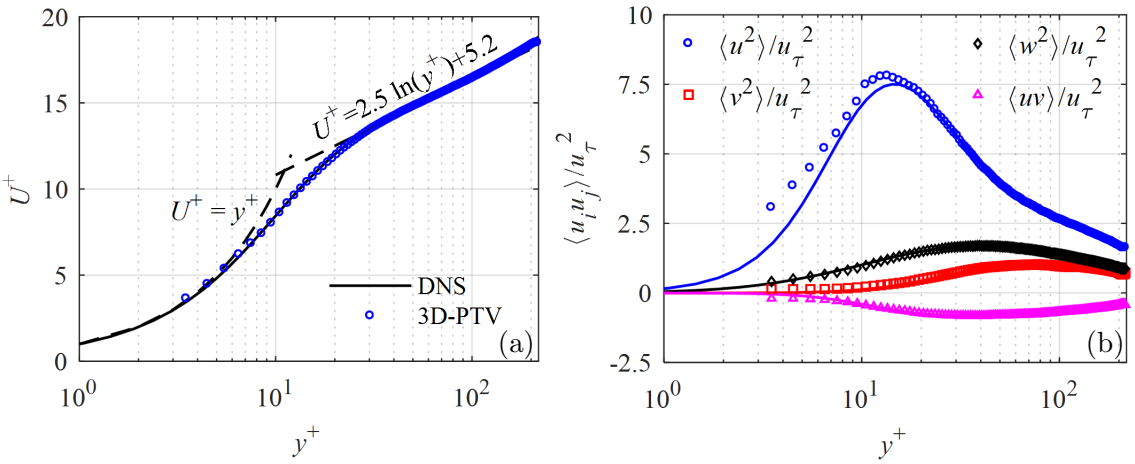

Figure 5.1: Comparison of 3D-LPT measurement of (a) mean streamwise velocity, and (b) non-zero components of Reynolds stress tensor in unladen flow at $Re_\tau = 410$ (symbols) with the DNS results of Moser et al. (1999) at $Re_\tau = 395$ (solid lines).

statistics is investigated by comparing the results of the measurement made for the unladen flow with the DNS results of Yeo et al. (2010) at $Re_\tau = 408$. The profiles of normalized mean streamwise acceleration $A_x^+ = \langle A_x \rangle / (u_\tau^3/\nu)$ and mean wall-normal acceleration, A_y^+, and mean spanwise acceleration, A_z^+, are presented in Figure 5.2(a) for the unladen flow. The measurements of A_x^+ and A_y^+ show good agreement with the DNS. At the locations where the minimum value of A_x^+ and the maximum value of A_y^+ occur ($y^+ = 8$ and 18, respectively), the difference between the experimental and DNS is approximately 4%. At $y^+ < 35$, A_x^+ is negative, which indicates flow deceleration. Yeo et al. (2010) attributed the negative value of A_x^+ in the near-wall region mainly to the viscous force within the solenoidal acceleration ($\equiv \nu \partial^2 \langle U \rangle / \partial y^2$). The negative A_x^+ at $y^+ < 35$ is also expected because of $A_x \equiv \partial \langle uv \rangle / \partial y$ (Chen et al., 2010). As it is well known, and seen in Figure 5.1(b), $\partial \langle uv \rangle / \partial y < 0$ in this region. At $y^+ < 70$, A_y^+ is positive as shown in Figure 5.2(a). This agrees with the DNS results of Yeo et al. (2010) at $Re_\tau = [180, 408, 600]$ and the DNS results of Zamansky et al. (2011) at $Re_\tau = 587$. The positive values of A_y^+ at $y^+ < 70$ is also expected since $A_y \equiv \partial \langle v^2 \rangle / \partial y$ (Chen et al., 2010) and $\partial \langle v^2 \rangle / \partial y$ is positive up to $y^+ \sim 70$ as observed in Figure 5.1(b). The variation of A_y^+ with y^+ also agrees with the variation of

$\partial\langle v^2\rangle/\partial y$ with y^+ in Figure 5.1(b). However, the trend of the values of A_y^+ measured for the present study is not in agreement with the DNS results of Lavezzo et al. (2010) at $Re_\tau = 300$ or Yu et al. (2016) at $Re_\tau = 150$, who reported negative A_y^+ values near the bottom wall of horizontal channel flows. The positive A_y^+ in the inner layer is attributed to the irrotational component of $\langle A_y\rangle$, i.e. $-\partial\langle p\rangle/(\rho\partial y)$, that accelerates the flow upward toward the axis of rotation of quasi-streamwise vortices (Lee et al., 2004; Lee and Lee, 2005; Yeo et al., 2010). The rotational motion of the quasi-streamwise vortices provides a mean low-pressure core at $y^+ \sim 20$ (Kim et al., 1987). This is consistent with the location of the maximum value of A_y^+ at $y^+ = 18$ in Figure 5.2(a). The trends of the wall-normal variation of $\langle A_x\rangle$ and $\langle A_y\rangle$ of the unladen flow in the current study are also consistent with the experimental and DNS results of Stelzenmuller et al. (2017). For a spanwise homogeneous flow, A_z^+ is expected to be zero. The maximum deviation of A_z^+ from zero is approximately 7.3×10^{-4} and occurs at $y^+ = 4.5$, which is an indication of small measurement uncertainty.

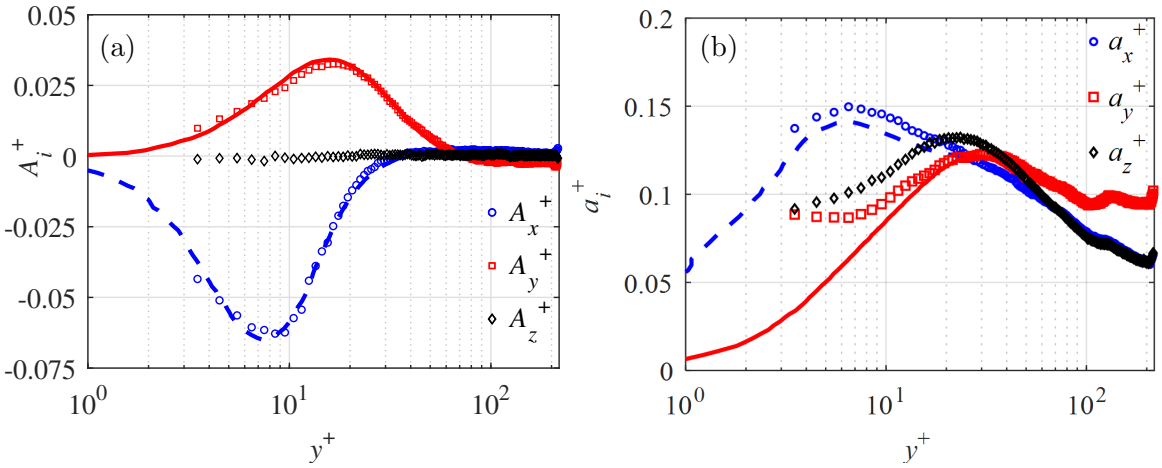

Figure 5.2: The 3D-LPT measurement (symbols) of (a) mean acceleration, and (b) rms of acceleration for the unladen flow at $Re_\tau = 410$. The results are normalized with inner scaling and compared with the DNS results of Yeo et al. (2010) at $Re_\tau = 408$ (dashed and solid lines).

The normalized rms of the acceleration components are presented in Figure 5.2(b) as $a_i^+ = a_i/(u_\tau^3/\nu)$, where $i = x, y$ and z, and are compared with the results of the simulations of Yeo et al. (2010). There is a good agreement between the measured and the DNS values

of a_x^+, with a maximum difference of approximately 6% at the maximum value of a_x^+, which occurs at $y^+ = 6$. The measured values of a_y^+ are in accord with the DNS profiles at $y^+ > 30$, with a difference of approximately 2 % for the maximum value of a_y^+ (at $y^+ = 30$). At $y^+ = 10$, the measured a_y^+ deviates from DNS while the profile of a_x^+ follows the DNS. This is due to the higher relative error in the y (and z) directions compared with the x-direction; the displacement of particles in the y (and z) is an order of magnitude smaller than that in the x direction. The maximum values of a_y^+ and a_z^+ are in the buffer layer (farther away from the wall than the maximum value of a_x^+), which suggests that they are pressure driven due to vortical structures (Yeo et al., 2010). It is also noticeable in Figures 5.2(a) and 5.2(b) that the magnitudes of a_x^+ and a_y^+ are greater than the magnitudes of A_x^+ and A_y^+, respectively, showing the intermittency of the events with high acceleration in the flow.

5.3.2 Particle-laden turbulent channel flow

The distribution of the particle number density in the near-wall region is presented in Figure 5.3. This distribution is determined based on the number of particles in each bin divided by the average number of particles across all the bins and represented by $\bar{N}$. The wall-normal location is normalized by λ. The averaging bin size for particles is equal to 125μm and the first data point is obtained at the center of the first bin immediately after the wall, i.e. at $y^+ = 3.4$. For this analysis, all the detected particles are considered, as no limitation is imposed on their trajectory length. As expected, the concentration of particles is higher close to the wall due to gravity. The figure also demonstrates that local near-wall number density can be up to 2.2 times larger than the average number density within the measurement domain, i.e. $y^+ < 218$. The relatively small increase of local number density in the vicinity of the wall suggests that modulation of the liquid phase turbulence by the particles is small.

The velocity and acceleration statistics of particles obtained from the 3D-LPT measurement at $Re_\tau = 410$ are also investigated in this section. The velocity statistics are

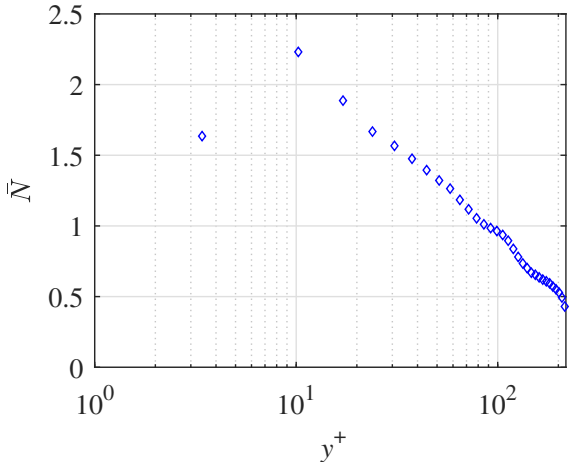

Figure 5.3: The normalized number density of particles in the near-wall region.

normalized using u_τ, and the acceleration statistics are normalized using u_τ^3/ν. The U^+ profiles of particles and the unladen flow are compared in Figure 5.4(a). The particle velocity is greater than that of the unladen flow at $y^+ < 10$ as the no-slip boundary condition does not apply to the particles. As a result, $\langle U_\mathrm{f} \rangle - \langle U_\mathrm{p} \rangle$ is negative; specifically, it is -0.09m/s at $y^+ = 3.4$ which is approximately 10% of the bulk velocity. At $y^+ > 10$, the particle velocity is lower than that of the unladen flow. A similar observation was reported by Shao et al. (2012) and Yu et al. (2016) and is associated with the larger inertia of particles (compared with that of the liquid phase). The trend of the U^+ profile is consistent with the results presented by others including Kussin and Sommerfeld (2002), Shao et al. (2012) and Yu et al. (2016) for different values of Re_τ and St. The mean wall-normal velocity of unladen flow and particles is also normalized by u_τ as $V^+ = \langle V \rangle / u_\tau$, and presented in Figure 5.4(b). The value of V^+ is close to zero for unladen flow in the whole measurement domain. However, particles have a small negative V^+, showing their motion toward the lower wall. Therefore, the gravitational settling of particles is not totally balanced by turbulence diffusion. The former gradually accumulates the particles close to the wall, as seen in Figure 5.3.

The normalized non-zero components of the Reynolds stress tensor of particles and the unladen flow are compared in Figure 5.4(c), showing similar trends and approximately the same peak locations for the associated components. particles have larger $\langle u^2 \rangle$ in comparison

with the unladen flow. Due to inertia, the particles can maintain their velocity for a longer time, and therefore over a longer wall-normal distance, relative to the fluid motions. As a result of this larger diffusion, a wider distribution of particle velocity, i.e. a larger velocity fluctuation, is observed (Shokri et al., 2017; Ahmadi et al., 2019). The maximum of the absolute value of $\langle uv \rangle$ of particles, $|\langle uv \rangle|_{\max}$, is approximately 30% larger than it is for the unladen flow, which indicates a greater correlation between their u and v and turbulence production. Shokri et al. (2017) compared the measured $\langle uv \rangle$ of inertial particles with the unladen flow in an upward turbulent vertical pipe flow. Their results showed that the $|\langle uv \rangle|_{\max}$ of particles (with St^+ values of 3.9 and 7.7) was approximately 30% larger than the unladen flow. However, at $St^+ = 14$, $|\langle uv \rangle|_{\max}$ became 27% smaller than $|\langle uv \rangle|_{\max}$ for the unladen flow, indicating that the difference between $|\langle uv \rangle|_{\max}$ of particles and unladen flow is strongly dependent on St^+. The DNS results of Yu et al. (2017) showed a similar effect of St on the difference between $|\langle uv \rangle|_{\max}$ of particles and unladen flow in horizontal turbulent channel flows.

The normalized mean and rms of particles acceleration are compared with the numerical results of Zamansky et al. (2011) in Figure 5.5. This numerical simulation was carried out for small particles ($d_p^+ < 1$) with a large density ratio ($r_\rho = 770$). For this flow regime, Zamansky et al. (2011) assumed point-particles, and the steady-state drag was the only force taken into account for the solid phase equations of motion. The effect of the added-mass, Basset, Saffman, Magnus and gravity forces were neglected. In the experiment, d_p^+ is larger and r_ρ is smaller. However, the numerical simulation is performed with $St^+ = 5$ and $Re_\tau = 587$, which are close to the St^+ and Re_τ of the current experiment. It should be noted that the comparison with the numerical simulation is not carried out here to evaluate the uncertainty of the 3D-LPT or the validity of the assumption for the numerical simulation. Here, we qualitatively compare the acceleration statistics of the experiment and the numerical simulation. The comparison also allows us to evaluate if the point-particle assumption is valid for the flow condition of the experiment. To the authors' knowledge, this simulation is the best in comparison to the results of the current study, especially when

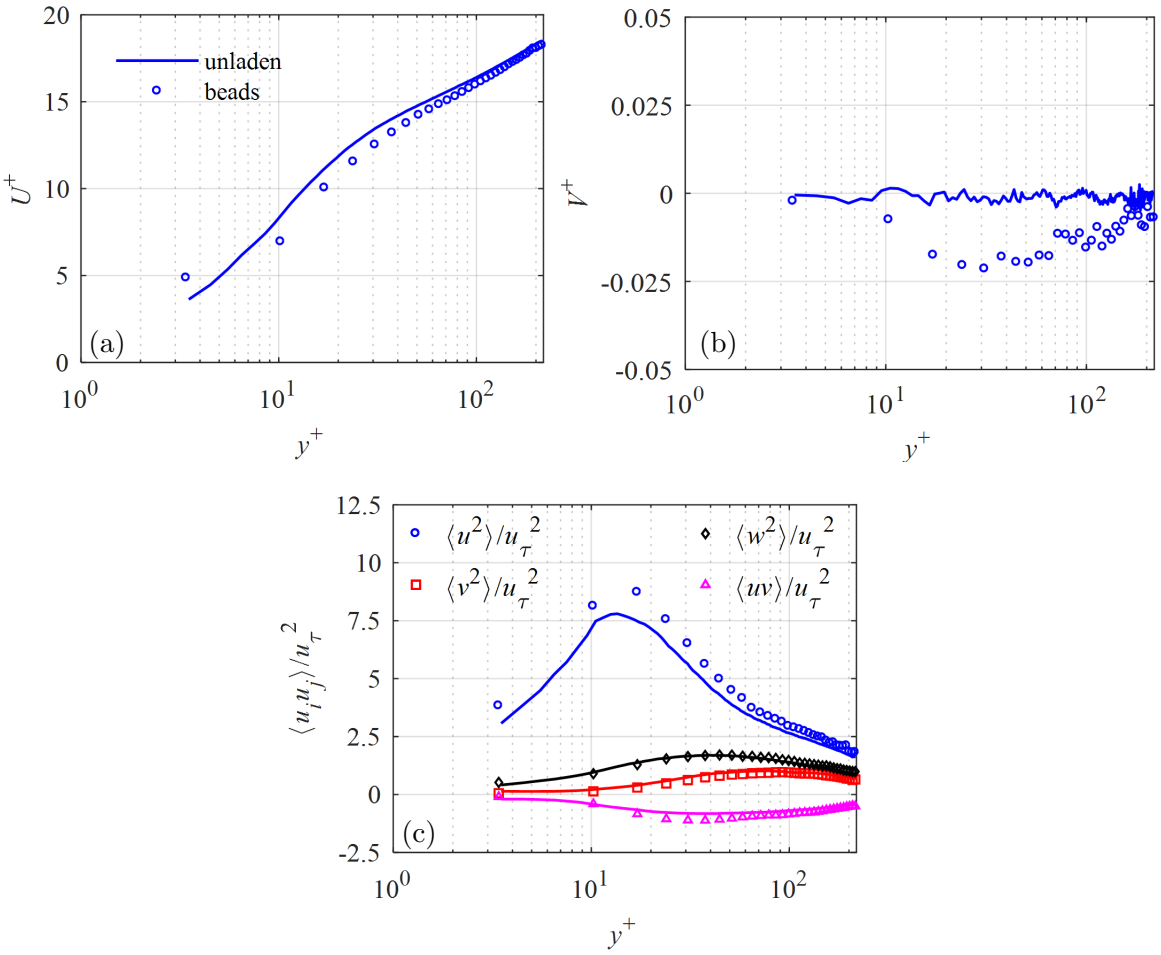

Figure 5.4: Comparison of 3D-LPT measurements of (a) mean streamwise velocity, (b) mean wall-normal velocity and (c) mean Reynolds stresses of particles (symbols) with the same parameters for the unladen flow (solid lines) at $Re_\tau = 410$.

one considers that mean and rms of acceleration are needed for the comparison.

From the A_x^+ profile of particles, presented in Figure 5.5(a), particle deceleration ($A_x^+ < 0$) occurs at $y^+ < 20$ with the minimum value of A_x^+ occurring at $y^+ \sim 10$. particle deceleration is attributed to the slower viscous-dominated flow of the surrounding near-wall fluid and the interaction of particles with the wall. It is notable that the location of the minimum value of A_x^+ is close to the location of the minimum value of $\partial\langle uv \rangle / \partial y$ for particles as shown in Figure 5.4(c). Lavezzo et al. (2010) used DNS of a particle-laden flow, with $St_\eta = [0.87, 1.76, 11.8]$ to show that $\langle A_x \rangle$ and $\partial\langle uv \rangle / \partial y$ are related for inertial particles.

The current experimental investigation also confirms this relation. The measured value at $y^+ = 3.4$ is $A_x^+ = -0.038$, while the numerical result at this location is $A_x^+ = -0.019$. This difference cannot be due to the different values of St^+ for as shown by Zamansky et al. (2011), increasing St^+ from 1 to 5 does not considerably affect A_x^+ at this near-wall position. It also is not expected that the higher value of Re_τ in the numerical study compared with the measurement is the reason for the difference in A_x^+ at $y^+ = 3.4$. Yeo et al. (2010) showed that increasing Re_τ enhances the viscous force contribution and increases the deceleration; but this increment is negligible for $Re_\tau > 400$. The difference between the measured A_x^+ and the numerical result at $y^+ = 3.4$ is attributed to the larger particles, smaller r_ρ and the particle–wall collision in the experiment. In the present study, the location of $A_x^+ = 0$ for particles is at $y^+ \sim 20$, which is closer to the wall than was found by Zamansky et al. (2011). Comparison of the A_x^+ profiles for the solid-phase, Figure 5.5(a), and the unladen flow, Figure 5.2(a), shows that the two are different when $y^+ > 20$: the unladen profile is relatively constant at a small positive value while for particles there is a local maximum at $y^+ \sim 40$, just above the buffer layer where $\partial\langle uv\rangle/\partial y$ is also positive, as shown in Figure 5.4(c). The difference is mainly associated with the acceleration of the particles that are ejected away from the wall. The region of positive A_x^+ overlaps with the logarithmic layer and indicates where fluid applies a net positive force on the particles to accelerate them. The streamwise velocity difference between particles and fluid results in a drag force (Crowe et al., 2012), which causes a local maximum of A_x^+ at $y^+ \sim 40$.

The maximum value of A_y^+ is found at $y^+ \sim 18$ of Figure 5.5(a). This is the same location of the maximum value of $\partial\langle v^2\rangle/\partial y$, as shown in Figure 5.4(c), as well as the location of the maximum A_y^+ for the unladen flow, as shown in Figure 5.2(a). This location is also near the mean axis of rotation of quasi-streamwise vortices, which is found at approximately $y^+ \sim 20$ (Kim et al., 1987) where a minimum pressure is expected. The positive acceleration can be associated with the ejection motions of the fluid, which lift up the particles and transport them away from the wall (Kiger and Pan, 2002). For particles moving toward the wall, their V should decrease to result in a positive A_y^+. In the region $18 < y^+ < 40$, A_y^+ decreases

and becomes zero at $y^+ \sim 40$. Figure 5.5(a) shows that at $y^+ < 20$, the A_y^+ of particles is larger than the A_y^+ reported by Zamansky et al. (2011). After the zero A_y^+ point, the effect of gravity becomes dominant and the A_y^+ of particles becomes negative. The negative A_y^+ values were not observed in the numerical results of Zamansky et al. (2011) in which gravity was not considered. As expected, the A_z^+ of particles is almost zero in the whole measurement domain. The maximum deviation of A_z^+ from zero is approximately 8.5×10^{-4} at $y^+ = 17$.

Considering the rms of the particle acceleration in Figure 5.5(b), the maximum value of a_x^+ of particles coincides with the location of the minimum value of A_x^+ in Figure 5.5(a). The maximum value of a_x^+ is larger than those of Zamansky et al. (2011). For unladen flow, Yeo et al. (2010) observed that as Re_τ increases from 408 to 600, the maximum value of a_x^+ increases by 3%. The numerical results of Zamansky et al. (2011) showed that the relationship between St^+ and a_x^+ is not monotonic: a_x^+ increased with increasing St^+ from 1 to 5, but decreased with further increases in St^+. The greater values of a_x^+ at $St^+ \sim 5$ compared to its values at the other St^+ in their simulations is associated with the balance between the particles' response to the surrounding fluid and their wall-normal dispersion. The wall-normal dispersion is expected to initially increase with increasing St^+, which results in acceleration/deceleration of particles when transported to different fluid layers, thereby increasing a_x^+ . The maximum value of a_y^+ in the measurement is also greater than that of the simulation. Again, the difference between a_x^+ and a_y^+ of the current measurement and those reported by Zamansky et al. (2011) in the immediate vicinity of the wall is mainly associated with the larger particles and the smaller r_ρ in the experiment. The discrepancy suggests that the point-particle assumption cannot be applied to the conditions of the current experiment. The fully elastic particle–wall collision assumption applied in the numerical simulation and measurement noise can also contribute to the discrepancy in particle's acceleration rms in the immediate vicinity of the wall.

The probability density functions of the components of the particle mean acceleration normalized with the rms of total acceleration, a, taken at five different y^+, are presented

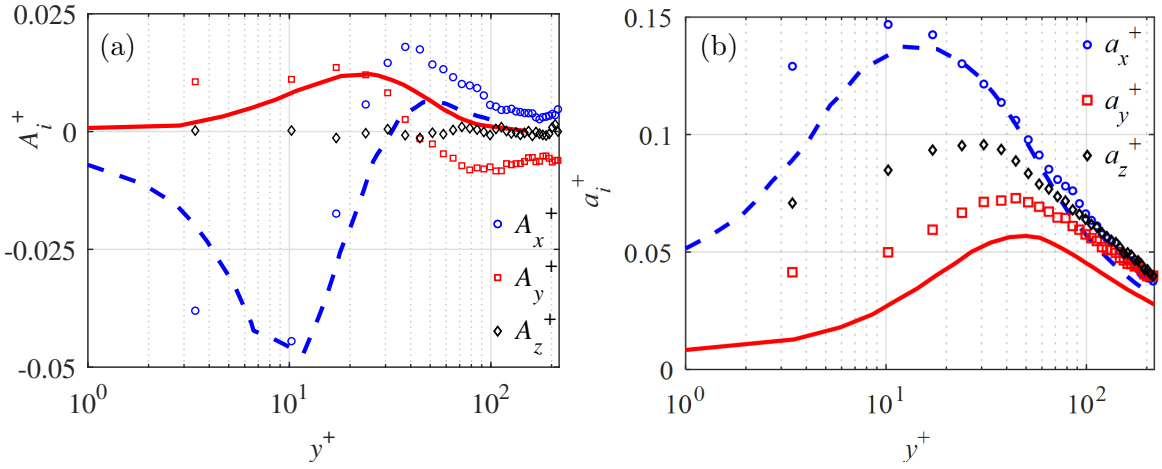

Figure 5.5: Comparison between measurement of normalized (a) mean acceleration and (b) rms of acceleration components from the 3D-LPT (symbols) with the numerical results of Zamansky et al. (2011) at $Re_\tau = 410$ with $St^+ = 5$ (lines).

in Figure 5.6. As Figure 5.6(a) shows, at $y^+ = 3.4$ and 10.2, the pdf of A_x is skewed towards negative A_x, which is consistent with the results of Figure 5.5(a) and the pdfs produced from the measurements of Gerashchenko et al. (2008). It is conjectured that the negative skewness of the pdf is due to the deceleration of particles by strong near-wall viscous forces and the particles' interaction with the wall. With increasing y^+, the viscous dominated deceleration reduces, and particles accelerate due to inertial forces. At $y^+ = 17$, the pdf is more symmetric. With further increases in y^+ to 44.3 and 98.8, the pdf becomes right-skewed, which shows more particles tend to have positive A_x.

The pdf of A_y shown in Figure 5.6(b) has a different behavior than was described above for A_x. Close to the wall and up to $y^+ = 44.3$, the pdf is right-skewed, indicating that more particles tend to have a positive A_y, which means the value of V of upward-moving particles increases or the value of V of downward moving particles decreases. The positive A_y can be associated with several forces. As it was mentioned, ejection motions of the liquid phase are known to lift up and accelerate particles away from the wall (Kiger and Pan, 2002). It is conjectured that the negative wall-normal pressure gradient also contributes to the positive A_y of the upward moving particles. This pressure gradient has been attributed to

a region of high vorticity where there is a larger accumulation of quasi-streamwise vortex cores located (Kim, 1989; Yeo et al., 2010). In the high-shear near-wall region, particles can also experience a large Magnus force. For a downward moving particle, the value of V is hypothesized to decrease due to the wall-normal pressure gradient and the increasing pressure of the fluid layer between the particle and the wall, known as wall repulsive force (Feng et al., 1994). By increasing y^+, the effect of these forces reduces, and particles experience a negative acceleration due to gravity. At $y^+ > 44.3$, the A_y pdf is skewed to the negative side, indicating that a large number of the particles with upward motion slow down, and downward moving particles speed up under the effect of gravity. The pdf of spanwise acceleration in Figure 5.6(c) is symmetric as expected.

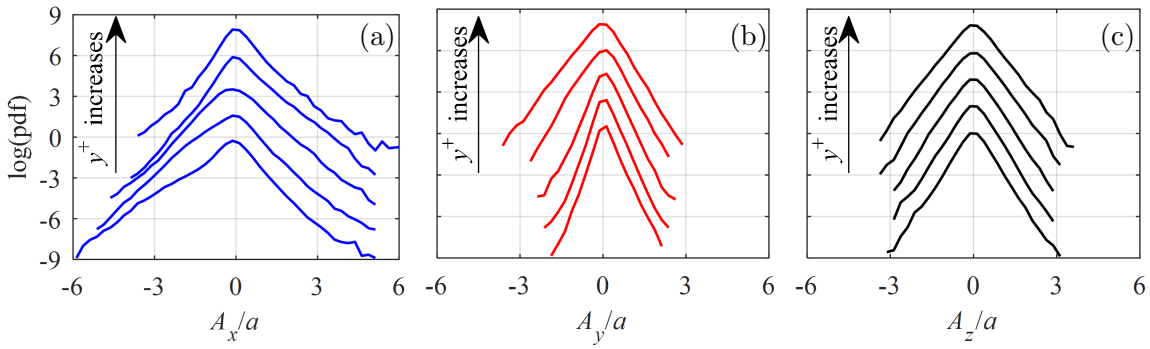

Figure 5.6: Probability density functions of mean (a) streamwise, (b) wall-normal and (c) spanwise acceleration of particles. The curves in each plot, from bottom to top, correspond to $y^+ = 3.4$, 10.2, 17, 44.3, 98.8. The pdfs are each shifted up by two units of the vertical axis for clarity.

5.3.3 Quadrant analysis

The turbulent motion of the fluid and particles can be further analyzed by plotting u and v in a quadrant plot. The motions described by the four quadrants are: Quadrant 1 (Q_1), upward interactions with $u > 0$ and $v > 0$; ejections (Q_2) with $u < 0$ and $v > 0$; downward interactions (Q_3) with $u < 0$ and $v < 0$; and sweeps (Q_4) with $u > 0$ and $v < 0$, as originally proposed by Wallace et al. (1972). To evaluate the contribution of each quadrant to $\langle uv \rangle$, the motions of the unladen flow and particles are sampled based on the u and v

signs of each quadrant. The conditionally sampled data are averaged as indicated by $\langle uv \rangle_{Q_i}$, where i varies from 1 to 4, referring to the four $u-v$ quadrants. Figure 5.7(a) shows the contribution of Q_1 and Q_3 while Figure 5.7(b) shows the contribution of Q_2 and Q_4. Based on the sign of $\langle uv \rangle$ and the positive $\partial \langle U \rangle / \partial y$ on the lower wall of the channel, the motions in Q_1 and Q_3 are associated with the reduction of turbulence while motions represented in Q_2 and Q_4 generate turbulence. Comparison of Figure 5.7(a) with Figure 5.7(b) shows that there is poorer correlation of u and v for the particles in Q_1 and Q_3 than observed for the unladen flow; however, the particles with ejection and sweep motions in Q_2 and Q_4 have higher $\langle -uv \rangle$ compared with the unladen flow. Therefore, particles have a larger $\langle uv \rangle$ in the near-wall region which is consistent with their $\langle uv \rangle$ profile in Figure 5.4(c). For the unladen flow, the sweep motion contributes more to turbulence production than ejection motions at $y^+ < 15$. Farther from the wall at $y^+ > 15$, the ejections become dominant as also observed in the DNS results of Kim et al. (1987). The particles with sweep and ejection motions also show a similar trend with the transition between sweep and ejection regions at $y^+ = 20$.

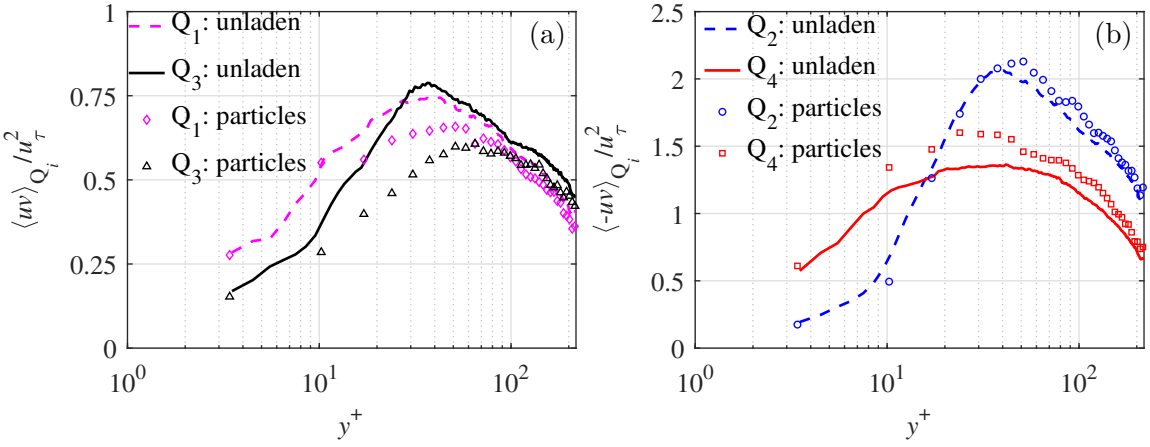

Figure 5.7: Conditional average of Reynolds shear stress of the unladen flow and particles based on motions in the (a) first and third, and (b) second and fourth $u-v$ quadrants.

The quadrant analysis is extended in Figure 5.8 to conditionally averaged acceleration, A^+_{x,Q_i}, of the unladen flow and particles to identify the contribution of quadrant motions

to A_x^+. The particles with $v > 0$ (Q_1 and Q_2) gain momentum from the high-speed region by moving away from the wall and have $A_x^+ > 0$, except for Q_1 at $y^+ < 40$ where the viscous forces are dominant. At $y^+ < 20$, only ejection motions of Q_2 result in positive A_x^+ . The maximum of the conditionally averaged A_x^+ based on Q_2 for both the unladen flow and particles is almost at the outer boundary of the buffer layer, or $y^+ \sim 30$. At this location, the viscous effects diminish and the surrounding fluid accelerates the ejected fluid and particles. The larger wall-normal displacement of particles due to their inertia moves them farther into the high-speed region. This results in a higher drag force on the ejected particles compared with the ejected fluid. Therefore, the positive A_x^+ of particles is larger than that of the fluid, as shown in Figure 5.8(b). It is also seen in this figure that in the near-wall region, sweep motions have $A_x^+ < 0$ for both the unladen flow and particles. The conditionally averaged A_x^+ based on Q_4 for unladen flow has a minimum at $y^+ \sim 8$ while the minimum for particles is found at $y^+ \sim 10$. The locations of the minimum values of these conditional averages are consistent with the locations of the minimum values of A_x^+ shown in Figure 5.2(a) and Figure 5.5(a), respectively. Comparison of Figures 5.8(a) and 5.8(b) shows that for both the unladen flow and particles, ejections and sweeps (Q_2 and Q_4 quadrants) are the major turbulent motions which provide positive and negative A_x^+, respectively.

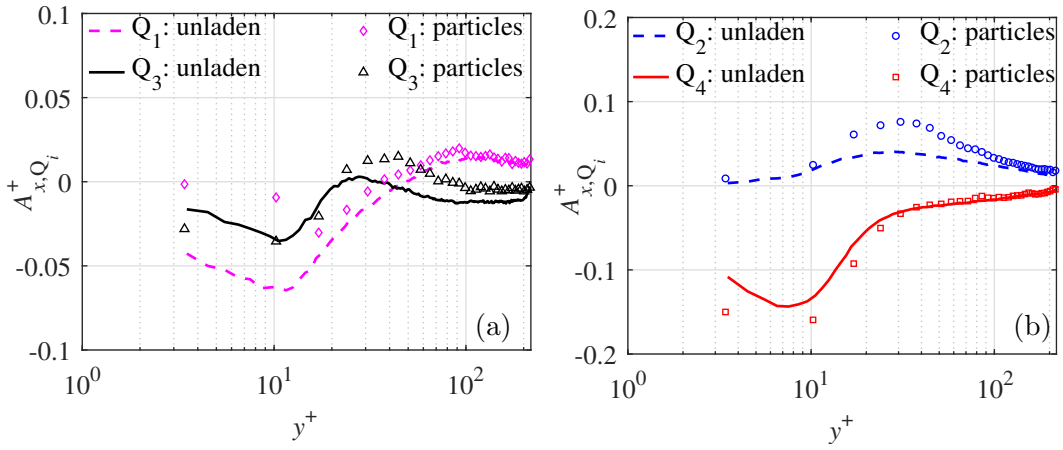

Figure 5.8: Conditional average of A_x^+ based on the motions in (a) first and third quadrants, and (b) second and fourth quadrants.

The conditionally averaged A_y^+ values, based again on $u-v$ quadrant analysis, are shown in Figure 5.9 for the unladen and particle-laden flows. As this figure shows, the positive A_y^+ of unladen flow is due to fluid elements with $v > 0$ (Q_1 and Q_2) in the whole near-wall region as well as sweep motions (Q_4) at $y^+ < 100$. The wall-normal pressure gradient induced by the low-pressure cores of the quasi-streamwise vortices pulls the flow upward and provides $A_y^+ > 0$. At $y^+ < 100$ for the unladen flow it is only the motions in Q_3 that have a negative contribution to A_y^+. Similar trends are observed for particles but the values of A_y^+ are smaller because of gravity and their larger inertia compared with the unladen fluid flow. The Q_2 and Q_4 profiles for particles show that ejection and sweep motions have a similar contribution to A_y^+ for the near-wall region: they both have $A_y^+ > 0$ at $y^+ < 40$ and $A_y^+ < 0$ at $y^+ > 40$. Figure 5.9 shows that for both unladen flow and particles, Q_1 and Q_3 have the major contributions to positive and negative A_y^+, respectively.

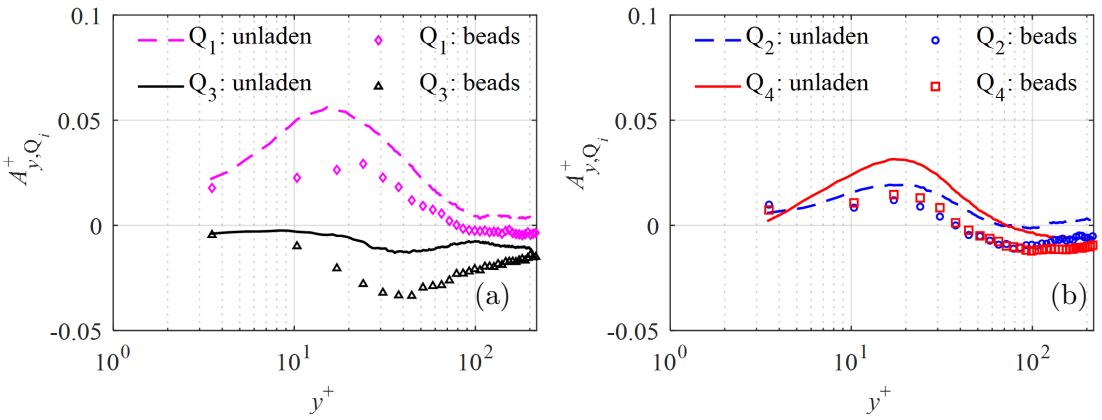

Figure 5.9: Conditional average of A_y^+ based on the motions in the (a) first and third quadrants, and (b) second and fourth quadrants.

5.3.4 Temporal scales

The temporal autocorrelation of particles' motion is investigated here to characterize their time scales at different wall-normal distances. For a variable S, the autocorrelation coefficient is determined as $C_{SS}(t^+) = \langle S(t_0^+)S(t_0^+ + t^+)\rangle / \langle S^2(t_0)\rangle$, where $S(t_0^+)$ is the value of S at the initial time step of t_0^+, and t^+ is the time shift. This autocorrelation is calculated

from the time-resolved values of U, V, W and θ along the particle trajectories. The results are shown in Figure 5.10 at five different y^+. In general, all the autocorrelation coefficients decrease with increasing t^+. The C_{UU} coefficient indicates that the streamwise velocity of the particles stays correlated for a longer time since C_{UU} stays positive for a long t^+, beyond the investigated range. However, C_{VV}, C_{WW} and $C_{\theta\theta}$ coefficients reach close to zero within $t^+ < 100$ for all the investigated y^+.

The autocorrelation coefficients approach zero at a larger gradient with decreasing y^+, which indicates a smaller time scale of the particles' motion. This is expected as the turbulent structures of fluid phase also become smaller with decreasing y^+. However, C_{VV} and $C_{\theta\theta}$ at $y^+ = 3.4$ demonstrate a different trend due to the presence of local minimums and negative values. At $y^+ = 3.4$, with increasing t^+, there is an initial and rapid decrease of C_{VV} to a local minimum at $t^+ = 11$. This is followed by a small increase and then a reduction to negative values at $t^+ = 20$. For the same wall-normal location of $y^+ = 3.4$, $C_{\theta\theta}$ rapidly decreases and reaches a local minimum also at $t^+ = 11$. The time shift, t^+, to reach negative C_{VV} and $C_{\theta\theta}$, both indicate the time scale when the particle changes its wall-normal direction of motion, shifts from upward to downward motion, and vice versa. However, the local minimum is more pronounced for $C_{\theta\theta}$ since θ is strongly modulated by the small magnitude of U according to $\theta = \tan^{-1}(V/U)$. Therefore, change in the direction of a weak wall-normal motion (small V) can result in a significant change of θ if U is small.

5.3.5 Particle-wall interaction

In this section, the effect of the wall is analyzed on particles with a wall separation distance of $y < 125\mu$m, where y is the distance between the particle center and the wall. The trajectory, velocity, and acceleration of these near-wall particles are investigated. In addition, the temporal scales of the near-wall trajectories and their collision with the wall are statistically characterized. The particle trajectories are analyzed based on the trajectory angle, θ, which is defined as $\tan^{-1}(V/U)$. Based on this definition and as seen in Figure 5.11 , a particle which is approaching the wall (i.e. $V < 0$) has a negative θ and a particle which is moving

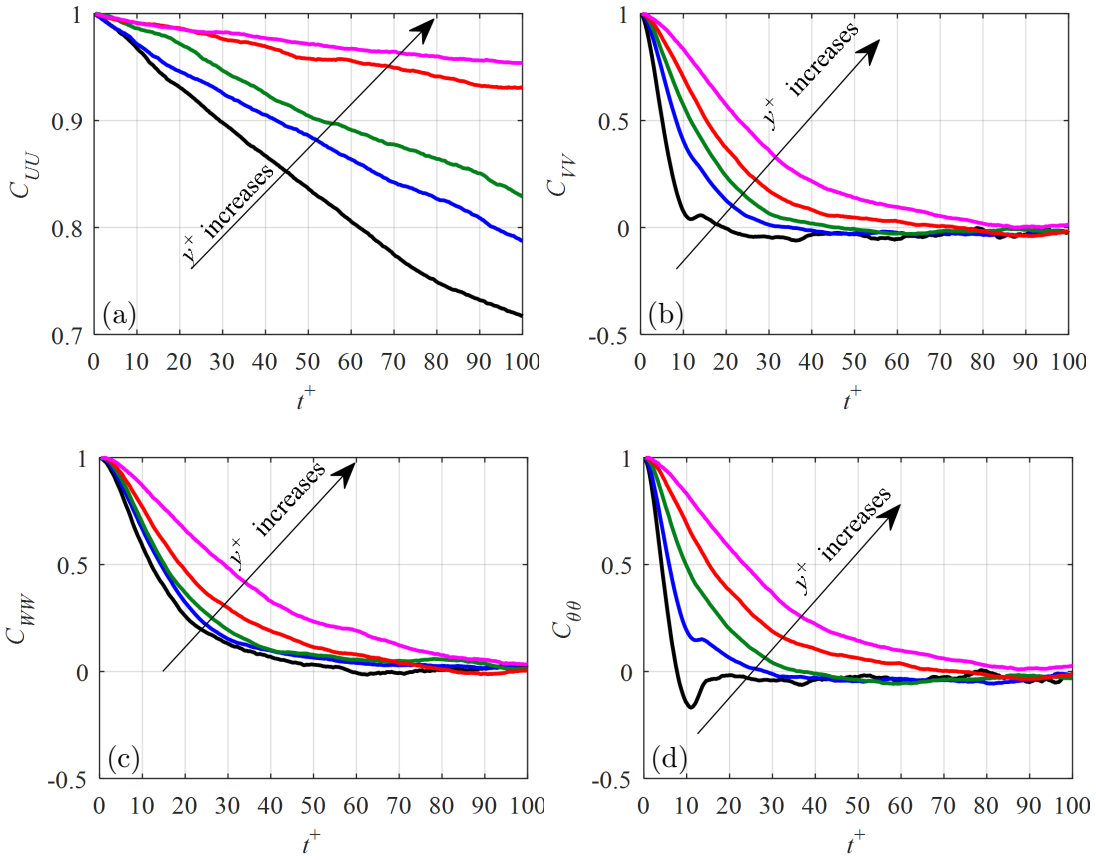

Figure 5.10: Temporal autocorrelation of (a) U, (b) V, (c) W and (d) θ of particles. The curves in each plot, from bottom to top, correspond to $y^+ = 3.4$, 10.2, 17.0, 44.3 and 98.8.

away from the wall (i.e. $V > 0$) has a positive θ. For a particle colliding with the lower wall of the channel, the impact angle, θ_i, and rebound angle, θ_r, are defined as the trajectory angle of the particle before and after a collision, respectively. In total, more than 80,000 particle trajectories at $y < 125\mu$m were detected from 5 seconds of time-resolved 3D-LPT data.

5.3.5.1 Trajectory angle

To scrutinize the relation of θ with velocity fluctuations for the particles at $y < 125\mu$m, the joint probability density function (jpdf) of θ and u/u_τ, and the jpdf of θ and v/u_τ are shown in Figures 5.12(a) and 5.12(b), respectively. The jpdf has a drop-shaped contour with a large variation of θ for large negative u, and a small variation of θ for large positive

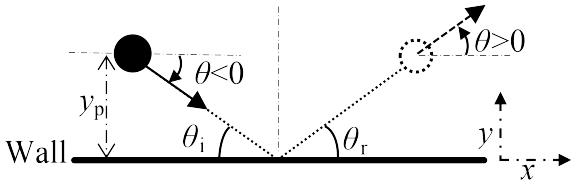

Figure 5.11: A schematic to define the parameters used to characterize particle collision with the lower wall of the channel.

u. Therefore, the smaller is the instantaneous streamwise velocity of the particle, U, the wider is the distribution of θ. This relation is pronounced here, since the mean streamwise velocity, $\langle U \rangle$, is small in the vicinity of the wall. The relation between θ and v is as expected; a positive v results in a positive θ, and vice versa. It is also observed that distribution of θ becomes wider with increasing v.

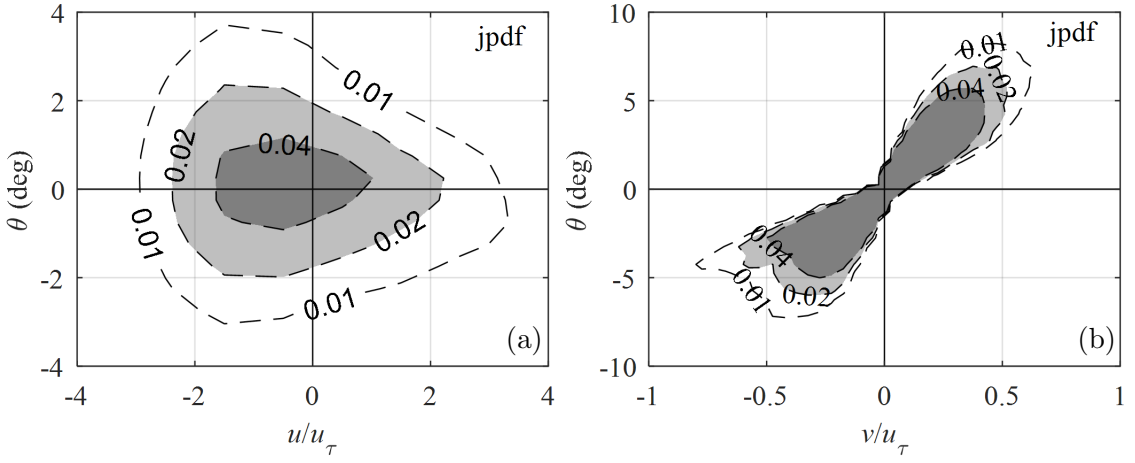

Figure 5.12: Joint probability density function of (a) u/u_τ and θ, and (b) v/u_τ and θ, for particles with $y < 125\mu$m.

The pdf of θ for particles in the vicinity of the wall at $y < 125\mu$m, i.e. $y^+ = 3.4$, and higher y^+ locations, is shown in Figure 5.13. The pdf for $y^+ = 3.4$ has a larger peak at $\theta = 0$, while the tails of the pdf extend to large positive and negative θ, reaching $\pm 20°$. This peaky behavior of the pdf reduces with increasing y^+. At higher y^+, the peak of the pdf attenuates and shifts towards negative θ, which means that most of the trajectories descend toward the wall. It is also observed that the tail of the pdf disappears with increasing y^+

as the probability of large θ becomes negligible. Therefore, the larger θ events are limited to the vicinity of the wall where the instantaneous streamwise velocity of the particles is small.

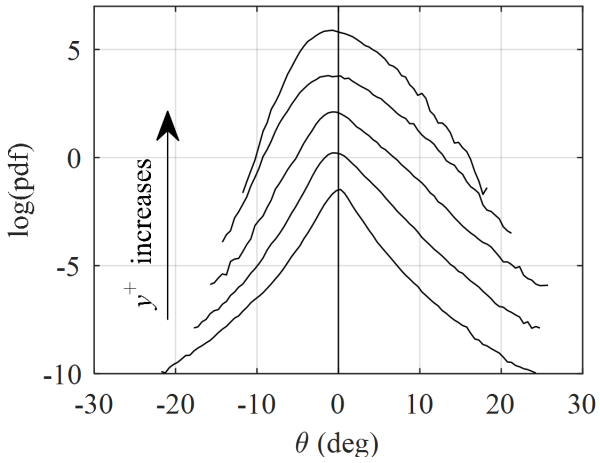

Figure 5.13: The pdf of θ for particles at $y^+ = 3.4$, 10.2, 17.0, 44.3 and 98.8, from bottom to top, respectively. The pdfs are shifted up by two units of the vertical axis for clarity.

5.3.5.2 Velocity and acceleration

Conditional averaging is applied here to investigate the contribution of each quadrant of velocity fluctuations to instantaneous velocity and acceleration of the near-wall particles, i.e. $y < 125\mu$m. First, to characterize the distribution of the motions, jpdf of u and v fluctuations of the particles is presented in Figure 5.14. The jpdf is relatively symmetric with respect to the horizontal axis ($v = 0$). Most of the particles have $u < 0$ caused by (i) the fluid viscous force, as the surrounding fluid has a lower velocity than particles and (ii) particle–wall interactions. The contours are also slightly shifted toward $v > 0$ and more particles are in the second quadrant (Q_2) than in the third quadrant (Q_3). Considering the smaller U of the fluid than the particles due to the no-slip boundary condition at $y^+ = 3.4$, the Saffman force at this location should be downward. Therefore, it is the ejection motions, Magnus lift force, and wall collision, which can move the particles away from the wall and cause $v > 0$.

The relation between instantaneous velocity and the absolute value of trajectory angle,

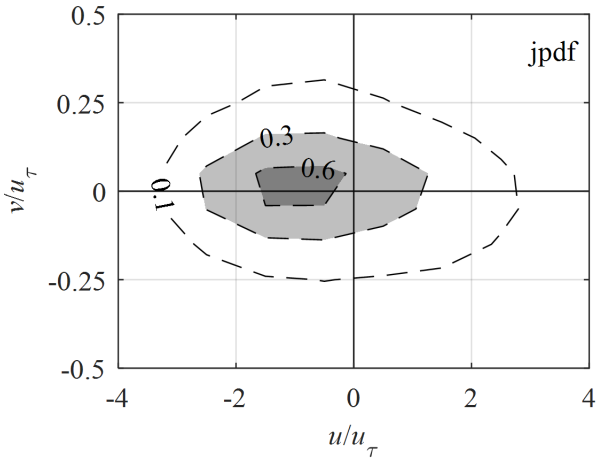

Figure 5.14: Joint probability density function of normalized velocity fluctuations. Only the particles with $y < 125\mu$m are considered.

$|\theta|$, is shown in Figures 5.15(a) and 5.15(b) for the streamwise and wall-normal components, respectively. Results are also conditionally averaged based on the $u - v$ quadrants of particle's motion. The conditional averaging is carried out for $|\theta| < 4°$ with a bin size of 0.5°. The $|\theta| < 4°$ range is applied to ensure statistical convergence as there are few particles outside this range. As expected, the particles with Q_1 and Q_4 motion ($u > 0$) have larger U^+ than the particles with Q_2 and Q_3 motion ($u < 0$) in Figure 5.15(a). The U^+ of the particles in the first quadrant (Q_1) is $\sim 6.3u_\tau$ and does not considerably change with $|\theta|$; streamwise velocity of the particles with Q_1 motion is not a function of the trajectory angle. For the particles with a sweep motion (Q_4), U^+ increases with increasing $|\theta|$ and reaches $\sim 7.5u_\tau$ at $|\theta| = 4°$. This is because the particles with larger $|\theta|$ have come down from a higher y^+, and therefore have higher U^+. The U^+ value of the particles in Q_2 and Q_3 are almost equal at different $|\theta|$, and for both quadrants, U^+ slightly decreases with increasing $|\theta|$. As seen in Figure 5.15 (b), there is a linear relation between $|\theta|$ and V^+, which indicates that $|\theta|$ is mainly caused by a variation of V and not U. The conditionally averaged values of V^+ also show that the particles with Q_1 and Q_4 motions ($u > 0$) have a larger magnitude of V^+ compared with the particles with Q_2 and Q_3 ($u < 0$). This means the faster particles (Q_1 and Q_4) have a larger wall-normal velocity, which diffuses their momentum in the wall-normal direction.

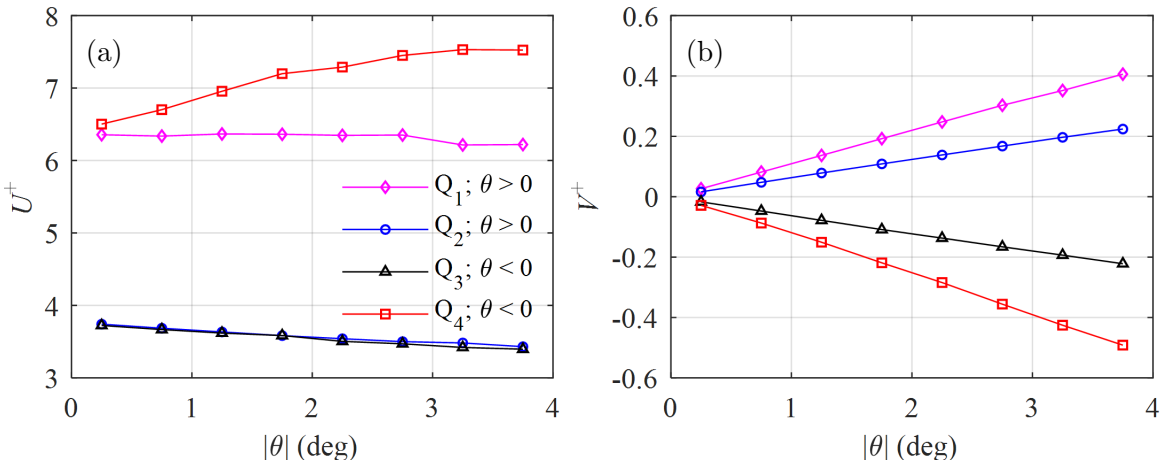

Figure 5.15: Conditionally averaged (a) U^+ and (b) V^+ of particles based on $u-v$ quadrants as functions of $|\theta|$. Only the particles with $y < 125\mu$m are considered in this analysis.

The variation of conditionally averaged A_x^+ with $|\theta|$ is shown in Figure 5.16(a) to compare the contributions of different quadrants. It is expected that the particles with upward motion (Q_1 and Q_2) accelerate in the streamwise direction as they move upward into the regions with higher U values. However, Figure 5.16(a) shows that such a trend is only valid for $|\theta| > 1$ when the motion away from the wall is large enough. When the particle's ascent angle is smaller than 1°, A_x^+ for Q_1 and Q_2 motions is negative. The particles in Q_3 have downward motion ($|\theta| < 0$) and $A_x^+ < 0$. In all these cases, streamwise deceleration is associated with viscous deceleration by the near-wall fluid and particle–wall collisions. Figure 5.16(a) shows that particles with sweeping motion in the Q_4 quadrant experience the highest streamwise deceleration. The deceleration of these particles also increases with increasing $|\theta|$. This larger deceleration of trajectories with large $|\theta|$ is associated with a larger viscous drag due to their greater velocity difference with respect to the surrounding fluid; the particles with larger $|\theta|$ have come down from higher y^+ locations with higher velocity.

The variation of conditionally averaged A_y^+ values is also investigated for the $u-v$ quadrants and is presented in Figure 5.16(b). All four quadrants have a positive A_y^+ . As it was explained previously, a positive A_y^+ indicates acceleration of upward-moving particles

and deceleration of downward moving particles. For the sweeping motion of Q_4, a strong increase in A_y^+ with increasing $|\theta|$ is observed. The larger positive A_y^+ of the sweeping particles is attributed to greater wall-normal drag and wall repulsive force as they approach the wall under a larger $|\theta|$. A strong increase in A_y^+ with increasing $|\theta|$, is also observed for the upward-moving particles ($v > 0$) in Q_1. Therefore, upward trajectories with a larger angle undergo a stronger wall-normal acceleration. A possible cause of this trend can be stronger ejection events which accelerate the particles upward under a larger ascent angle. The A_y^+ of particles with Q_2 motion slightly increases with increasing $|\theta|$, while the A_y^+ of particles in Q_3 does not show a strong and monotonic dependence on $|\theta|$. In general, particles with $u > 0$ (Q_1 and Q_4) have greater A_y^+ than the particles with $u < 0$ (Q_2 and Q_3). As was seen in Figure 5.15(b), the particles with $u > 0$ have a larger V^+, which can cause a larger velocity difference relative to the surrounding fluid. Therefore, a larger drag force can act on particles with $u > 0$, which increases their A_y^+ .

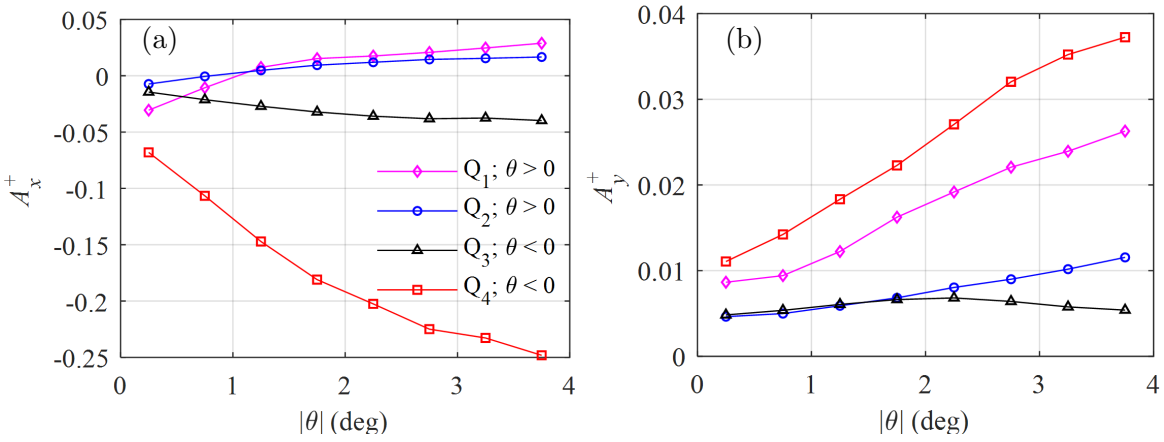

Figure 5.16: Conditionally averaged (a) A_x^+ and (b) A_y^+ of particles based on $u-v$ quadrants as functions of $|\theta|$. Only the particles with $y < 125\mu$m are considered in this analysis.

5.3.5.3 Collision with the wall

The momentum exchange of particles during particle–wall collision is investigated by analyzing particle trajectories that are in a narrower wall separation distance relative to the previous analysis. In this analysis, only particles that the distance of their centroid from

the wall is equal to, or smaller than 62.5μm are considered. This resulted in approximately 34,000 particle trajectories within 5 seconds of time-resolved 3D-LPT data. For these near-wall trajectories, wall-collision is defined when the particle also has a negligible wall-normal velocity. This criterion is imposed when the instantaneous wall-normal particle velocity, V, is an order of magnitude smaller than the average of the absolute wall-normal particle velocity, $\langle|V|\rangle$. Therefore, $|V| < 0.1\langle|V|\rangle$, where $\langle|V|\rangle = 0.01$m/s at $y^+ = 3.4$. The period when this criterion is valid is defined as the wall-interaction time, t_i. For the tracks with a detected collision and within $y \leq 62.5$μm, the absolute value of trajectory angle before the collision is averaged and indicated as $|\theta_i|$. The average trajectory angle after the collision is also estimated and denoted as the average rebound angle, $\langle\theta_r\rangle$.

The variation of the estimated $\langle\theta_r\rangle$ with $|\theta_i|$ is presented in Figure 5.17(a). For $|\theta_i| < 1.5°$, $\langle\theta_r\rangle$ is greater than $|\theta_i|$, meaning that trajectories with small θ rebound at a larger angle and disperse through collision with the wall. Particles with $|\theta_i| > 1.5°$ rebound at a smaller angle; $\langle\theta_r\rangle < |\theta_i|$. The normalized average of the wall-interaction time ($t_i^+ = \langle t_i\rangle/t_\tau$) is presented in Figure 5.17(b) as a function of $|\theta_i|$. Inspection of the data shows that a particle with $|\theta_i| < 1.5°$ can spend on average $5t_\tau$ in contact with the wall. Such particles may have multiple small collisions with the wall or slide along it. The wall-interaction time scale approaches a constant value of approximately 1.6 for particles with $|\theta_i| > 1.5°$.

The average restitution ratio of particles (the ratio of the rebound velocity to the incident velocity) in the streamwise direction, $\langle e_U\rangle$, and wall-normal, $\langle e_V\rangle$, are determined and presented in Figure 5.18 to show their variation with $|\theta_i|$. Figure 5.18(a) shows that for small incident angles of $|\theta_i| < 1°$, $\langle e_U\rangle$ is close to 1 which means that the sliding particles have negligible momentum exchange and undergo elastic collision in the streamwise direction. This is consistent with the smaller A_x^+ values observed for downward-moving particles (Q_3 and Q_4) at small $|\theta|$, as seen in Figure 5.16(a). As the incident angle becomes steeper ($|\theta_i| > 1°$), $\langle e_U\rangle$ reduces to ~ 0.925 for $|\theta_i| > 2°$. In other words, the streamwise momentum of these particles reduces by 7.5 % due to the collision with the wall.

The particles with $|\theta_i| < 1.5°$ have wall-normal restitution ratios, $\langle e_V\rangle$, greater than

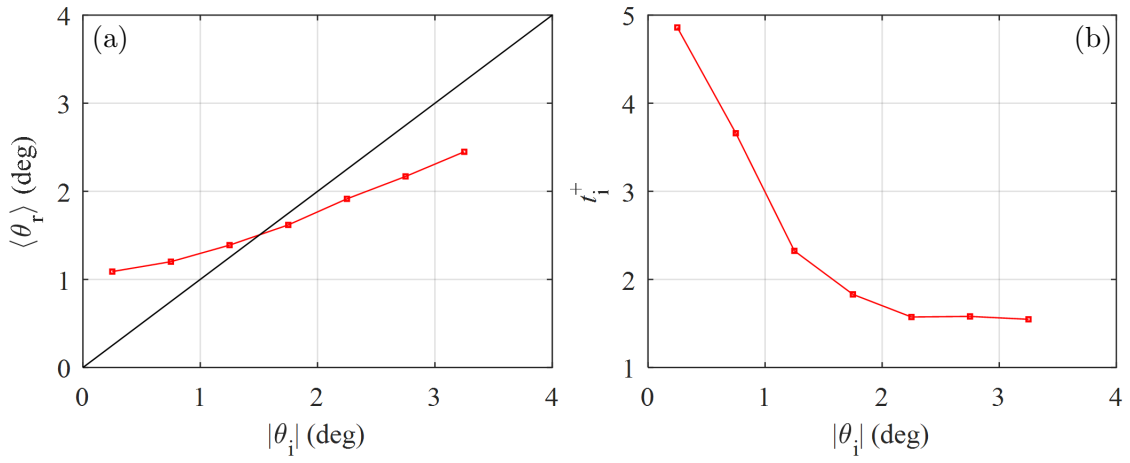

Figure 5.17: (a) The average rebound angle and (b) the wall-interaction time scale of particles as a function of incident angle.

1 as seen in Figure 5.18(b). These particles slide on the wall over a longer time as seen in Figure 5.17(b). The longer interaction increases the angular velocity of a particle since the bottom surface of the particle is subject to surface friction due to the interaction with the wall, while its upper surface is subjected only to shear. This angular velocity is known to produce the Magnus lift force (Rubinow and Keller, 1961). The Magnus force in the wall-normal direction can be determined as $F_{\text{mag}} = \pi d_p^3 \rho_f \omega (U_p - U_f)$ (Crowe et al., 2012). Here, ω is the angular velocity of a particle, which is approximated as half of the local shear rate (Drew and Passman, 2006). Based on the unladen mean velocity profile, the mean shear rate at $y^+ = 3.4$ is approximately 2800 per second. At this wall-normal location, $\langle U_p \rangle - \langle U_f \rangle$ is approximately 0.09 m/s. Therefore, the approximate F_{mag} for a particle at $y^+ = 3.4$ is approximately 12.2×10^{-8}N. This force is approximately four times more than the weight of a particle ($\sim 3.15 \times 10^{-8}$N) and can potentially lift a particle. This type of particle motion, where particle lift occurs after some period of sliding on the bottom wall was also recently observed by Barros et al. (2018). Based on these observations, the fact that $\langle e_V \rangle > 1$ does not mean that the particle gains wall-normal momentum through collision with the wall; the excess momentum is due to the additional angular momentum which in turn produces a lift force. By increasing $|\theta_i|$, $\langle e_V \rangle$ decreases to a value of approximately

0.8 for the particles with $|\theta_i| > 1.75°$. Generally, increasing the incident angle increases the wall-normal momentum loss and results in lower values of $\langle e_V \rangle$.

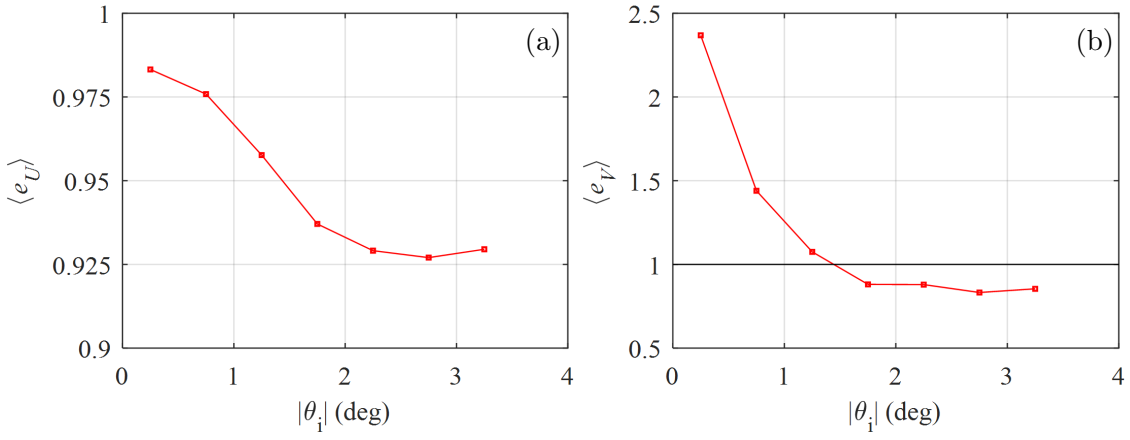

Figure 5.18: Variation of (a) streamwise and (b) wall-normal particle restitution ratios with absolute incident angle.

5.4 Summary and conclusion

The 3D-LPT measurement of G-125 particles acceleration at $Re_\tau = 410$ and $C_v = 0.03\%$ showed that there are qualitative relations between the wall-normal variations of $\langle A_x \rangle$ and $\partial\langle uv \rangle = \partial y$ as well as $\langle A_y \rangle$ and $\partial\langle v^2 \rangle = \partial y$. Comparison of the wall-normal acceleration of particles and unladen flow showed similarities between particle dynamics and the near-wall fluid dynamics. The investigations show the presence of two layers based on the acceleration of the particles: (i) an inner layer in the vicinity of the wall at approximately $y^+ < 20$, and (ii) an outer layer at a farther distance from the wall at $y^+ > 20$.

Within the inner-layer, the particles decelerated (on average) in the streamwise direction. The maximum negative streamwise deceleration was observed at $y^+ = 10$ and it gradually reduced to zero at $y^+ = 20$. In the inner-layer, a large percentage of the particles had velocities less than the average velocity and their turbulent motions belonged to the second and the third quadrants of velocity fluctuations. However, the particle dynamics in this layer were dominated by the extreme motions of a smaller number of particles in the fourth

quadrant. These particles had a sweeping motion toward the wall and demonstrated the largest streamwise momentum and deceleration. The wall-normal acceleration of particles in the inner layer was positive, which indicated an increase in wall-normal velocity when a particle moves away from the wall, or a reduction of wall-normal velocity when a particle moves towards the wall.

In the outer layer, particles had an overall positive streamwise acceleration, which peaked at approximately $y^+ = 30$. The peak was associated with the particles in the second quadrant, i.e. an ejection motion. The maximum transfer of momentum from the liquid phase to the particles occurred in the logarithmic layer, where the streamwise acceleration of the particles was large and positive. However, the streamwise acceleration gradually attenuated with increasing y^+. At a farther distance from the wall, the positive streamwise acceleration of the particles moving away from the wall was balanced by the negative streamwise acceleration of the particles moving towards the wall. The outer-layer particles also had a negative wall-normal acceleration, which was associated with an increase in the wall-normal velocity of particles in the third and fourth quadrant, and reduction in the wall-normal velocity of particles of the first and second quadrant.

The interaction of particles with the wall was studied by analyzing the trajectory angle, velocity, and acceleration of the particles found in the immediate vicinity of the wall. At $y_p < 125\mu$m, particles with sweeping motion had the maximum momentum, streamwise deceleration, and wall-normal acceleration compared with other particles. These terms increased by increasing the trajectory angle. At $y_p = 125\mu$m, the particle trajectory angle had a peaky distribution; a large number of particles had a near-zero angle while there were occasional extremely large trajectory angles of up to 20°. The latter was associated with the near-wall particles that had a small streamwise velocity. With increasing y^+, the trajectory angle did not demonstrate a peaky distribution, and the mode of the distribution was slightly negative as most of the particles gradually settled toward the wall. For particles within $y_p \leq 125\mu$m, wall collision was defined when a particle had a negligible wall-normal velocity. The particles with an incident angle of $|\theta_i| < 1.5°$ had a longer average interaction

time with the wall, which could be as long as $\sim 5t_\tau$. These particles were referred to as the sliding particles and had a negligible streamwise momentum exchange ($\sim 5\%$) during their interaction with the wall. It is conjectured that their longer interaction time increased the effect of the Magnus lift force on them. As a result, their average rebound angle was larger than their incident angle and their wall-normal restitution coefficient was larger than one. The particles with sharper collision angle with the wall of $\theta_i \geq 1.5^\circ$ had smaller streamwise and wall-normal restitution coefficients, and also a smaller average wall-interaction time. The autocorrelation coefficients of wall-normal velocity and trajectory angle had a local minimum with negative value at a time-shift of approximately $11t_\tau$. This indicates the average time for a change in the direction of wall-normal motions for the particles at $y_p \leq$ 125µm due to their interaction with the wall. A negative autocorrelation coefficient was not observed for the particles at a farther distance from the wall.

In general, this experimental investigation showed that the assumptions of elastic particle–wall collision and point-particles are inadequate for accurate modeling of large inertial particles in water. Measurements of particles' velocity demonstrated evidence of inelastic particle–wall collisions with considerable loss of momentum at larger impact angles. In addition, these measurements showed evidence of prolonged interactions with the wall for particles that impact the wall at a shallow angle. This resulted in an increase of particles' momentum, which cannot be accounted for using the steady-state drag of the point-particle model. Moreover, the discrepancy between the acceleration profiles from the experiments and those from the numerical simulation of Zamansky et al. (2011) showed that the point-particle assumption is not valid for large particles ($d_p^+ = 7.4$) with small density relative to the carrier phase ($r_\rho = 2.6$).

Chapter 6

The effect of Reynolds number and particle concentration on the near-wall motion of spherical particles in turbulent channel flow

6.1 Introduction

In this chapter, the analyzes of the previous study presented in Chapter 5 are extended to a higher Re_τ of 765 and a higher C_v of 0.15% to investigate the effect of these parameters on the near-wall motion of the particles in particle-laden turbulent flows. Experiments were conducted using the flow facility described in Section 3.1, measurements were performed using the 3D-LPT system and the data processing was carried out using STB algorithm in DaVis 8.4 (LaVision GmbH), as described in Section 4.3. The effect of Re_τ and C_v on the kinematics and distribution of particles is investigated in Section 6.3.1 by studying their velocity statistics, turbulent kinetic energy spectrum, and number density distribution. The dynamics of particles is scrutinized in Section 6.3.2 through the investigation of their acceleration statistics. The influence of Re_τ and C_v on the Lagrangian time scales of particles in different directions is studied in Section 6.3.3 by estimating the Lagrangian autocorrelation function (LAF) of particles velocity and acceleration. The PPI rate and V_r are estimated in Section 6.3.4 to analyze the effect of Re_τ and C_v on them. The influence of Re_τ and C_v on PWI are investigated in Section 6.3.5 by studying the impact angle and

velocity components of particles that collided with the wall and their wall-normal restitution ratio. The summary and conclusions of the analysis of this chapter are provided in Section 6.4.

6.2 Experimental design

The experiments of unladen water flow were performed at a constant temperature of 20° with mass flow rates of 1.76 and 3.52 kg/s, resulted in the U_b of 0.98 and 1.96 m/s and the Re_H of 14,600 and 29,200, respectively. Table 6.1 presents the characteristics of the unladen turbulent flows including their Re_H, Re_τ , U_b, and the inner scaling.

Re_τ	Re_H	U_b (m/s)	u_τ (m/s)	λ (μm)	t_τ(μs)
410	14,600	0.98	0.055	18	337
765	29,200	1.96	0.102	10	96

Table 6.1: Characteristics of the unladen turbulent flows tested in the present study. The inner scaling was determined based on the velocity profiles measured using 3D-LPT.

The particle-laden experiments were performed at similar mass flow rates as the unladen experiments using G-125 particles dispersed in water at the volume concentrations of 0.03% and 0.15%. The maximum $\langle U_s \rangle$ estimated as $|\langle U_f \rangle - \langle U_p \rangle|$ was approximately 0.32 m/s for particles at $Re_\tau = 765$ and $C_v = 0.15\%$, discussed in Section 6.3.1, resulting in $Re_{ps} \approx 43$. The estimated Re_{ps} is significantly less than the threshold of $Re_{ps} = 110$ suggested by Hetsroni (1989) for vortex shedding for spherical particles.

Figure 6.1 shows the wall-normal variation of St_e determined for the particles at the lower and higher Re_τ based on Equation 2.16. To compare the St_e at similar wall-normal locations, y is normalized by the inner length-scale of the unladen flow at the lower Re_τ, λ_0, and presented as y^*. At the lower Re_τ, the St_e varies from 3.3 at $y^* = 3.4$ to 0.05 at $y^* = 215$. As it is expected, the St_e is larger for the higher Re_τ and varies from 6.0 to 0.1 with increasing y^*. The Stokes number based on the inner time-scale of the unladen

counterpart, St^+, was 4.5 and 15.8 for the low and high Re_τ cases, respectively. Table 6.2 shows the characteristics of the performed experiments including the number of the collected images, N_{im}, and the approximate number of the detected trajectories by STB algorithm, N_{tr}. The acronyms that are used to present results in the following sections are also introduced in this table. The first letter of the acronyms refers to low Re_τ (L) or high Re_τ (H) and the second letter refers to unladen (U), low C_v (L), or high C_v (H).

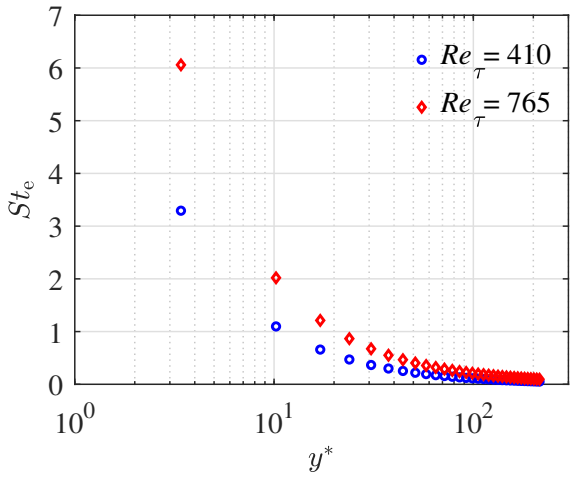

Figure 6.1: The wall-normal variation of St_e at the lower and higher Re_τ cases. The St_e was determined based on d_{50} of G-125 particles.

Experiment	Re_τ	$C_v(\%)$	St^+	$N_{im} \times 10^{-3}$	$N_{tr} \times 10^{-6}$	Acronym
Unladen	410	-	-	27	9.0	LU
Particle-laden	410	0.03	4.5	50	2.3	LL
Particle-laden	410	0.15	4.5	50	3.5	LH
Unladen	765	-	-	27	9.2	HU
Particle-laden	765	0.03	15.8	50	2.1	HL
Particle-laden	765	0.15	15.8	50	3.4	HH

Table 6.2: The specifications of the experiments performed in the present study. The St^+ was determined based on the d_{50} of G-125 particles.

Similar to the previous chapter, the velocity and acceleration fields were averaged in the streamwise and spanwise directions and in time. The wall-normal size of the averaging bins was equal to λ for the unladen flows and 125µm for the particle-laden flows. In this

chapter, the wall-normal distance, velocity and acceleration are either normalized by the inner scaling of the unladen flow at the lower Re_τ , denoted by the superscript '*', or the inner scaling of the corresponding unladen counterpart, represented by the superscript '+'. The random error of the velocity and acceleration statistics of unladen flow and particles were investigated based on the standard deviation of the last 20% of data collected at $y/H = 0.008$ (equivalent to $y^* = 3.4$) and presented in Table 4.5.

6.3 Results and discussion

6.3.1 Particle kinematics and distribution

The variation of $U^+ = \langle U \rangle / u_\tau$ with y^+ for LU and HU are presented in a semi-logarithmic plot in Figure 6.2(a) and compared with DNS results of Moser et al. (1999) at $Re_\tau = 395$. The linear viscous sublayer profile ($U^+ = y^+$) and the logarithmic law of the wall with $\kappa = 0.4$ and $B = 5.2$ are also presented in this figure. The unladen measurements agree well with the DNS results across the presented data. For the low Re_τ case, the first data point is at $y^+ = 3.4$ and extends up to $y^+ = 218$. For the high Re_τ flow, the first data point is at $y^+ = 6.2$ and spans up to $y^+ = 400$. This comparison shows the accuracy of the mean flow from 3D-PTV measurements and also the fully developed state of the turbulent channel flows.

The normalized mean streamwise velocity of particles is presented in Figure 6.2(b) along with their unladen counterparts. To compare the effect of Re_τ and C_v on the streamwise velocity of particles at similar wall-normal locations, $\langle U \rangle$ and y are normalized by the inner scaling of LU (i.e. $u_{\tau 0}$ and λ_0) and presented as U^* and y^*, respectively. At $y^* = 3.4$, the U^* of particles is higher than their unladen counterpart. This is expected since the no-slip boundary condition does not apply to the particles, as it was also reported by Taniere et al. (1997), Righetti and Romano (2004), and Li et al. (2012). At the same location, the normalized velocity difference between particles and their unladen counterpart, U_s^*, is greater for LH and HH than LL and HL. This trend has been previously reported in the literature (Kulick et al., 1994; Li et al., 2016; Shokri et al., 2017) and it is related to the

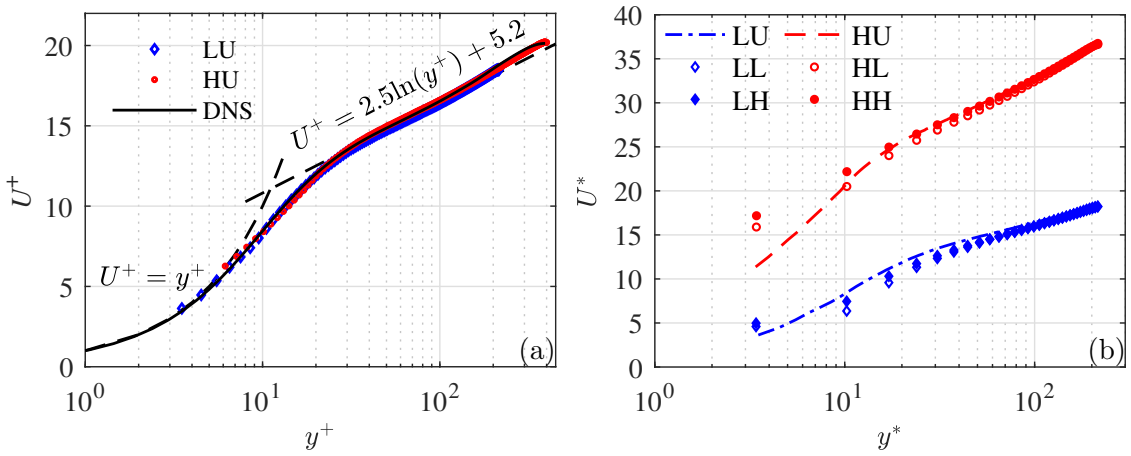

Figure 6.2: The wall-normal variation of normalized average streamwise velocity of (a) unladen flow and (b) particles in laden flows. Acronyms are defined in Table 6.2. The DNS result is from Moser et al. (1999) at $Re_\tau = 395$.

higher C_v of LH and HH which increases the wall-normal momentum transfer of particles from the center of the channel toward the wall, resulting in a higher particles velocity close to the wall. For both HL and HH, U_s^* at $y^* = 3.4$ is larger than LL and LH. In addition, the difference between U_s^* of HH and HL is about three times more than that of LH and LL. The greater St_e of particles at the higher Re_τ increases particles capability to maintain their streamwise momentum when they move toward the wall (Zhao et al., 2012; Shokri et al., 2017). Away from the wall, U^* of particles is less than unladen counterparts due to their higher inertia.

To investigate the effect of Re_τ and C_v on the kinematics of particles in the wall-normal and spanwise directions, the pdf of V/U and W/U for particles at $y^* = 3.4$, 106, and 215 are provided in Figure 6.3. The V/U and W/U ratios have wider distribution at $y^* = 3.4$. At this location, particles have small U and they are under the effect of near-wall coherent vortical structures of the flow that distributes them in the wall-normal and spanwise directions. Due to the opposing effects of gravity and near-wall lift forces on particles wall-normal motion, the V/U ratio has a narrower distribution than W/U at $y^* = 3.4$. By increasing y^* the U of particles increases and the strength and frequency of vortical structures reduce, resulting in a narrower pdf for both V/U and W/U ratios at

$y^* = 106$ and 215.

Turbulent motions are responsible for wall-normal and spanwise distribution of particles in a turbulent flow. The drag force that eddies apply on the particles is proportional to their characteristic velocity, u_e. Close to the wall $u_e \sim u$ (Tennekes and Lumley, 1972). Increasing Re_τ increases the u of the flow and the drag force that eddies apply on the particles. However, since $U > u$, the increment of streamwise drag force, that is proportional to U, is larger than the increment of wall-normal and spanwise drag forces applied on the particles by the eddies. This results in narrower pdfs of V/U and W/U at $y^* = 3.4$ for the higher Re_τ. Far away from the wall, the $u_e \sim U$ (Tennekes and Lumley, 1972). Therefore, with increasing Re_τ, the streamwise, wall-normal, and spanwise drag forces that are applied to the particles increase with the same ratio, resulting in almost the same pdfs of V/U and W/U at $y^* = 106$ and 215 for lower and higher Re_τ.

The effect of Re_τ on the pdfs of V/U and W/U can also be explained based on St_e. With increasing Re_τ, the St_e of particles significantly increases at $y^* = 3.4$ (see Figure 6.1). This means that the t_e of the energy-containing eddies becomes much smaller than the time that particles need to follow them, t_p, which narrows the pdfs of V/U and W/U at $y^* = 3.4$. With increasing y^*, the difference between St_e of particles at the higher and lower Re_τ reduces and it lessens the effect of Re_τ on the pdfs of V/U and W/U at $y^* = 106$ and 215. At the higher C_v the wall-normal momentum of particles is larger for both lower and higher Re_τ, resulting in a wider pdf of V/U, specifically at $y^* = 3.4$. The effect of C_v on the pdf of V/U is smaller farther away from the wall, where the motion of particles is dominated by the large drag forces that are proportional to U. The pdfs of W/U show that increasing C_v does not affect the ratio of spanwise momentum to the streamwise momentum of particles.

The particles trajectory angle in $x-y$ and $x-z$ planes can be defined as $\theta = \arctan(V/U)$ and $\alpha = \arctan(W/U)$. Therefore, Figure 6.3 indicates that Re_τ or C_v does not considerably affect the θ and α away from the wall. Close to the wall, however, the ranges of θ become smaller by increasing Re_τ and larger by increasing C_v. The range of α also decreases by increasing Re_τ, but changing C_v does not affect it.

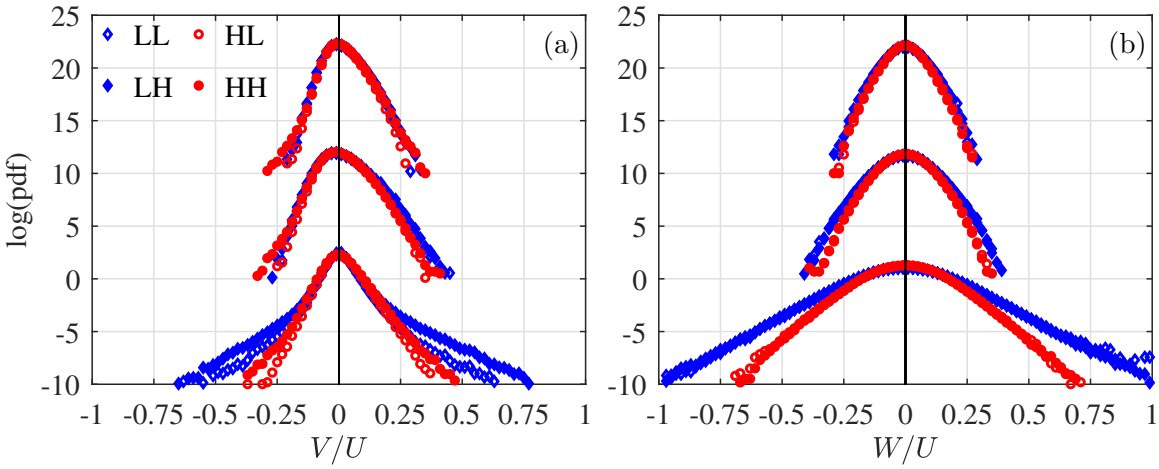

Figure 6.3: The pdf of (a) V/U and (b) W/U of particles at $y^* = 3.4, 106$, and 215 from bottom to top, respectively. For clarity, the pdfs at $y^* = 106$ and 215 are shifted up by 10 and 20 units of the vertical axis, respectively. The log(pdf) less than -10 is not shown. Acronyms are defined in Table 6.2.

The influence of Re_τ and C_v on the local concentration of particles is investigated in Figure 6.4, showing the wall-normal variation of particles number density, $\bar{N}$, calculated as the number of particles in each bin divided by the average number of particles in all the bins. Increasing Re_τ decreases the number density close to the wall and increases it away from the wall as it was also reported by Ahmadi et al. (2019). At the low Re_τ, the maximum local concentration is close to the wall for both LL and LH due to the effect of gravity and the weak turbulence suspension. At the higher Re_τ, however, the ejection and sweep motions become stronger and disperse the particles; the location of the maximum local concentration of particles is farther away from the wall, as it is seen for HL and HH.

The Rouse number, calculated using Equation 2.14, for particles is 0.61 and 0.33 at the low and high Re_τ cases, respectively, showing the larger turbulence contribution in suspension of the particles at the higher Re_τ. By increasing C_v the particle number density is decreased close to the wall and increased away from the wall. This behaviour was reported by Varaksin et al. (2000). The higher C_v makes a more uniform particle distribution for both LH and HH cases compared with LL and HL cases, respectively.

The $\langle u^2 \rangle$, $\langle v^2 \rangle$, $\langle w^2 \rangle$, and $\langle uv \rangle$ of unladen flows and particles in laden flows are normalized

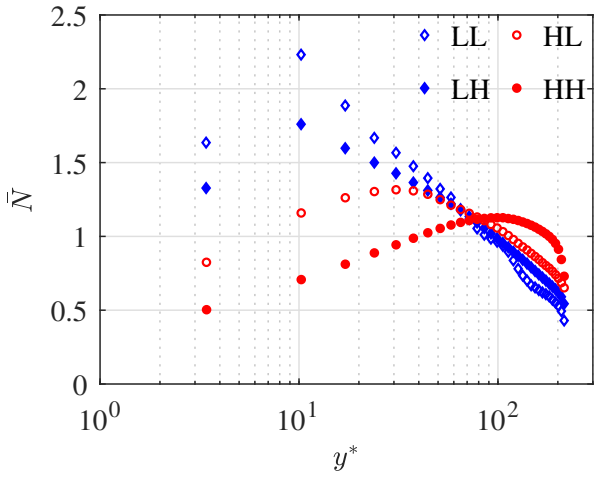

Figure 6.4: The number density distribution of particles in particle-laden flows. Acronyms are defined in Table 6.2.

using $u_{\tau 0}^2$ and presented as u^*, v^*, w^*, and $(uv)^*$ in Figure 6.5. The deviation of the Reynolds stresses of LU at their peak located at $y^* = 15$, 70, 40, and 35 from the DNS results of Moser et al. (1999) is about 4, 1, 2, and 2% for u^*, v^*, w^*, and $(uv)^*$, respectively. The good agreement of these variables shows the fully developed state of the flow and the measurement accuracy for Reynolds stresses.

As expected, with increasing Re_τ, the magnitude of Reynolds stresses increases for both unladen flows and particles. At the lower Re_τ, u^* of particles is slightly larger than the unladen flow in the whole measurement domain. The larger inertia of particles than the fluid results in a wider wall-normal diffusion of particles velocity and a larger u^* relative to the unladen flow. The particle larger inertia can also work in an opposite way and reduce the momentum transfer between particles and fluid, resulting in a lower u^* of particles than the unladen flow (Ahmadi et al., 2019). This behavior is observed at the higher Re_τ for particles close to the wall where their high local St_e reduces their response to the fluid. Increasing Re_τ increases the difference between the peak of v^*, w^*, and $(uv)^*$ of particles and their unladen counterparts, consistent with the results presented by Ahmadi et al. (2019) for 285 µm glass particles in a solid-liquid turbulent channel flow. The numerical investigation of Zhao et al. (2015) also showed that increasing particle St increases the difference between

the v^* and w^* peak of particles and their unladen counterparts. The trends of u^*, v^*, and $(uv)^*$ of particles with respect to the unladen flow at the higher Re_τ are consistent with the results presented by Righetti and Romano (2004) for 100 μm glass particles ($d^+ = 3.8$) in a water channel at Re_τ=790. With increasing y^* and reduction of St_e, the difference between the Reynolds stresses of particles and their unladen counterparts reduces.

Increasing C_v does not significantly affect particles Reynolds stresses at the lower Re_τ, but it modifies them at the higher Re_τ. This shows that the contribution of C_v to particle Reynolds stresses depends on St_e. The u^* of HH is smaller than HL at $10 \leq y^* \leq 40$. The reduction of streamwise velocity fluctuation by increasing C_v was previously reported by Nouri et al. (1987) for 270 μm inertial particles in vertical solid-liquid pipe flow. Yamamoto et al. (2001) argued that PPI reduces the fluctuation energy of particles in the streamwise direction and increases it in the direction normal to the mean flow. The higher v^* and w^* (near the wall) of HH than HL shows this behavior. Fong et al. (2019) also observed the increase of wall-normal velocity fluctuation of particles by increasing C_v in a solid-air vertical channel flow. The magnitude of $(uv)^*$ of HH is larger than HL at $y^* \leq 10$ due to the increase of wall-normal motion of particles at higher C_v which exposes more particles to the high shear region of the flow close to the wall.

The effect of Re_τ and C_v on the distribution of turbulent kinetic energy in the frequency domain is investigated in Figure 6.6. In this figure, the pre-multiplied LSD of normalized turbulent kinetic energy in x, y and z directions is presented as a function of $\bar{f}$, which is the frequency normalized by the Nyquist frequency. As expected, increasing Re_τ increases the energy in three directions over all the frequencies within the temporal range of the 3D-PTV measurement system. Increasing C_v, reduces the kinetic energy from the streamwise (and slightly spanwise) direction and increases it in the wall-normal direction. The reduction of energy from the streamwise and spanwise directions is more significant at the lower frequencies and the increment of wall-normal kinetic energy is larger at the higher frequencies. This trend is more significant at the higher Re_τ. The effect of C_v on the LSD of turbulent kinetic energy in the spanwise direction is smaller than streamwise and wall-normal directions.

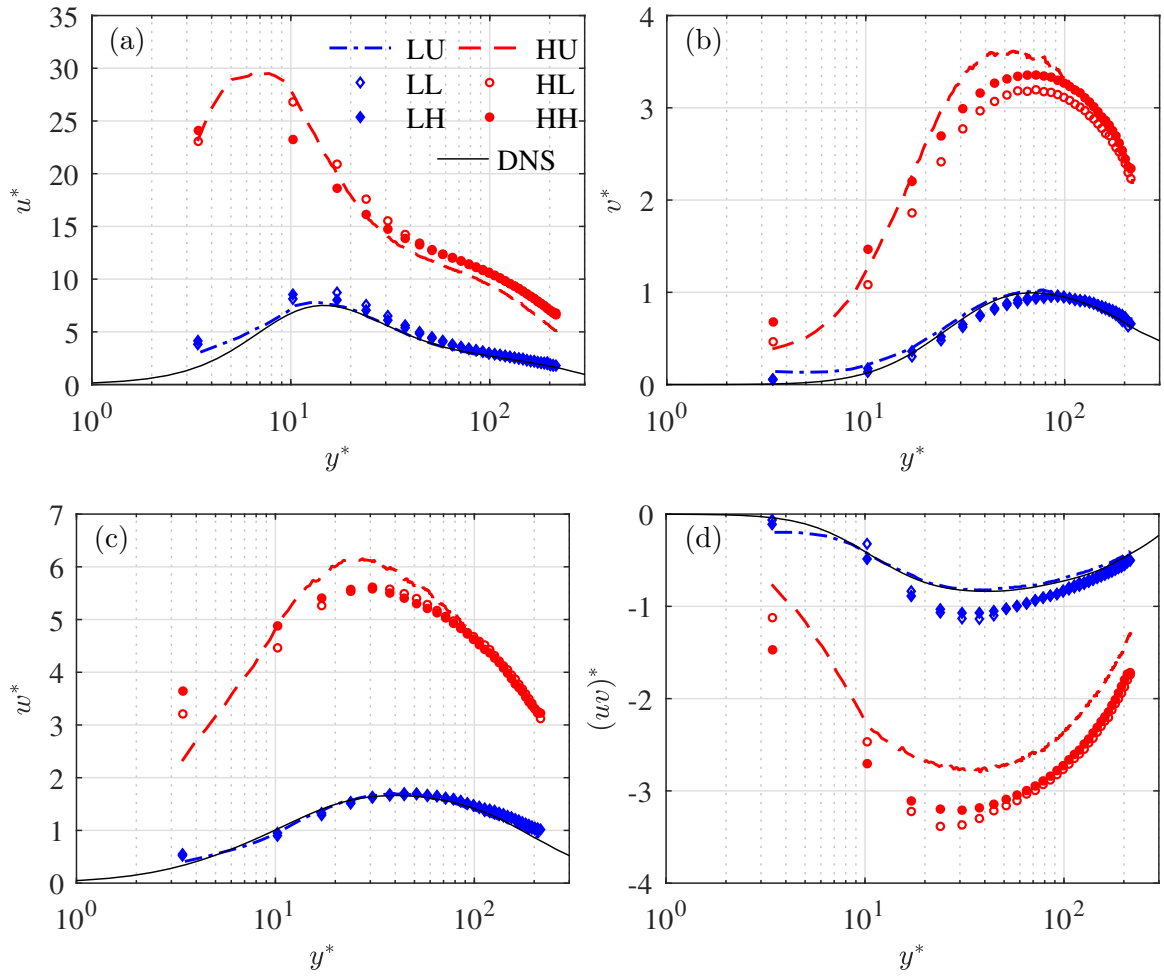

Figure 6.5: The wall-normal variation of normalized Reynolds stresses for unladen flow and particles. Acronyms are defined in Table 6.2. The solid lines show the DNS results of Moser et al. (1999) for unladen channel flow at $Re_\tau = 395$.

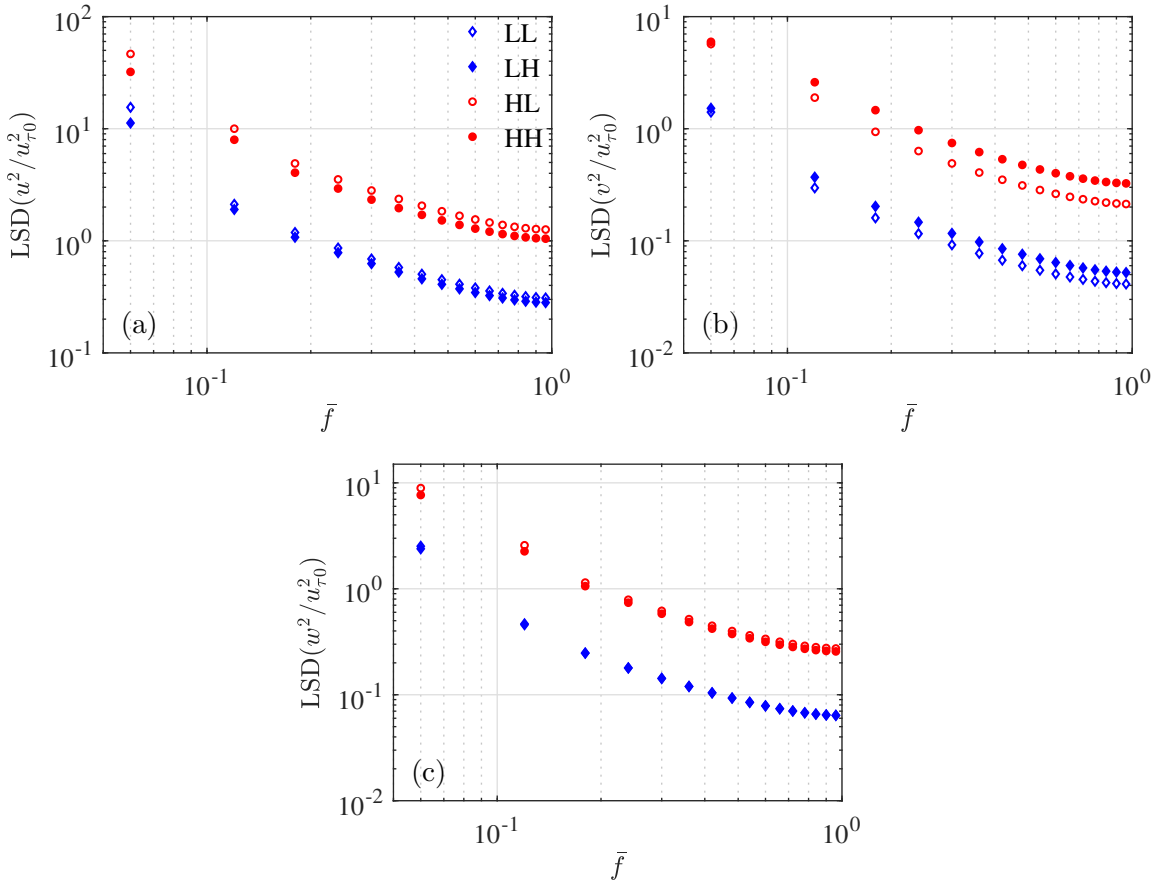

Figure 6.6: Pre-multiplied LSD of (a) $u^2/u_{\tau 0}^2$, (b) $v^2/u_{\tau 0}^2$, and (c) $w^2/u_{\tau 0}^2$ of particles. Acronyms are defined in Table 6.2.

6.3.2 Particle dynamics

The effect of Re_τ and C_v on the acceleration statistics of particles is investigated in this section. The mean and rms of acceleration components are normalized using $u_{\tau 0}$ and ν and presented as $A_x^* = \langle A_x \rangle \nu / u_{\tau 0}^3$, A_y^*, $a_x^* = \langle A_x^2 \rangle^{0.5} \nu / u_{\tau 0}^3$, a_y^*, a_z^*. The wall-normal variation of A_x^* and A_y^* are presented in Figure 6.7 for unladen flow and particles. The normalized mean spanwise acceleration, A_z^*, is zero for all the flows and not shown here. Both A_x^* and A_y^* of unladen flow at $Re_\tau = 410$ agree with the DNS results of Yeo et al. (2010) for unladen channel flow at $Re_\tau = 408$. The deviation from the DNS at A_x^* and A_y^* peak located at $y^* = 8$ and 16 is about 4% and 2%, respectively.

Due to the effect of viscous forces, particles have negative A_x^* (i.e. decelerate) very close

to the wall at $y^* < 20$, similar to their unladen counterparts. The streamwise deceleration of inertial particles near the wall was also reported by Gerashchenko et al. (2008), Lavezzo et al. (2010), and Zamansky et al. (2011). The larger viscous forces at higher Re_τ increases the streamwise deceleration of the unladen flow and particles near the wall. This behavior is consistent with the DNS of Yeo et al. (2010) for an unladen flow and experimental results of Gerashchenko et al. (2008) for inertial droplets in a liquid-air turbulent flow. Ebrahimian et al. (2019) showed that particles A_x^* in the inner-layer, $y^+ < 20$, is dominated by sweeping particles (i.e. particles with $u > 0$ and $v < 0$) which have the largest deceleration among all the particles. The A_x^* of particles is positive at $20 < y^* < 70$ but it gradually attenuates and becomes zero by increasing y^*. The particles' positive A_x^* is mainly associated with the effect of the drag force applied to the particles with ejection motions (i.e. particles with $u < 0$ and $v > 0$) as shown by Ebrahimian et al. (2019). Due to the larger drag force imposed on the particles and the stronger ejection motions at the higher Re_τ, the positive A_x^* of HL is larger than LL.

With increasing C_v, the more streamwise kinetic energy of particles is converted to wall-normal/spanwise kinetic energy (Yamamoto et al., 2001) and also dissipates due to the more frequent inelastic particles-particle collision, resulting in the reduction of their A_x^*. In addition, due to higher wall-normal fluctuation of particles, more particles with high velocity move toward the wall. Although these particles increase U^* of the solid phase in this region, see Figure 6.2(b), their interaction with the high-shear region of the flow and their inelastic collision with the wall increase their streamwise deceleration in the inner-layer. The increase of C_v also reduces the A_x^* of particles at $20 < y^* < 70$. This region overlaps with the log-layer as it is equivalent to $20 < y^+ < 70$ and $36 < y^+ < 126$ for the low and high Re_τ cases, respectively. At the higher C_v, the more frequent inelastic particle-particle collision, the larger streamwise to wall-normal momentum conversion, and the more interaction between low-velocity and high-velocity particles reduce the effect of streamwise drag force on A_x^* of particles.

The A_y^* of particles is positive at $y^* < 40$ due to the drag force applied by ejection

motions, Magnus force, the wall-normal pressure gradient across the quasi-streamwise vortices, wall repulsive force, and PPI. Ejection motions are known as a major mechanism for particle suspension in turbulent flows (Lelouvetel et al., 2009; Soldati and Marchioli, 2009). Particles that accompany ejection motions are pushed away from the wall by the drag force and have a positive A_y^*. Particles also experience Magnus lift force toward the center of the channel, when their velocity is larger than the surrounding fluid, due to their large rotation rate in the near-wall high-shear region (Rubinow and Keller, 1961; Drew and Passman, 2006; Crowe et al., 2012). The wall-normal pressure gradient caused by the quasi-streamwise vortices which is known as an effective factor for positive A_y^* of unladen flow in the inner-layer (Yeo et al., 2010) can also push the particles away from the wall and cause positive particle A_y^* (Ebrahimian et al., 2019). Another factor that can provide positive A_y^* for downward-moving particles is the wall repulsive force due to the pressure increase of the fluid layer between those particles and the wall (Feng et al., 1994). The collision of a downward moving particle with another particle also applies an upward force to the former particle (has a positive contribution on its A_y^*) and push the latter toward the wall which can increase the effect of wall repulsive force on it and have a positive contribution on its A_y^*.

With increasing Re_τ the ejection motions become stronger and apply a larger drag force on the particles which increases their A_y^*. The wall-normal pressure gradient of quasi-streamwise vortices and the Magnus lift force are also larger at the higher Re_τ and increase the A_y^*. At the higher C_v, the larger streamwise to wall-normal kinetic energy conversion increases the A_y^* of particles. Away from the wall at $y^* > 40$, the effect of ejection motions, wall-normal pressure gradient, upward Magnus force, and wall repulsive force on A_y^* of particles diminishes and the particles experience a negative A_y^* due to the gravity.

Investigation of A_x^* and A_y^* shows that the effect of C_v on particles acceleration depends on St_e. For example, increasing C_v from 0.03% to 0.15% reduces A_x^* of particles at $y^* = 24$ by 48% at the lower Re_τ and by 94% at the higher Re_τ. At the same location, increasing C_v increases A_y^* of particles by 3% at the lower Re_τ and by 48% at the higher Re_τ.

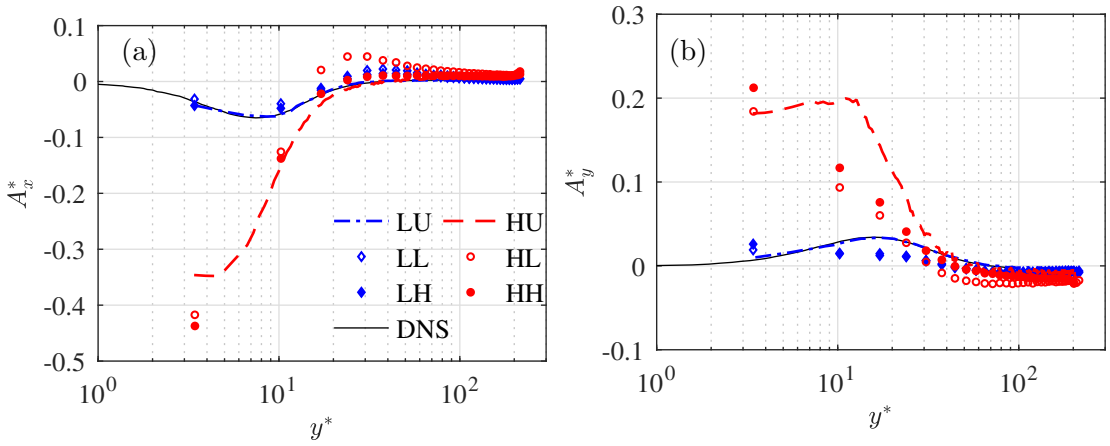

Figure 6.7: The wall-normal variation of (a) A_x^* and (b) A_y^* for unladen flow and particles. Acronyms are defined in Table 6.2. The solid lines show the DNS results of Yeo et al. (2010) for unladen channel flow at $Re_\tau = 408$.

The numerical simulation of particles with $d^+ > 1$ and $r_\rho \gg 1$ in vertical gas-solid turbulent channel flow by Li et al. (2016) showed that the wall-normal direction of motion of particles considerably affects their acceleration. The effect of wall-normal direction of motion of particles on their acceleration in the current study is investigated in Figure 6.8, showing the conditionally sampled A_x^* and A_y^* of particles with upward (i.e. $V > 0$) and downward (i.e. $V < 0$) motions. This figure confirms the significant effect of wall-normal direction of motion of particles on their A_x^*. The upward-moving particles are transported to high-velocity regions and subjected to drag force in the streamwise direction which results in their positive A_x^*. The downward moving particles are transported from high-velocity regions to low-velocity regions and subjected to large viscous forces near the wall, resulting in their significant streamwise deceleration (i.e. $A_x^* < 0$).

With increasing Re_τ, ejection motions become more frequent and stronger (Gad-el Hak and Bandyopadhyay, 1994), suspending more particles further away from the wall, and subject them to the larger drag force than the lower Re_τ. At the lower Re_τ, increasing C_v increases the A_x^* of upward moving particles at $y^* < 20$. In this region particles have the maximum local concentration, see Figure 6.4, and PPI increases their wall-normal displacement and expose them to a larger streamwise drag force in the high-shear region of the flow.

At the higher Re_τ, the region where PPI increases the A_x^* of upward-moving particles is smaller due to the smaller particles' local concentration and the thinner high-shear region. Beyond this region, however, increasing the inelastic PPI reduces the effect of streamwise drag force on the particles and lowers their A_x^*. The downward moving particles experience larger deceleration at the higher Re_τ due to the larger viscous forces. The deceleration of particles slightly increases at the higher C_v due to the more frequent inelastic PPI. The comparison of Figure 6.9(a) and (b) shows that the effect of PPI on the A_x^* of upward-moving particles is larger than downward-moving particles.

The effect of particles wall-normal direction of motion on their A_y^* is significantly smaller than A_x^*. The upward and downward moving particles are both under the effect of Magnus lift force and the wall-normal pressure gradient of quasi-streamwise vortices and have $A_y^* > 0$ at $y^* < 25$. The A_y^* of upward mowing particles is larger than downward mowing particles due to the effect of drag force applied on them by ejection motions. The stronger ejection motions and larger Magnus force at the higher Re_τ, results in the larger A_y^*. The A_y^* of upward and downward moving particles is larger at the higher C_v, showing that increasing C_v pushes these particles away from the wall. This is consistent with the particle number density distribution shown in Figure 6.4. With increasing y^* the A_y^* of both upward and downward moving particles decreases since the near-wall lift forces and ejection motions become weaker compared to the gravity.

The effect of Re_τ and C_v on the acceleration fluctuation of particles is investigated in Figure 6.9, showing the rms of particles acceleration. The rms of the three acceleration components of all the experiments peaks close to the wall at $y^* < 30$ due to the effect of near-wall turbulent vortical structures. Beyond this region, increasing y^* reduces a_x^*, a_y^* and a_z^*. The rms of all the acceleration components are larger at the higher Re_τ due to the larger pressure gradient and viscous forces as well as the stronger and more frequent vortical structures in the vicinity of the wall.

At the lower Re_τ, increasing C_v increases a_x^* at $y^* < 30$. This is due to the increase of the local concentration of particles, see Figure 6.4, PPI and wall-normal motion of particles

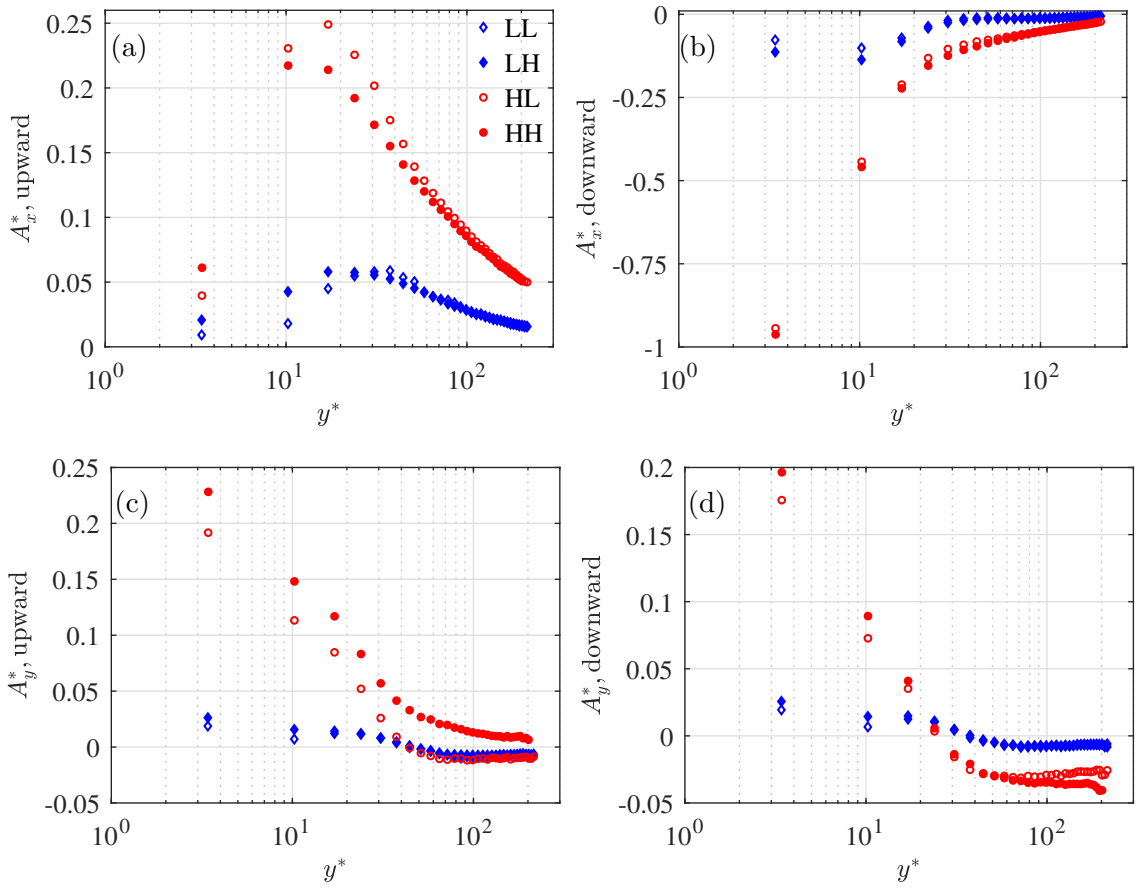

Figure 6.8: The wall-normal variation of A_x^* and A_y^* for (a, c) upward and (b, d) downward moving particles. Acronyms are defined in Table 6.2.

in this region which expose them more to the large velocity gradient in this region. For example, the a_x^* of LH at $y^* = 10$ is 30% larger than LL. Away from the wall, however, increasing C_v does not have a significant effect on a_x^*. At the higher Re_τ the high local concentration of particles is farther away from the wall, see Figure 6.4, resulting in a larger effect of C_v on a_x^* in that region. For instance, the a_x^* of HH is approximately 30% larger than HL at $y^* = 215$. The a_x^* of HH is also larger than HL at $y^* = 3.4$. This can be related to the increment of PWI due to the larger wall-normal motion of particles at the higher C_v.

The a_y^* shows a stronger dependency on C_v than a_x^*. The increment of wall-normal fluctuation of particles at the higher C_v, see Figure 6.5(b), increases the intermittency of the drag force applied to them and results in a larger a_y^*. For the particles at the lower

Re_τ this effect is larger close to the wall where the local concentration of particles is high and their motion is under the effect of near-wall turbulent structures. At the higher Re_τ, the stronger vortical structures near-wall and the high local concentration of particles away from the wall increase the a_y^* of particles in these two regions, resulting in a larger a_y^* of HH than HL at $y^* < 215$. Although at the lower Re_τ, the effect of increasing C_v on a_z^* is negligible, at the higher Re_τ it reduces the a_z^* at $y^* < 60$ and slightly increases it at $y^* > 100$.

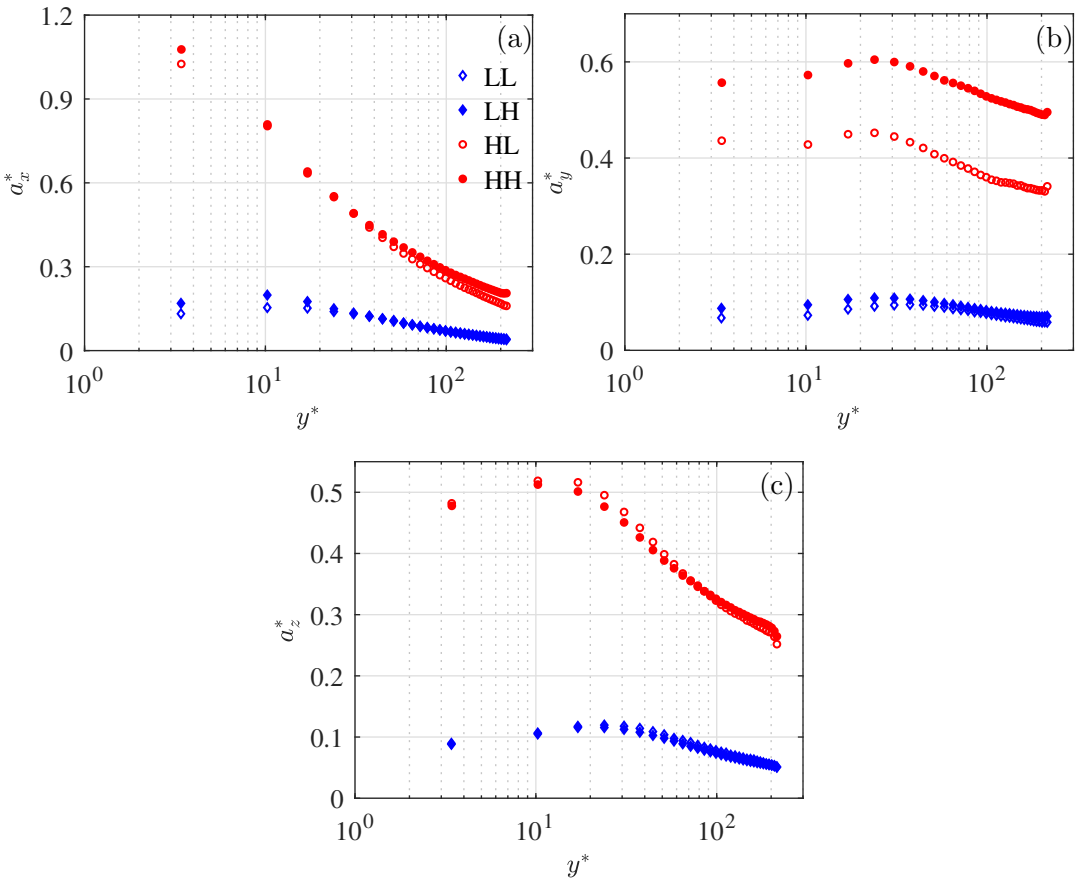

Figure 6.9: The wall-normal variation of (a) a_x^*, (b) a_y^*, and (c) a_z^* of particles. Acronyms are defined in Table 6.2.

Figure 6.10 indicates the pdf of A_i/a_i, where $i = x, y, z$ and $a_i = \langle A_i^2 \rangle^{0.5}$, for particles at $y^* = 3.4$, 105, and 215. Away from the wall at $y^* = 105$ and 215, the pdfs of A_i/a_i of all four particle-laden flows collapse onto one curve for each acceleration component. The

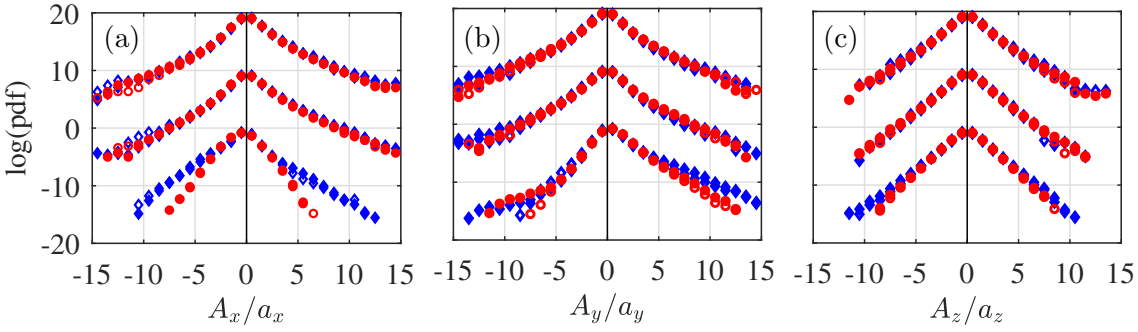

Figure 6.10: The pdf of (a) A_x/a_x, (b) A_y/a_y, and (c) A_z/a_z for particles at $y^* = 3.4$, 105, and 215, ordered from bottom to top, respectively. For clarity, the pdfs at $y^* = 105$ and 215 are shifted up by 10 and 20 units of the vertical axis, respectively. The log(pdf) values less than -15 are not shown. Symbols are similar to those defined in Figure 6.9(a).

independency of the pdf of A_x/a_x from Re_τ was expected. Previous studies indicated that the pdf of A_x/a_x away from the wall does not depend on d_η or r_ρ (Qureshi et al., 2007, 2008). Figure 6.10 shows that away from the wall, the pdf of A_i/a_i for all the components neither significantly depends on Re_τ nor C_v. In the non-isotropic turbulence at $y^* = 3.4$, however, increasing Re_τ narrows the tails of the pdfs and reduces their value. This behavior is more pronounced for the streamwise component. At the same location, the change in C_v does not have a significant effect on the pdfs of A_x/a_x and A_z/a_z, but it extends the pdf tails of A_y/a_y.

6.3.3 Lagrangian autocorrelation function

Particles dispersion and dynamics in turbulent flow can be characterized using their Lagrangian velocity and acceleration time scales, T_v and T_a, which are defined as the integral of the LAF of particles velocity and acceleration over time, respectively (Taylor, 1921; Sawford, 1991; Calzavarini et al., 2012). The LAF of particles streamwise velocity for a given wall-normal location of y_s at a time shift of Δt can be estimated as

$$\rho_{u'u'}(\Delta t, y_s) = \frac{\langle u'(t_s, y_s)u'(t_s + \Delta t, y_s)\rangle}{\sqrt{\langle u'^2(t_s, y_s)\rangle\langle u'^2(t_s + \Delta t, y_s)\rangle}}, \tag{6.1}$$

where $u'(t_s + \Delta t, y_s) = U(t_s + \Delta t, y_s) - \langle U(t_s + \Delta t, y_s)\rangle$, and $\langle U(t_s + \Delta t, y_s)\rangle$ is the ensemble average of the instantaneous streamwise velocity of the particles which have been located

at y_s at the time t_s. For each trajectory, the initial time, t_s, is set as soon as its wall-normal position locates within an interval of width 125μm around y_s. To minimize the effect of wall-normal variation of St_e on the LAF, only the segment of a trajectory which its y meets the condition $y_s - 62.5\mu m \leq y \leq y_s + 62.5\mu m$ is considered for calculating the LAF. The LAF for the other velocity components as well as the acceleration components are calculated similarly.

The effect of Re_τ and C_v on the LAF of velocity and acceleration of particles with $y_s^* = (y_s/\lambda_0) = 10$ is presented in Figure 6.11 as a function of time shift normalized by the t_τ of LU, t^*. As it is expected, the decorrelation rate of velocity is smaller than acceleration, indicating $T_a < T_v$, in all directions. The decorrelation rate of velocity and acceleration in the streamwise direction is smaller than wall-normal and spanwise directions. This is also expected considering the preferential orientation of vortical structures near the wall in the streamwise direction and the effect these structures on the wall-normal and spanwise motion of particles. With increasing Re_τ, the vortical structures become stronger and more frequent, resulting in a faster reduction of the velocity and acceleration LAF (i.e. smaller T_v and T_a, respectively) in all directions. At the higher C_v, the LAF of streamwise and wall-normal velocity and acceleration approaches zero at a larger gradient due to the more frequent PPI. The effect of C_v on the LAF of the velocity and acceleration in the spanwise direction is smaller than streamwise and wall-normal directions.

6.3.4 Particle-particle interaction

The influence of Re_τ and C_v on PPI rate and V_r of particles is investigated in this section. A schematic representation of two particles, P_1 and P_2, is presented in Figure 6.12 showing the instantaneous position and velocity vectors ($\vec{R}$ and $\vec{V}$, respectively) of their centers. The relative position and velocity vectors for these two particles can be defined as $\vec{R}_r = \vec{R}_2 - \vec{R}_1$ and $\vec{V}_r = \vec{V}_2 - \vec{V}_1$, respectively. For two approaching particles $\vec{V}_r \cdot \vec{R}_r < 0$. Here, a PPI is defined when the distance between the center of two approaching particles, $|\vec{R}_r|$, reaches to less than 250μm.

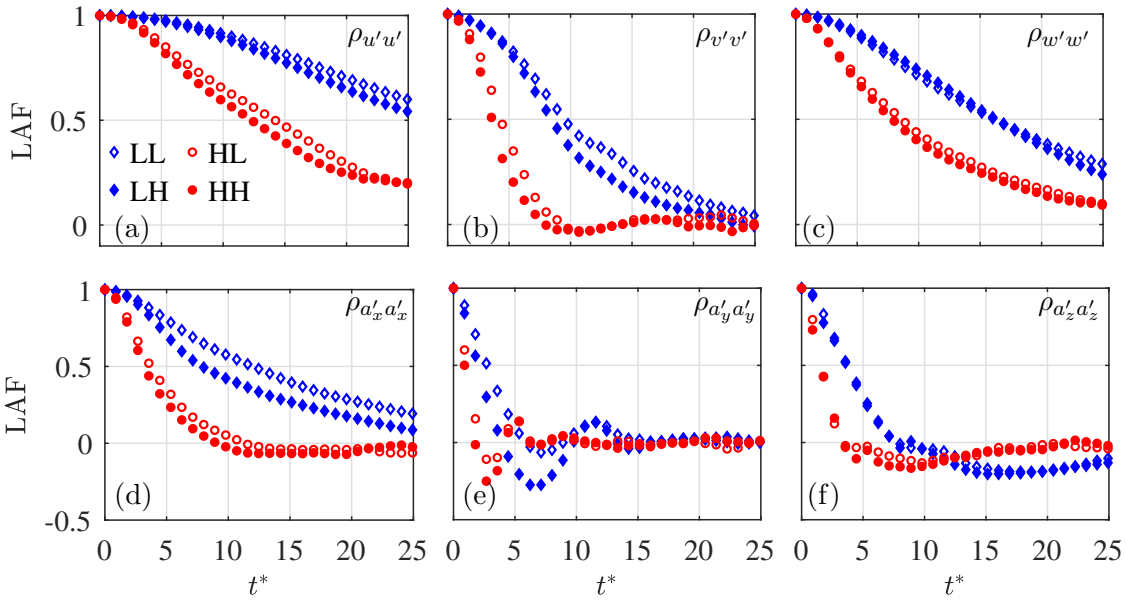

Figure 6.11: Lagrangian autocorrelation function of particles (a-c) velocity and (d-f) acceleration at $y^* = 10$. Acronyms are defined in Table 6.2. Only one of every three data points is presented for clarity.

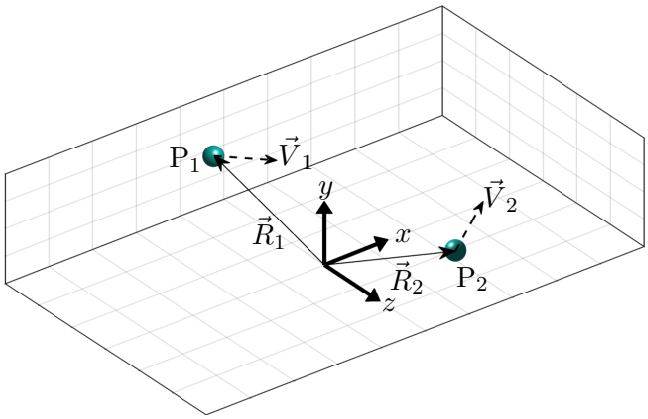

Figure 6.12: Schematic view of two particles (P_1 and P_2), their position vectors with respect to the center of the coordinate system ($\vec{R}_1$ and $\vec{R}_2$) and their velocity vectors ($\vec{V}_1$ and $\vec{V}_2$).

The number of PPI detected in each bin is normalized by the average number of PPI across all the bins and presented as $\bar{f}_p$ in Figure 6.13(a). The $\bar{f}_p$ is larger in the vicinity of the wall, where the turbulent kinetic energy of particles is higher, and it decreases with increasing y^*. With increasing Re_τ, the $\bar{f}_p$ is reduced close to the wall and increased away from the wall. This is similar to the effect of increasing Re_τ on the wall-normal distribution of particle number density seen in Figure 6.4. The influence of increasing C_v on $\bar{f}_p$ is also similar to its effect on $\bar{N}$ shown in Figure 6.4: decreases $\bar{f}_p$ close to the wall and increases it away from the wall. It is conjectured from the comparison of Figure 6.13(a) with Figure 6.4 that similar to the particle-laden isotropic turbulent flows (discussed in Section 2.2.1.2), the PPI rate in near-wall non-isotropic turbulence depends on the particle number density. This comparison also confirms that particle number density is not a dominant factor for PPI rate at least for the higher Re_τ as the peaks of $\bar{f}_p$ and $\bar{N}$ occur at different y^*.

The magnitude of the relative velocity vector, $V_r = |\vec{V}_r|$, is determined for each PPI when the particles reach their minimum $|\vec{R}_r|$. The mean relative velocity of all PPI in each bin, $\langle V_r \rangle$, is normalized by $u_{\tau 0}$ and presented in Figure 6.13(b) as V_r^*. The V_r^* of all the flows is larger close to the wall, where particles have high turbulent kinetic energy, and it decreases by increasing y^*. As expected, by increasing Re_τ the V_r^* increases. The larger fluctuation of particles at the higher Re_τ increases their relative velocity. The V_r^* also increases with increasing C_v due to the larger wall-normal momentum transfer by particles from high-speed regions to low-speed regions at the higher C_v. The V_r^* of all the flows peaks close to the wall at $y^* = 10$. This location coincides with the location of maximum $\bar{f}_p$ as seen in Figure 6.13(a), confirming the relation of particles relative velocity and PPI rate in near-wall non-isotropic turbulent flows. At $y^* = 10$, the effect of C_v on V_r^* is larger at the lower Re_τ since this location coincides with the location of the peak of particles concentration at this Re_τ.

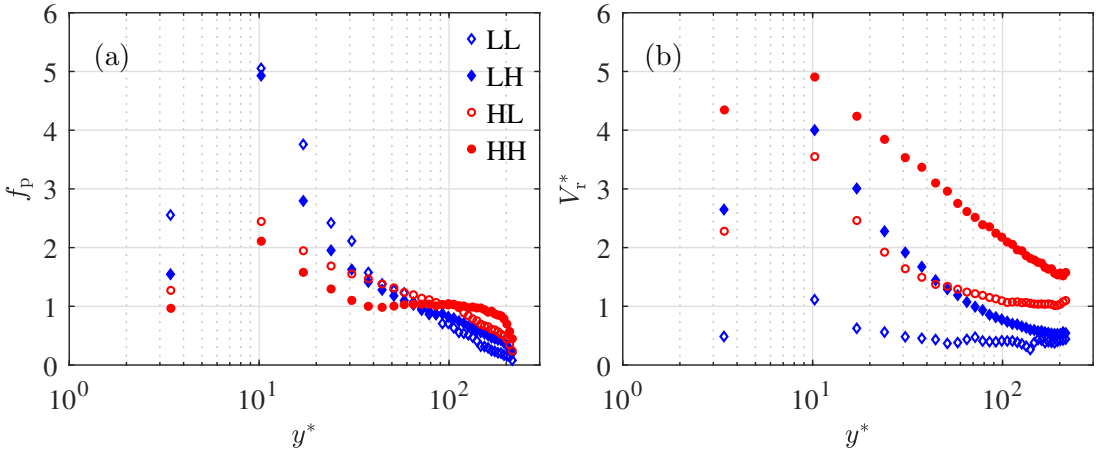

Figure 6.13: The wall-normal variations of normalized (a) PPI rate and (b) relative velocity. Acronyms are defined in Table 6.2.

6.3.5 Particle-wall interaction

The effect of Re_τ and C_v on PWI is investigated in this section by studying their influence on the velocity components of particles before colliding with the wall (U_i, V_i, W_i) and their impact angle, $\theta_i = \arctan(V_i/U_i)$. Investigation of particles size distribution using 2D images showed a standard deviation of approximately $0.1d_p$ for the diameter of particles. Therefore, considering that we track the center of particles, the minimum wall-normal distance ($y_{\min}$) for the trajectory of a particle that collides with the wall should be within $0.45d_p \leq y_{\min} \leq 0.55d_p$ as shown in Figure 6.14. The level of measurement noise in estimating the wall-normal location of particles is reduced to less than 0.5 µm after applying the quadratic regression function, see Section 4.3.3. Therefore, the PWI time is defined as the period when the y of a colliding particle is $y \leq (y_{\min} + 0.5\mu\text{m})$. The impact and rebound angle/velocity are estimated using the average of the associated parameter over five time steps (0.5 ms) right before and after PWI, respectively.

The pdfs of θ_i and the impact velocity components, which are normalized by $u_{\tau 0}$ and presented as U_i^*, V_i^*, and W_i^*, are indicated in Figure 6.15. At the higher Re_τ, the pdf of θ_i is narrower showing the reduction of impact angle by increasing Re_τ. This is expected since increasing Re_τ reduces the magnitude of V/U ratio for particles close to the wall as

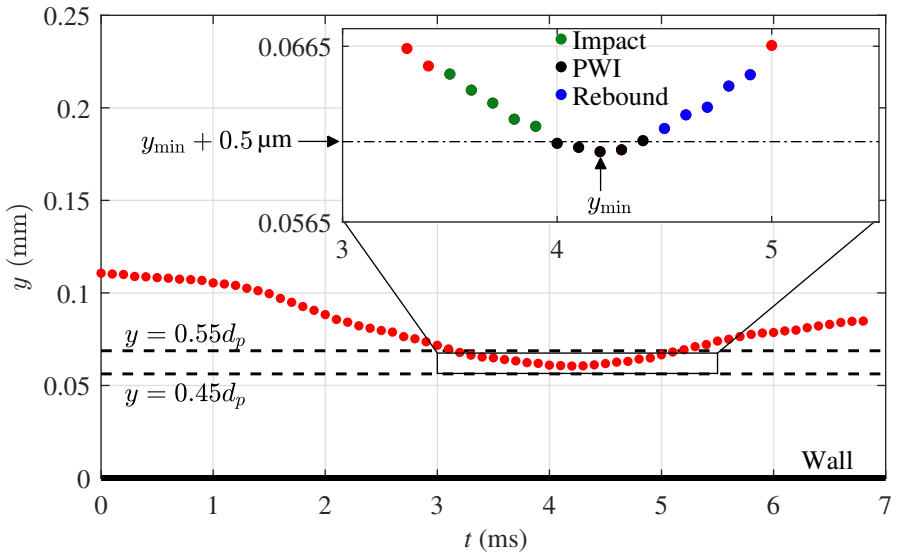

Figure 6.14: Sample of the trajectory of a particle colliding with the wall located at $y = 0$. Symbols show the wall-normal location of the center of the particle in time. The area between the dashed lines shows the acceptable range for $y_{\min}$ of a colliding particle. The inset shows a magnified view of the particle trajectory within 3 ms $< t <$ 5.5 ms. The period of time when $y \leq (y_{\min} + 0.5\mu\text{m})$ is considered as PWI time. The impact and rebound angle/velocity are calculated by averaging the associated parameter over five time steps before and after PWI, respectively.

seen in Figure 6.3(a). However, increasing Re_τ does not significantly affect the value of the most frequent θ_i which is approximately -2 degrees for all the experiments.

By increasing Re_τ, the pdf of U_i^* is shifted toward larger magnitudes and its tails become wider. For LL and LH, the peak of the pdf of U_i^* is at $U_i^* \approx 4$ while it is at $U_i^* \approx 16$ and 18 for HL and HH, respectively. The pdfs of V_i^*, and W_i^* are also extended to larger magnitudes at the higher Re_τ. The pdf of V_i^* peaks at approximately -0.25 and -0.55 for the lower and higher Re_τ, respectively. Due to the homogeneity of the flow field in the spanwise direction, the pdf of W_i^* is symmetric and peaks at $W_i^* = 0$ for all the flows.

At the higher C_v the pdf of large θ_i is slightly increased, showing the more frequent wall collision of particles with larger θ_i. This is consistent with the larger pdf of V/U for near-wall particles shown in Figure 6.3(a). With increasing C_v, the pdf of U_i^* is slightly shifted to larger values. This is also expected since increasing the C_v increases the U^* of the particles close to the wall as seen in Figure 6.2(b). The pdfs of large magnitudes of V_i^*,

and W_i^* are also slightly increased by increasing C_v. Increasing C_v also slightly shifts the peak of V_i^* pdf to the larger magnitudes.

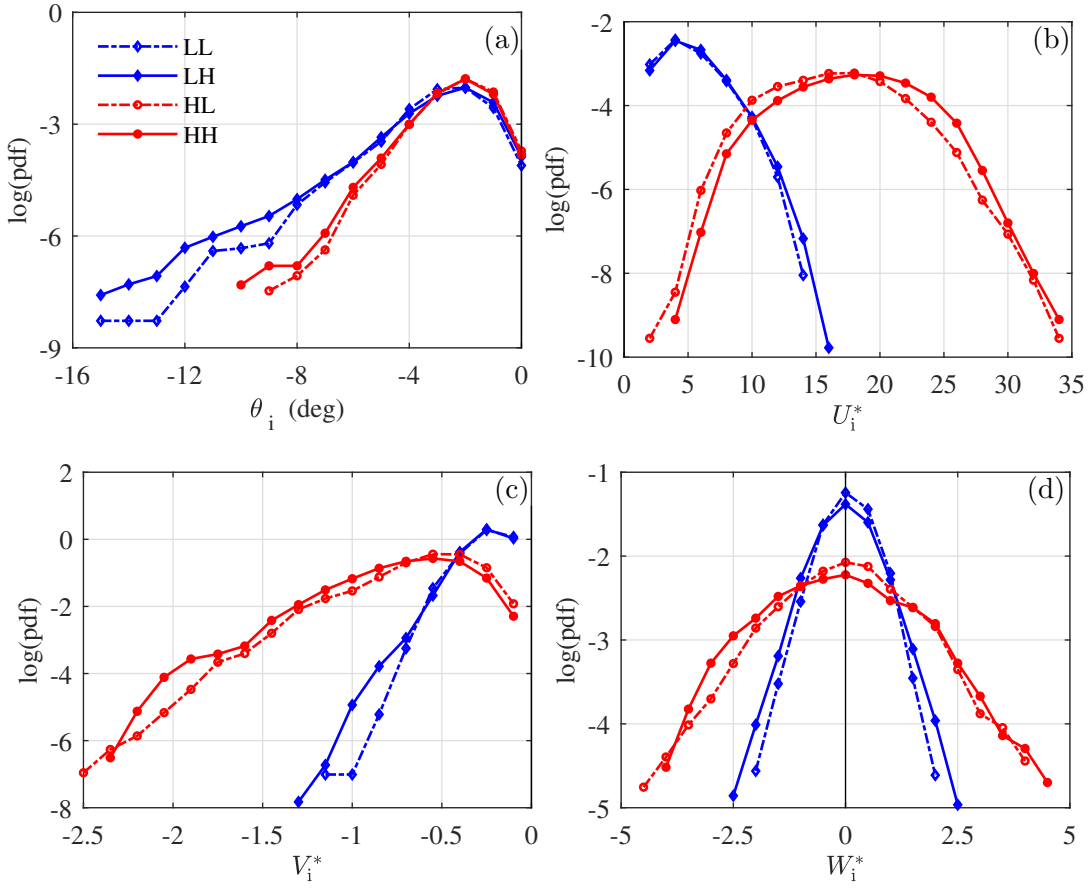

Figure 6.15: The pdf of (a) θ_i, (b) U_i^*, (c) V_i^*, and (d) W_i^*. Acronyms are defined in Table 6.2.

The wall-normal restitution ratio, e_V, is a key factor in particle-wall collision modeling (e.g. Tsuji et al. 1987; Sommerfeld and Huber 1999; Kosinski and Hoffmann 2009). It is defined as the ratio of the wall-normal velocity after collision, V_{rb}, to V_i. Here, the V_{rb} is estimated using the average of V of the colliding particles over five time steps (0.5 ms) right after PWI (see Figure 6.14). Previous investigations showed that e_V depends on θ_i (e.g. Salman et al. 1989; Joseph and Hunt 2004; Sommerfeld and Lain 2018). The effect of Re_τ and C_v on $\langle e_V \rangle$ of colliding particles with different θ_i is investigated in Figure 6.16. The analysis is applied to the particles with $\theta_i \geq -4$ to ensure statistical convergence since most

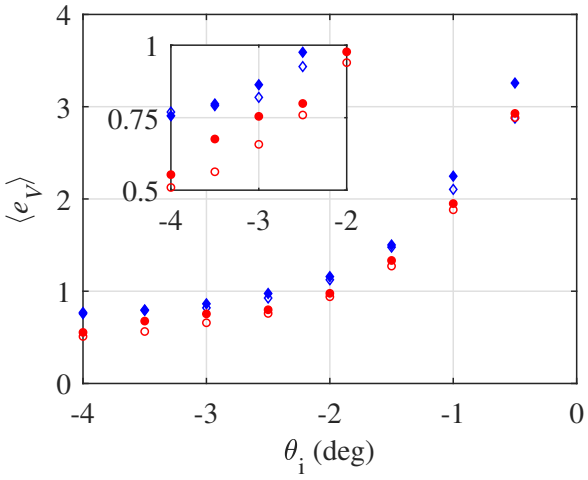

Figure 6.16: The variation of $\langle e_V \rangle$ with θ_i. The values of $\langle e_V \rangle$ are only presented for $\theta_i \geq -4$ to ensure the statistical convergence. The inset shows a zoomed-in view of the figure for $-4 \leq \theta_i \leq -2$.

of the colliding particles have θ_i within this range as seen in Figure 6.15(a).

In general, the $\langle e_V \rangle$ is reduced by reducing θ_i which is consistent with the observations of Salman et al. (1989), Sommerfeld and Huber (1999), and Sommerfeld and Lain (2018) in solid-gas flows and Joseph and Hunt (2004) in solid-liquid flow. Particles with $\theta_i > -2$ have $\langle e_V \rangle > 1$. The $\langle e_V \rangle > 1$ for colliding particles with shallow θ_i was also reported by Sommerfeld and Huber (1999). With increasing Re_τ, the $\langle e_V \rangle$ of particles is reduced. This is related to the larger shear rate at the higher Re_τ which increases particles' angular velocity (Drew and Passman, 2006). Lukerchenko et al. (2012) showed that increasing the angular velocity of a colliding particle reduces its e_V. With increasing C_v, $\langle e_V \rangle$ increases. This is related to the larger magnitude of the V of particles that move toward the wall and collide with it at the higher C_v as it was seen in Figures 6.3(a) and 6.15(c), respectively. Falcon et al. (1998) showed that increasing the magnitude of V_i increases e_V.

6.4 Summary and conclusion

The motion of G-125 particles in near-wall non-isotropic particle-laden turbulent channel flows was investigated using Lagrangian 3D-PTV. Experiments were performed at Re_τ of 410 and 765 and at $C_v = 0.03$ and 0.15%, respectively. Results showed the effect of Re_τ and

C_v on particles wall-normal distribution, velocity and acceleration, Lagrangian time scales, PPI, and PWI.

As expected, with increasing Re_τ, the mean turbulent kinetic energy of particles increased in all directions and over all frequencies. At $y^* < 20$ the A_x^* of particles was negative due to the dominating effect of shear stress applied on the particles by the surrounding fluid. This shear stress increases with increasing Re_τ, resulted in the larger streamwise deceleration of particles. The A_x^* increased with increasing y^*, became positive and then and gradually reduced to zero at $y^* > 20$. The positive A_x^* was due to the effect of drag force applied on the particles that were moving away from the wall. The positive A_x^* was larger at the higher Re_τ due to the stronger ejection motions that pushed particles further away from the wall with a larger drag force. The A_y^* was positive at $y^* < 40$ under the effect of the drag force applied by the ejection motions, Magnus force and the wall-normal pressure gradient caused by quasi-streamwise vortices. These forces were larger at the higher Re_τ and increased the A_y^*. Further away from the wall the A_y^* became negative under the effect of gravity. Despite the significant effect of Re_τ on the rms of acceleration in all directions, the pdfs of A_x/a_x, A_y/a_y, and A_z/a_z were independent of Re_τ away from the wall at $y^* = 105$ and 215. Very close to the wall at $y^* = 3.4$, however, increasing Re_τ narrowed these pdfs and reduced their values. This effect was more significant for the pdf of A_x/a_x. Investigation of LAF of particles velocity and acceleration showed the lower Lagrangian velocity and acceleration time scales in all directions at the higher Re_τ. The effect of increasing Re_τ on the wall-normal variation of $\bar{f}_p$ was similar to its effect on $\bar{N}$; it reduced $\bar{N}$ and $\bar{f}_p$ at $y^* < 70$ and increased them at $y^* > 70$. Investigation of particles interacting with each other also showed that they have larger V_r^* at the higher Re_τ. The analysis of the trajectory of particles that interacted with the wall showed that increasing Re_τ shifted the pdfs of impact velocity toward larger magnitudes in all directions, but it narrowed the pdf of impact angle to a smaller range of θ_i and reduced $\langle e_V \rangle$.

By increasing C_v the turbulent kinetic energy of particles decreased in the streamwise direction and increased it in the wall-normal direction. The larger PPI rate at the higher

C_v, converted a larger streamwise kinetic energy of particles to wall-normal kinetic energy and reduced the A_x^* and increased A_y^*. Investigation of A_x/a_x, A_y/a_y, and A_z/a_z pdfs in different y^* showed that they are independent of C_v except for the pdf of A_y/a_y that became slightly wider at the higher C_v. The analysis of the velocity and acceleration LAFs showed the reduction of Lagrangian time scales in all directions with increasing C_v. This effect was less significant in the spanwise direction. The effect of C_v on the wall-normal variation of $\bar{f}_p$ and $\bar{N}$ was similar; increasing C_v reduced $\bar{N}$ and $\bar{f}_p$ close to the wall and increased them away from the wall. The V_r^* also increased by increasing C_v. The effect of C_v on V_r^* was more significant close to the wall and gradually reduced by increasing y^*. The PWI analysis illustrated that increasing C_v increases the interaction of particles with large θ_i with the wall. It also slightly shifted the pdfs of U_i^* and V_i^* toward larger magnitudes and increased the $\langle e_V \rangle$.

Chapter 7

Near-wall motion of non-spherical particles in turbulent channel flow

7.1 Introduction

The shape of a particle has an important effect on its motion as discussed in Section 2.3. The effect of inertial particles' shape on their velocity statistics in particle-laden turbulent flows has been recently investigated in a few numerical studies including van Wachem et al. (2015) and Sommerfeld and Lain (2018). van Wachem et al. (2015) investigated the motion of regularly-shaped non-spherical particles in a gas-solid horizontal turbulent channel flow at $Re_\tau = 600$ and compared it with the motion of spherical particles with the same density (2.5 g/cm^3) and equivalent diameter ($\approx 200\mu$m). The mass loading (the ratio of the mass of particles to the mass of the fluid) of particles was equal to one in their simulation. Results showed that the concentration of non-spherical particles was larger close to the lower wall and smaller away from it compared with the spherical particles. In addition, the streamwise velocity of non-spherical particles was smaller than spherical particles across the channel. Sommerfeld and Lain (2018) compared the motion of irregularly-shaped particles with spherical particles with the same density (2.65 g/cm^3) and equivalent diameter ($\approx$ 185μm) in a gas-solid horizontal turbulent channel flow with the particle mass loading of 0.1. The simulation of Sommerfeld and Lain (2018) showed that the concentration of non-spherical particles was smaller than the spherical particles near the wall and larger away from it. Their results also showed that the streamwise velocity of non-spherical particles

was larger than the spherical particles across the channel. Given the limited number of studies on the effect of particle shape on its dynamics, experimental investigation of the motion of spherical and non-spherical particles with similar density and equivalent diameter in a turbulent flow is essential for better understanding and more accurate modeling of non-spherical particles motion in turbulent flows.

In addition to the particle shape, the size of a particle also affects its motion in turbulent flows. Kussin and Sommerfeld (2002), Borée and Caraman (2005) and Ahmadi et al. (2019) have experimentally investigated the effect of particle size on the velocity statistics of spherical inertial particles (with similar concentration) in turbulent flows. Experiments of Kussin and Sommerfeld (2002) in a horizontal gas-solid turbulent channel flow with particle mass loading of one showed that increasing particle size reduced the mean streamwise velocity, $\langle U \rangle$, of particles across the channel and made its profile more uniform in the wall-normal direction. Results of the experiments of Borée and Caraman (2005), performed in a vertical gas-solid turbulent pipe flow at low and high particle mass loading of 0.11 and 1.1, indicated that bigger particles had larger $\langle U \rangle$ than the smaller particles close to the wall and slightly smaller $\langle U \rangle$ at the pipe centerline at both mass loading. The experiments by Ahmadi et al. (2019) in a horizontal solid-liquid turbulent channel flow at C_v of 0.05% also illustrated that increasing particle size increased the $\langle U \rangle$ of near-wall particles while it had a negligible effect on the $\langle U \rangle$ of particles away from the wall.

The effect of particle size on the velocity fluctuation of particles was also investigated by Kussin and Sommerfeld (2002), Borée and Caraman (2005), and Ahmadi et al. (2019). Results of the experiments performed by Kussin and Sommerfeld (2002) showed larger streamwise fluctuation across the channel for bigger particles. However, the results of Borée and Caraman (2005) showed smaller streamwise fluctuation close to the wall and larger away from it for bigger particles. They also indicated that bigger particles had slightly larger wall-normal fluctuation across the pipe. Investigations of Ahmadi et al. (2019) showed the reduction of streamwise and wall-normal particles fluctuation across the channel by increasing the particle size. This reduction was more significant near the wall. More

experimental investigations can help to better understand reasons for differences between results of the reviewed studies and improve our understanding of the effect of particle size on the velocity statistics of particles in turbulent flows.

The influence of particle size on the acceleration statistics of inertial particles in turbulent air flows has been experimentally investigated by Ayyalasomayajula et al. (2006), Gerashchenko et al. (2008) and Qureshi et al. (2008). The Lagrangian measurement of water droplets acceleration in a grid generated turbulence in a wind tunnel by Ayyalasomayajula et al. (2006) with particle mass loading of 10^{-4} showed that increasing particle size reduced the rms of their streamwise acceleration. The experiments of Gerashchenko et al. (2008) using droplets in a wind tunnel with particle mass loading of 10^{-4}, however, indicated an opposite trend. Their measurements showed the increment of the rms of droplets streamwise acceleration by increasing their size. The experiments of Qureshi et al. (2008) in a wind tunnel using inertial particles with different sizes showed that the effect of particle size on its rms of acceleration was not monotonic. They also showed that the pdf of the streamwise acceleration normalized by its rms did not significantly depend on particle size. This was in contrast to the measurements of Ayyalasomayajula et al. (2006) and Gerashchenko et al. (2008) that showed narrower tails of the normalized pdf of acceleration for bigger particles. More experimental studies of particles acceleration in turbulent flows are essential to scrutinize these contradictions.

In this chapter, first, the near-wall motion of non-spherical quartz particles (Q-250) is studied in comparison with the spherical glass particles (G-250). The near-wall particle distribution, velocity and acceleration statistics, and PWI characteristics of Q-250 and G-250 particles are compared to investigate the effect of particle shape on these parameters. The effect of particle size on the distribution, velocity and acceleration statistics, and PWI characteristics is also studied in this chapter for both spherical and non-spherical particles.

The flow facility that was used for conducting the experiments of this chapter is introduced in Section 3.1. The measurement system, data processing, and uncertainty analysis are detailed in Section 4.2. The accuracy of the measurement system is also evaluated in

Section 7.3.1 by comparing the measured velocity statistics of unladen flow with those of DNS of Tanahashi et al. (2004). The near-wall motion of G-250 particles is compared with the G-250 particles in Section 7.3.2. The effect of particle size on the near-wall motion of spherical and non-spherical particles is investigated in Section 7.3.3. Finally, the conclusions are summarized in Section 7.4.

7.2 Experimental design

The unladen flow experiment was conducted at a mass flow rate of 3.21 kg/s and a constant temperature of 25°, resulting in the Re_H of approximately 30,000. Table 7.1 presents the main parameters of the unladen flow including the U_b, u_τ, λ, t_τ and Re_τ.

Re_H	Re_τ	U_b(m/s)	u_τ(m/s)	λ(μm)	t_τ(μs)
30,000	770	1.79	0.09	9.7	106

Table 7.1: The main parameters of the unladen flow. The inner scaling is calculated based on the velocity profile of the unladen flow measured using 2D-LPT.

Six particle-laden flow experiments were performed at the similar mass flow rate and temperature of the unladen flow experiment using spherical glass particles (detailed in Section 3.4) and non-spherical quartz particles (detailed in Section 3.5). The particles were dispersed in water at a volume concentration of 0.01% for each particle-laden experiment. At this low solid volume concentration, the effect of particles on the fluid and the motion of other particles is negligible. Table 7.2 presents the characteristics of the conducted experiments including the particle type, the number of collected images, N_{im}, the approximate number of the detected trajectories, N_{tr}, using 2D-LPT, d_p^+, St^+, and the maximum Re_{ps}. The maximum Re_{ps} was estimated using Equation 2.13 based on the maximum $U_s = |\langle U_f \rangle - \langle U_p \rangle|$ in the measurement domain. The random error of the measured velocity and acceleration statistics of particle-laden flow experiments were investigated in Section 4.2.3.

Experiment	Particle type	$N_{im} \times 10^{-3}$	$N_{tr} \times 10^{-6}$	d_p^+	St^+	max(Re_{ps})
Unladen	-	70	5.9	-	-	-
Particle-laden	G-125	419	1.2	13.9	17.2	33.9
Particle-laden	G-250	419	0.2	28.3	71.3	35.0
Particle-laden	G-420	419	0.06	47.2	197.9	21.1
Particle-laden	Q-125	419	1.1	14.2	17.9	48.1
Particle-laden	Q-250	419	0.2	29.2	75.5	64.5
Particle-laden	Q-420	419	0.05	48.8	211.1	56.3

Table 7.2: The characteristics of the experiments performed for this chapter. The values of d_p^+, St^+, and Re_{ps} were determined based on the d_{50} of the associated particle type.

7.3 Results and discussion

In the following sections, first, the accuracy of the measurement system is evaluated in Section 7.3.1 by comparing the velocity statistics of the unladen flow with the DNS of Tanahashi et al. (2004) at $Re_\tau = 800$. Then, in Section 7.3.2, the distribution, velocity, acceleration, and PWI of non-spherical particles (Q-250) are investigated and compared with those of the spherical particles with similar density and equivalent size (G-250). Finally, in Section 7.3.3, the effect of particle size on the distribution, velocity and acceleration statistics, and PWI characteristics is investigated for spherical and non-spherical particles.

7.3.1 Unladen turbulent flow

The velocity statistics of the unladen flow were averaged in the streamwise and spanwise directions and in time. The wall-normal size of the averaging bin was equal to λ. The measured average streamwise velocity, $\langle U \rangle$, of the unladen flow is compared with that of the DNS of Tanahashi et al. (2004) performed at $Re_\tau = 800$ in a semi-logarithmic presentation in Figure 7.1(a). In this figure, the normalized mean streamwise velocity, $U^+ = \langle U \rangle / u_\tau$, is presented as a function of the normalized wall-normal distance $y^+ = y/\lambda$. The U^+ profile resulted from 2D-LPT measurement agrees with the DNS from $y^+ \approx 4$ up to $y^+ \approx 310$ in the log-layer, showing the accuracy of the 2D-LPT system in mean flow measurement and

the fully developed state of the turbulent channel flow.

Figure 7.1(b) shows a comparison between the measurement and the DNS of Tanahashi et al. (2004) for the streamwise and wall-normal Reynolds stresses, $\langle u^2 \rangle$ and $\langle v^2 \rangle$, respectively. The $\langle u^2 \rangle$ and $\langle v^2 \rangle$ are normalized by u_τ^2 and presented as $\langle u^2 \rangle^+$ and $\langle v^2 \rangle^+$, respectively. The maximum deviation of $\langle u^2 \rangle^+$ and $\langle v^2 \rangle^+$ from the DNS is about 4 and 7%, occurred at $y^+ \approx 18$ and 70, respectively. The agreement of the 2D-LPT results with the DNS shows the measurement accuracy for the streamwise and wall-normal Reynolds stresses. The wall-normal variation of the average shear Reynolds stress, $\langle uv \rangle$, of the unladen flow is also presented in Figure 7.1(b).

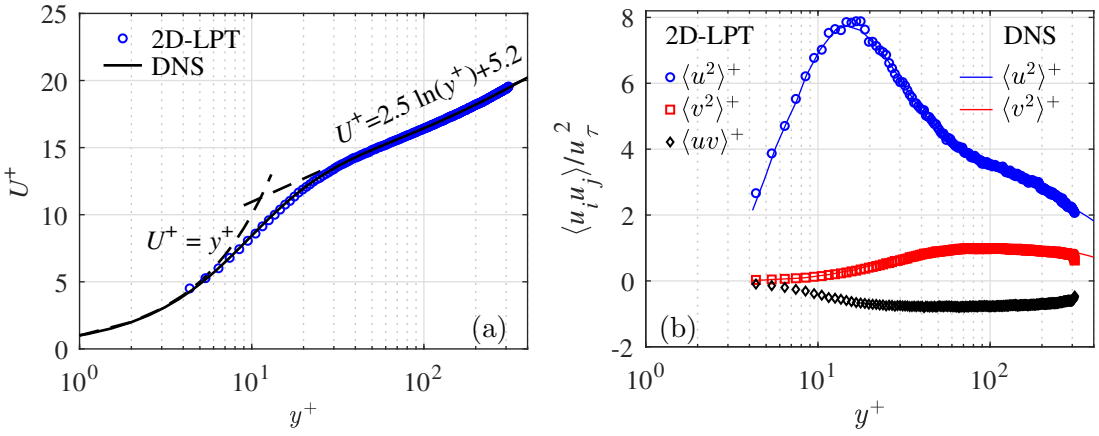

Figure 7.1: Comparison of 2D-LPT measurement of normalized (a) mean streamwise velocity and (b) Reynolds stresses of the unladen flow at $Re_\tau = 770$ (symbols) with the DNS results of Tanahashi et al. (2004) at $Re_\tau = 800$ (solid lines).

7.3.2 Near-wall motion of non-spherical particles

The effect of particle shape on the near-wall motion of particles is investigated in this section by comparing the distribution, velocity and acceleration statistics and PWI of G-250 and Q-250 particles. The velocity and acceleration statistics of particles are averaged in the streamwise and spanwise directions and in time. The wall-normal size of the averaging bin is set to 250 μm.

7.3.2.1 Particles distribution

The particles number density, $\bar{N}$, calculated as the number of particles in each bin divided by the average number of particles in all the bins, is presented in Figure 7.2 for G-250 and Q-250 particles. The concentration of Q-250 particles is larger than the G-250 particles at $y^+ < 130$ and it becomes smaller farther from the wall. This observation is consistent with the numerical results presented by van Wachem et al. (2015) and contrary to the results of Sommerfeld and Lain (2018). van Wachem et al. (2015) argued that the higher concentration of non-spherical particles near the wall is due to the alignment of their major axis with the wall in this region which reduces the effect of turbulent suspension on them. They showed that the angle between the major axis of the particles and the wall was smaller in the vicinity of the wall.

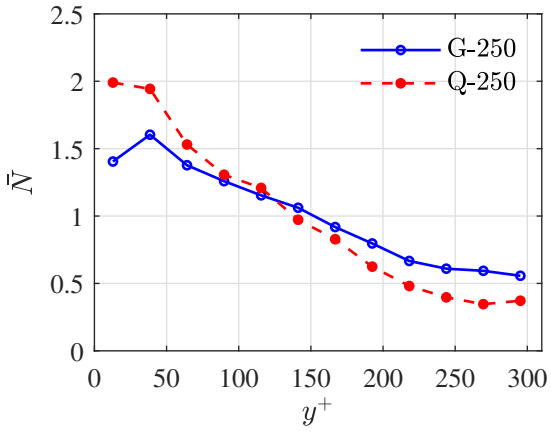

Figure 7.2: Comparison of the number density of G-250 and Q-250 particles.

7.3.2.2 Particles velocity statistics

Figure 7.3(a) indicates the U^+ profile for the unladen flow, G-250, and Q-250 particles. The U^+ of particles is larger than the unladen flow close to the wall at $y^+ = 13$, since the no-slip boundary condition does not apply to them, while they are smaller than the unladen flow farther from the wall, due to the higher inertial of the particles than the fluid. The U^+ of G-250 and Q-250 particles are almost the same except at $y^+ = 13$ where Q-250 has a larger U^+. The larger U^+ of non-spherical particles near the wall can be due to

their higher concentration in this region. The wall-normal variation of the $\langle u^2\rangle^+$, $\langle v^2\rangle^+$, and $\langle uv\rangle^+$ profiles of G-250 and Q-250 particles are compared in Figure 7.3(b). As seen, the magnitude of $\langle u^2\rangle^+$, $\langle v^2\rangle^+$ and $\langle uv\rangle^+$ of Q-250 particles is smaller than those of G-250 particles close to the wall at $y^+ < 150$. Farther from the wall these magnitudes are almost equal for G-250 and Q-250 particles.

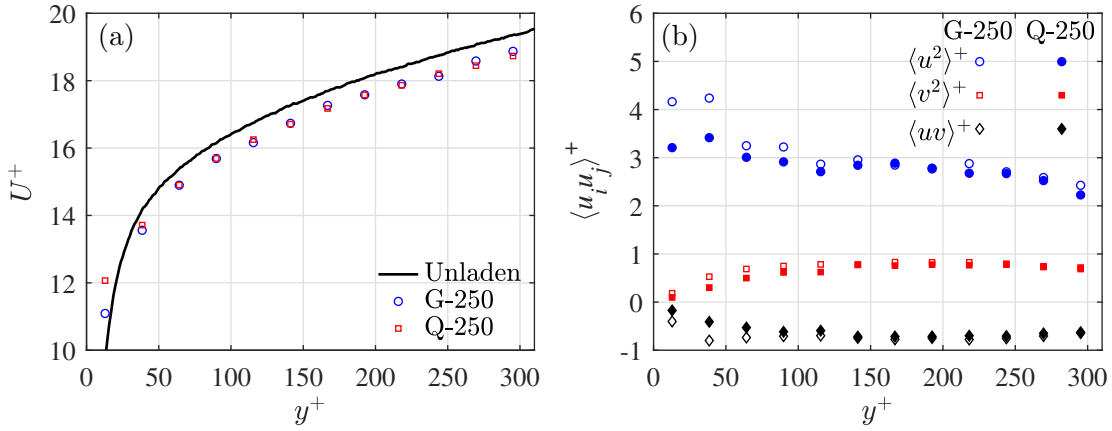

Figure 7.3: Comparison of normalized (a) mean streamwise velocity and (b) velocity fluctuations of G-250 and Q-250 particles.

7.3.2.3 Particles acceleration statistics

The wall-normal variation of the mean streamwise and wall-normal acceleration of G-250 and Q-250 particles are normalized using u_τ and ν and presented in Figure 7.4 as $A_x^+ = \langle A_x\rangle\nu/u_\tau^3$ and A_y^+, respectively. The A_x^+ of Q-250 is smaller than G-250 at $y^+ < 75$ showing that these particles experience a larger streamwise deceleration near the wall. A possible reason for the larger deceleration of non-spherical particles can be their larger surface area compared with the spherical particles which increases the effect of viscous drag on their motion. Farther from the wall at $y^+ > 100$, where the viscous force diminishes, the A_x^+ of G-250 and Q-250 are approximately equal. The A_y^+ of Q-250 particles is approximately twice the A_y^+ of G-250 particles at $y^+ = 13$. Beyond this location, the A_y^+ of G-250 and Q-250 particles are approximately equal. The larger concentration of non-spherical particles near the wall can also be another reason for their larger streamwise deceleration and wall-normal

acceleration in this region as it was also seen in Chapter 6.

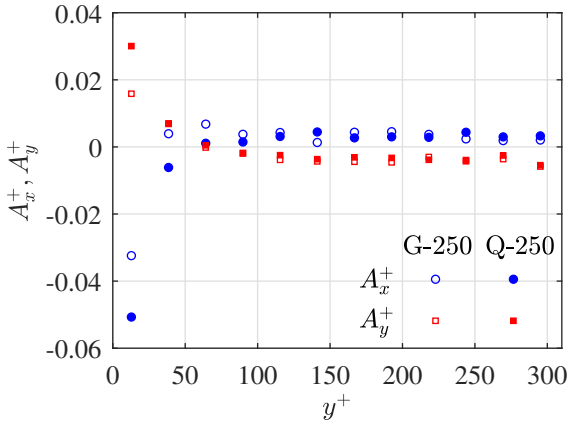

Figure 7.4: Comparison of the A_x^+ and A_y^+ of G-250 and Q-250 particles.

Figure 7.5 compares the pdfs of A_x/a_x and A_y/a_y (where a_x and a_y are the rms of A_x and A_y, respectively) of G-250 and Q-250 particles at $y^+ = 13$, 141 and 270. As this figure shows, the pdfs of A_x/a_x and A_y/a_y do not depend on the particle shape.

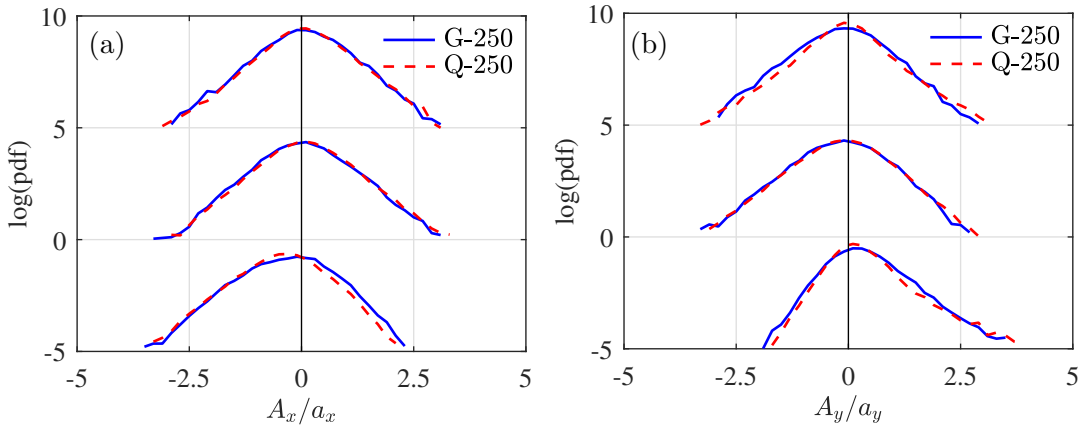

Figure 7.5: Comparison of the pdf of (a) A_x/a_x and (b) A_y/a_y of G-250 and Q-250 particles at $y^+ = 13, 141$ and 270, ordered from bottom to top, respectively. For clarity, the pdfs at $y^+ = 141$ and 270 are shifted up by 5 and 10 units of the vertical axis, respectively.

7.3.2.4 Particle-wall interaction

The interaction of G-250 and Q-250 particles with the wall is investigated in this section by determining the impact and rebound angle/velocity for the particles that collide with

the wall. The impact and rebound angle/velocity are estimated using the average of the associated parameter over five time steps (0.6 ms) right before and after PWI, respectively. The streamwise and wall-normal impact velocity components are normalized by u_τ and presented as U_i^+ and V_i^+, respectively. Figure 7.6(a) compares the pdf of U_i^+ of G-250 and Q-250 particles, showing a larger U_i^+ for Q-250 particles. This is expected since the U^+ of Q-250 particles was larger than the G-250 particles next to the wall, as seen in Figure 7.3. The comparison of the pdfs of V_i^+ of G-250 and Q-250 in Figure 7.6(b) shows a very small shift toward the smaller magnitudes for Q-250 particles. The comparison of Figures 7.6(a) and (b) indicates that the effect of particle shape on U_i^+ is larger than V_i^+. The impact angle of particles that collide with the wall is determined as $\theta_i = \arctan(V_i/U_i)$. Figure 7.6(c) compares the pdf of θ_i of G-250 particles with that of the Q-250 particles. The pdf of θ_i of Q-250 particles is slightly shifted toward the smaller magnitudes indicating that these particles have a smaller impact angle compared to G-250 particles. The reason is the larger U_i of Q-250 particles. Figure 7.6(c) also shows that the the magnitude of most frequent impact angle of non-spherical particles is slightly less than the that of spherical particles.

The mean streamwise restitution ratio, $\langle e_U \rangle$, is determined for G-250 and Q-250 particles and presented in Figure 7.7(a) as a function of θ_i. The $\langle e_U \rangle$ of both particle types decreases by increasing the magnitude of θ_i. The $\langle e_U \rangle$ of Q-250 particles is larger than G-250 particles for all the investigated θ_i, showing that these particles lose less streamwise kinetic energy when they collide with the wall that can result in their higher streamwise velocity close to the wall, as seen in Figure 7.3(a). The difference between the $\langle e_U \rangle$ of G-250 and Q-250 particles is increased by increasing the magnitude of θ_i. The mean wall-normal restitution ratio, $\langle e_V \rangle$, of G-250 and Q-250 particles is also decreased by increasing the magnitude of θ_i, as seen in Figure 7.7(b). The Q-250 particles have larger $\langle e_V \rangle$ than G-250 particles in the range of the investigated θ_i; however, the difference between the $\langle e_V \rangle$ of G-250 and Q-250 particles is decreased by increasing the magnitude of θ_i.

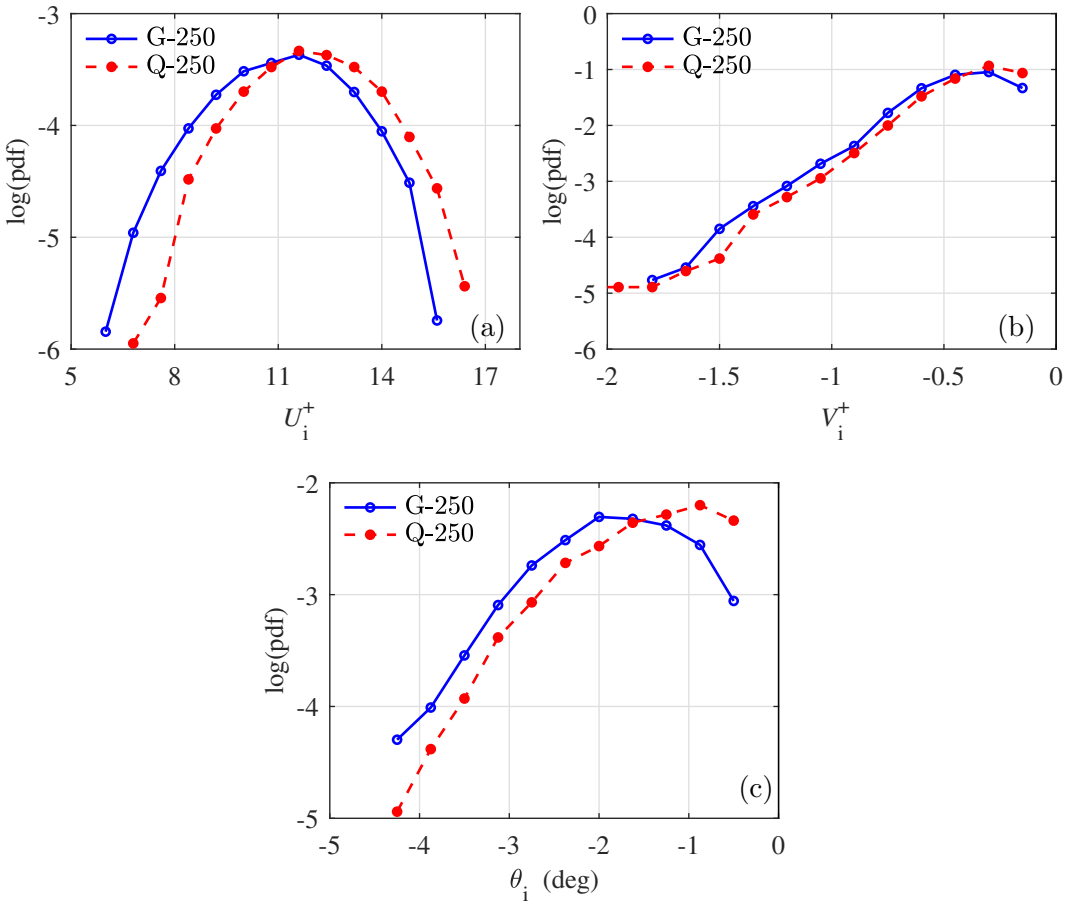

Figure 7.6: Comparison of the pdf of (a) U_i^+, (b) V_i^+ and (c) θ_i of G-250 and Q-250 particles.

7.3.3 Effect of particle size on its near-wall motion

In this section, the effect of particle size on the near-wall motion of both spherical and non-spherical particles is investigated by comparing the distribution, velocity and acceleration statistics, and PWI characteristics of G-125, G-250 and G-420 particles as well as Q-125, Q-250 and Q-420 particles. The velocity statistics of particles are averaged in the streamwise and spanwise directions and in time. In this section, the size of the wall-normal averaging bin is set to 420 μm.

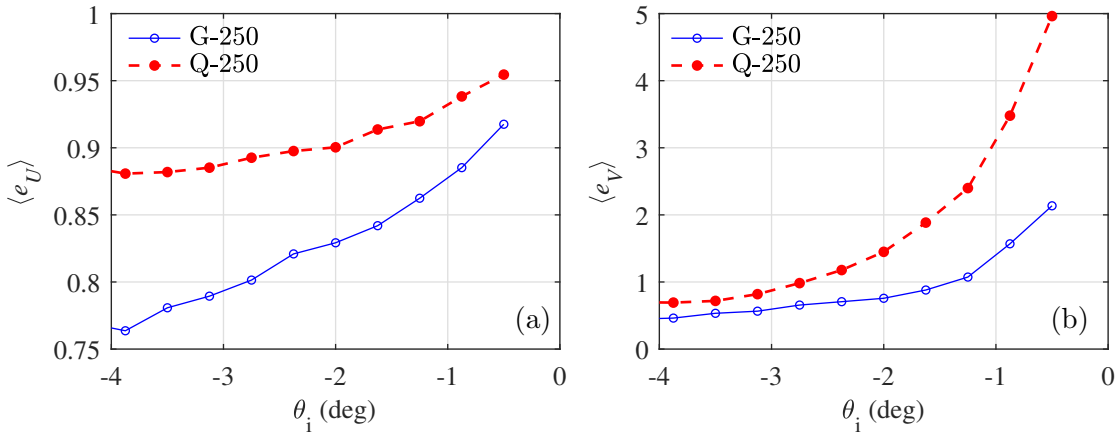

Figure 7.7: Comparison of (a) $\langle e_U \rangle$ and (b) $\langle e_V \rangle$ of G-250 and Q-250 particles.

7.3.3.1 Particles distribution

The wall-normal variation of $\bar{N}$ is presented in Figures 7.8(a) and (b) for glass and quartz particles, respectively. For both glass and quartz particles, increasing particle size increased the $\bar{N}$ of particles near the wall and reduced it away from the wall. This trend was also reported by Ahmadi et al. (2019) who investigated the effect of particle size on the distribution of particles using glass beads in a horizontal solid-liquid turbulent channel flow. They attributed this trend to the larger settling velocity of bigger particles.

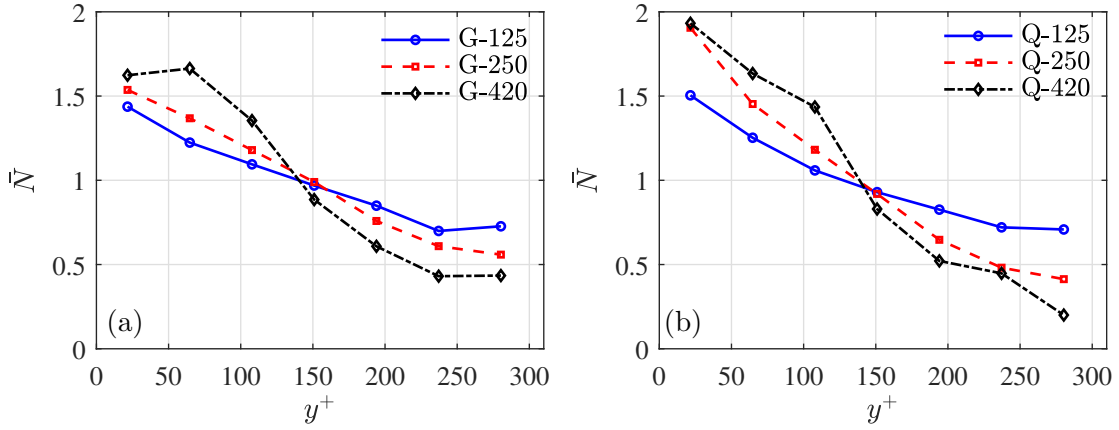

Figure 7.8: Comparison of the particle number density of (a) glass particles and (b) quartz particles.

7.3.3.2 Particles velocity statistics

Figure 7.9 shows the U^+ of glass and quartz particles as a function of y^+. For glass particles, by increasing the particle size the U^+ is increased close to the wall at $y^+ = 22$. Farther from the wall at $y^+ = 280$ for example, increasing the particle size slightly reduces their U^+. The reason can be the larger St of the bigger particles which increases the difference between their U^+ and the fluid. Increasing particle size showed a similar effect on the U^+ of quartz particles, as seen in Figure 7.9(b).

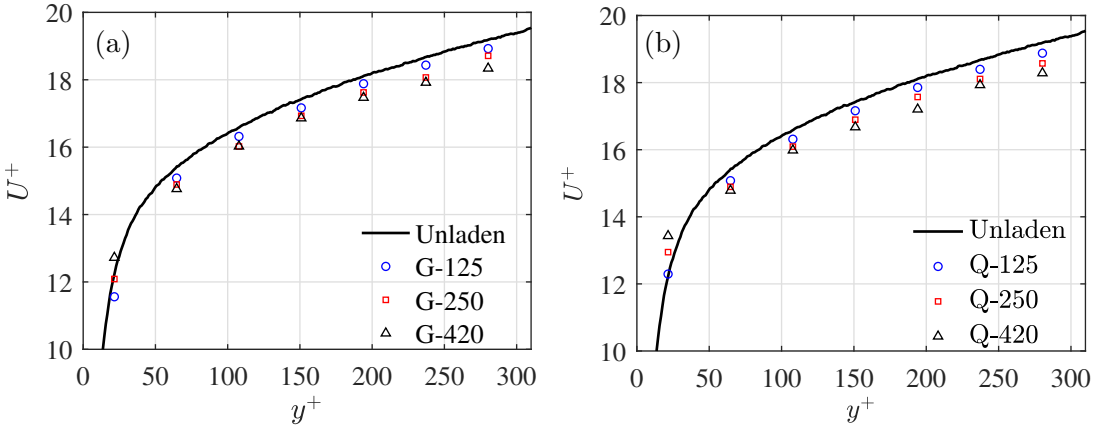

Figure 7.9: Comparison of the U^+ of (a) glass and (b) quartz particles with different sizes.

The effect of particle size on the $\langle u^2 \rangle^+$, $\langle v^2 \rangle^+$, and $\langle uv \rangle^+$ is investigated in Figures 7.10(a) and (b) for glass and quartz particles, respectively. For glass particles, increasing the particle size reduced the $\langle u^2 \rangle^+$. This reduction is more significant close to the wall at $y^+ < 150$. The magnitudes of $\langle v^2 \rangle^+$ and $\langle uv \rangle^+$ are also decreased slightly at $y^+ < 100$ by increasing the size of glass particles. The smaller fluctuation of larger particles is due to their larger St which makes them less responsive to the flow. The difference between St of particles is larger close to the wall which causes a larger reduction to particles fluctuation in this region. Farther from the wall the effect of particle size on $\langle u^2 \rangle^+$, $\langle v^2 \rangle^+$, and $\langle uv \rangle^+$ is small due to the smaller difference between their St. The near-wall reduction of $\langle u^2 \rangle^+$, $\langle v^2 \rangle^+$ and $\langle uv \rangle^+$ of particles by increasing the particle size was also reported by Ahmadi et al. (2019). Increasing the size of particles has a similar effect on the $\langle u^2 \rangle^+$, $\langle v^2 \rangle^+$ and

$\langle uv \rangle^+$ of quartz particles, as seen in Figure 7.10(b).

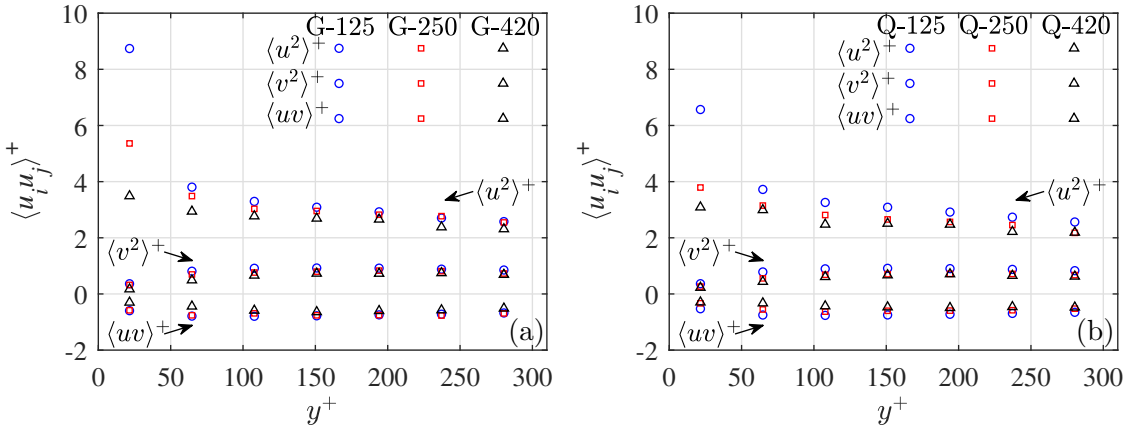

Figure 7.10: Comparison of the velocity fluctuation of (a) glass and (b) quartz particles with different sizes.

7.3.3.3 Particles acceleration statistics

The effect of particle size on the A_x of particles is investigated in Figure 7.11(a) and (b) for glass and quartz particles, respectively. Figure 7.11(a) shows the pdf of normalized A_x for glass particles at $y^+ = 22$, 65, 108 and 151. Increasing the particle size narrowed the pdf of A_x in these wall-normal locations. This behavior was also reported by Qureshi et al. (2007) for neutrally buoyant particles in isotropic turbulence. They attributed this behavior to the larger St of bigger particles which makes them less responsive to the turbulent motions. The effect of particle size on the pdf of A_x is stronger near the wall since it makes larger change in the St due to the smaller flow time scale in this region. Increasing the particle size showed a similar effect on the pdf of A_x of quartz particles, as seen in Figure 7.11(b). The pdf of A_x/a_x at $y^+ = 22$, 65, 108, and 151 is presented in Figure 7.12 for glass and quartz particles, indicating that this pdf does not significantly depend on the particle size, neither for spherical particles, as it was also reported by Qureshi et al. (2007), nor for non-spherical particles.

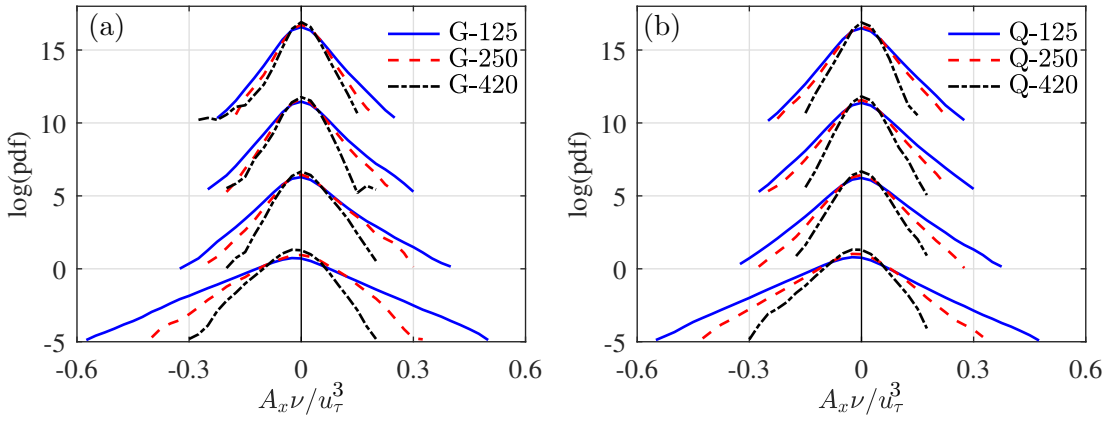

Figure 7.11: Comparison of the pdf of normalized A_x for (a) glass and (b) quartz particles at $y^+ = 22$, 65, 108 and 151, ordered from bottom to top, respectively. For clarity, the pdfs at $y^+ = 65$, 108 and 151 are shifted up by 5, 10 and 15 units of the vertical axis, respectively.

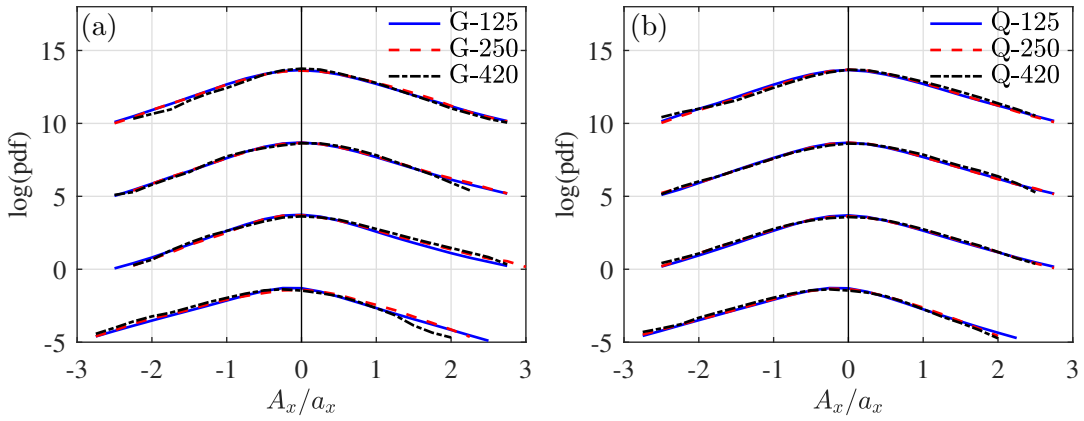

Figure 7.12: Comparison of the pdf of A_x/a_x for (a) glass and (b) quartz particles at $y^+ = 22$, 65, 108 and 151, ordered from bottom to top, respectively. For clarity, the pdfs at $y^+ = 65$, 108 and 151 are shifted up by 5, 10 and 15 units of the vertical axis, respectively.

The pdf of normalized A_y at $y^+ = 22$, 65, 108 and 151 is presented in Figure 7.13 for glass and quartz particles with different sizes. With increasing particle size the pdf of normalized A_y becomes narrower at the investigated wall-normal locations. The reason is again the larger St of the bigger particles. Although the large size of these particles makes them less responsive to the turbulent motions, it can also reduce their preferential sampling and expose them to the turbulent motions with high energy, as it was also reported

by Qureshi et al. (2008). This can be the reason of large positive A_y with low frequency observed for both G-420 and Q-420 particles at $y^+ = 22$.

The pdf of A_y/a_y at $y^+ = 22$, 65, 108 and 151 is shown in Figure 7.12(a) and (b) for glass and quartz particles, respectively. Away from the wall at $y^+ = 65$, 108 and 151 the pdf of A_y/a_y does not significantly depend on the particle size, neither for glass particles nor for quartz particles. At $y^+ = 22$, however, increasing the particle size slightly narrowed the pdf of A_y/a_y for both glass and quartz particles, particularly for G-420 and Q-420. The reason can be the large positive A_y events of these particles, seen in Figure 7.13, that increase their a_y at $y^+ = 22$.

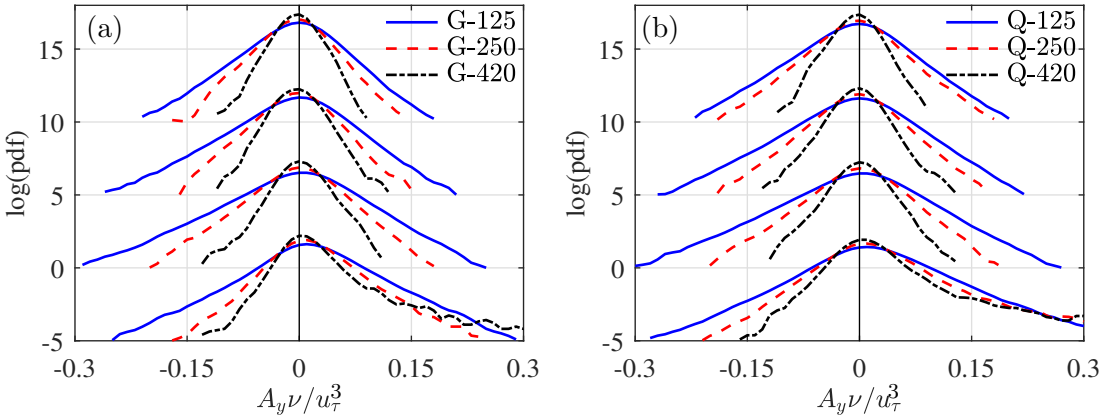

Figure 7.13: Comparison of the pdf of normalized A_y for (a) glass and (b) quartz particles at $y^+ = 22$, 65, 108, and 151, ordered from bottom to top, respectively. For clarity, the pdfs at $y^+ = 65$, 108, and 151 are shifted up by 5, 10, and 15 units of the vertical axis, respectively.

7.3.3.4 Particle-wall interaction

The effect of particle size on PWI characteristics of glass and quartz particles is investigated in this section. Similar to Section 7.3.2.4, the impact and rebound angle/velocity are estimated using the average of the associated parameter over five time steps before and after the collision, respectively. The pdf of U_i^+ for glass and quartz particles is presented in Figure 7.15, showing the larger U_i^+ for the bigger particles. This is consistent with the higher U^+ of the bigger particles in the vicinity of the wall seen in Figure 7.9.

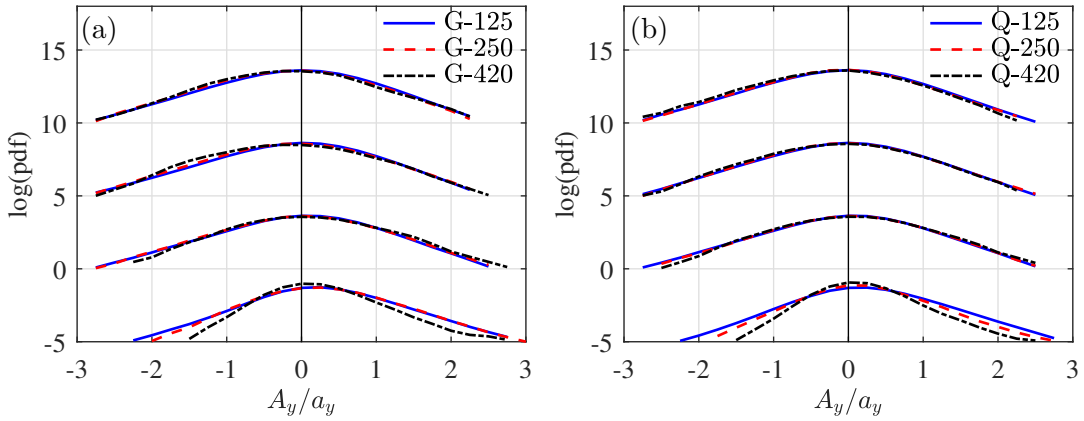

Figure 7.14: Comparison of the pdf of A_y/a_y for (a) glass and (b) quartz particles at $y^+ = 22$, 65, 108 and 151, ordered from bottom to top, respectively. For clarity, the pdfs at $y^+ = 65$, 108 and 151 are shifted up by 5, 10, and 15 units of the vertical axis, respectively.

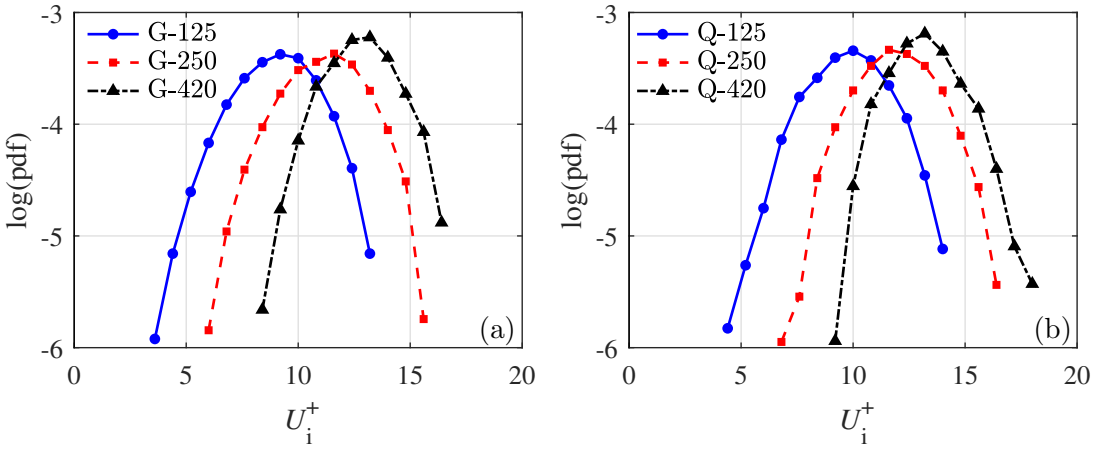

Figure 7.15: Comparison of the pdf of U_i^+ for (a) glass and (b) quartz particles with different sizes.

Figure 7.16 presents the pdf of V_i^+ for glass and quartz particles. The pdf of V_i^+ of G-125 and G-250 are approximately equal for $V_i^+ > -1$. For $V_i^+ < -1$ the pdf of V_i^+ of G-250 becomes slightly larger, showing the higher frequency of PWI with large V_i^+ for these particles. The pdf of G-420 particles is slightly shifted toward the larger V_i^+ magnitudes, again showing the increment of the frequency of PWI with larger V_i^+. The reason can be the larger settling velocity of the bigger particles. Increasing the size of the quartz particle shows a similar effect on their pdf of V_i^+.

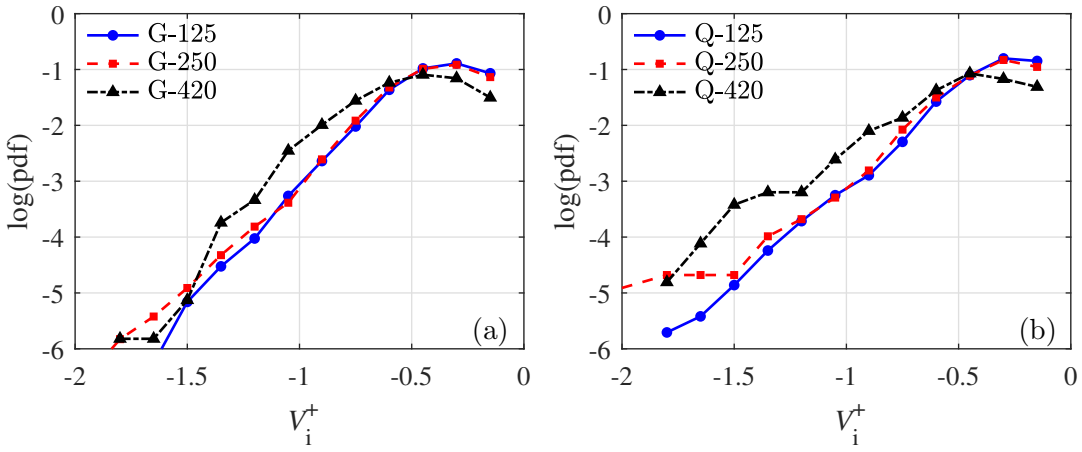

Figure 7.16: Comparison of the pdf of V_i^+ for (a) glass and (b) quartz particles with different sizes.

Figure 7.17 indicates the $\langle e_U \rangle$ as a function of θ_i for glass and quartz particles. As expected, increasing the magnitude of θ_i decreases $\langle e_U \rangle$ for all the investigated particle types. Increasing the size of particles increases the $\langle e_U \rangle$ for both glass and quartz particles, meaning that bigger particles lose smaller streamwise kinetic energy when they collide with the wall. This can be another reason for the higher U^+ of larger particles in the vicinity of the wall, as seen in Figure 7.9.

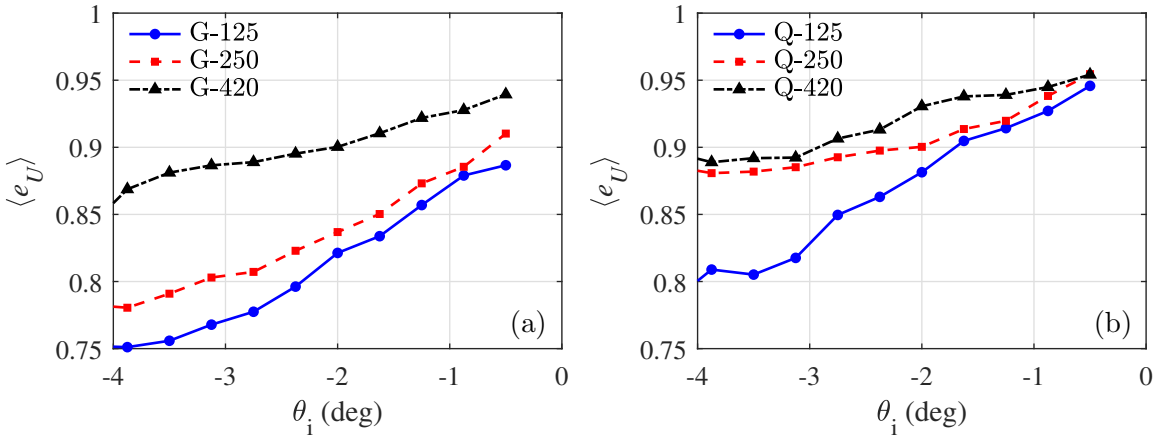

Figure 7.17: Comparison of the $\langle e_U \rangle$ of (a) glass and (b) quartz particles with different sizes.

The $\langle e_V \rangle$ of glass and quartz particles that collide with the wall is presented in Figure

7.18 as a function of θ_i. Increasing θ_i decreases $\langle e_V \rangle$ for both glass and quartz particles. The bigger particles have smaller $\langle e_V \rangle$ at almost all the investigated θ_i for both glass and quartz particles, indicating that these particles transfer larger momentum to the wall and apply a stronger impact force to it in the wall-normal direction when they collide with the wall.

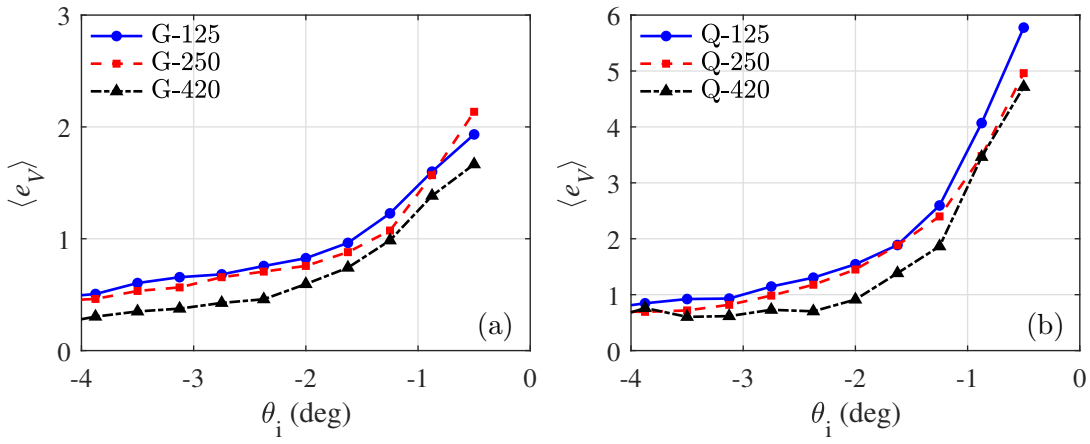

Figure 7.18: Comparison of the $\langle e_V \rangle$ of (a) glass and (b) quartz particles with different sizes.

7.4 Summary and conclusion

In this chapter, the near-wall motion of spherical and non-spherical particles was investigated using the 2D-LPT measurement system with backlight illumination. The experiments were performed at $Re_\tau = 770$ and $C_v = 0.01\%$. The near-wall motion of spherical and non-spherical particles were compared by analyzing the differences between the number density, velocity and acceleration statistics, and PWI characteristics of G-250 and Q-250 particles. Results showed that the number density of Q-250 particles was larger than G-250 particles close to the wall and smaller away from it. The Q-250 particles also had a larger U^+ next to the wall at $y^+ = 13$ due to their larger concentration in the region and the lower energy loss in the streamwise direction during their interaction with the wall. The analyzes of velocity statistics of particles showed that the streamwise and wall-normal fluctuation of Q-250 par-

ticles were slightly smaller than the spherical particles close to the wall at $y^+ < 150$. The A_x^+ of G-250 and G-250 particles were similar away from the wall at $y^+ > 100$. Closer to the wall at $y^+ < 100$, the Q-250 particles had smaller A_x^+ than G-250 particles. The A_y^+ of G-250 and Q-250 particles were also approximately equal away from the wall. In the immediate vicinity of the wall at $y^+ = 13$, however, the A_y^+ of Q-250 particles was twice larger than G-250 particles. Investigation of particles acceleration showed that the G-250 and Q-250 particles had approximately equal pdfs of A_x/a_x and A_y/a_y at different wall-normal locations. The analyzes of the PWI characteristics of G-250 and Q-250 particles indicated that Q-250 lose less kinetic energy in the streamwise and wall-normal directions during their interaction with the wall. Investigation of the rotation of the non-spherical particles was one of the objectives of the experiments of this chapter. However, this objective was not achieved using the 2D-LPT system due to the 3D rotation of the particles.

The comparison of the number density, velocity and acceleration statistics, and PWI characteristics of particles with different sizes showed that increasing particle size had a similar effect on these parameters for both glass and quartz particles. The bigger particles had a higher number density than the smaller particles close to the wall and lower away from the wall. The U^+ of bigger particles was also higher than smaller particles near the wall and lower away from the wall. Increasing the size of particles increased their St and therefore reduced their streamwise fluctuation near the wall. The analyzes of the acceleration statistics of particles showed that bigger particles experienced smaller streamwise and wall-normal acceleration due to their larger St. However, increasing the size of particles did not affect the pdf of A_x/a_x. The pdf of A_y/a_y of particles was also independent of their size away from the wall while it became narrower in the vicinity of the wall by increasing the particle size. Investigation of the effect of particle size on the PWI characteristics showed the larger U_i^+ and smaller streamwise momentum loss for bigger particles. However, the wall-normal momentum loss of the bigger particles was larger than the smaller particles during their interaction with the wall.

Chapter 8

Near-wall motion of spherical particles in a drag-reduced non-Newtonian turbulent channel flow

8.1 Introduction

Polymers with large molecular weight are well known to be effective in reducing drag and pumping power in unladen turbulent liquid flows (Virk et al., 1970; Luchik and Tiederman, 1988; Warholic et al., 1999). However, the effect of polymer drag reducers on the kinematics of particles in non-Newtonian turbulent flows with viscoelastic properties is still an open question.

Previous studies of particle motion in non-Newtonian flows have mostly investigated individual particles released in quiescent fluids or laminar flows at small Reynolds numbers (D'Avino and Maffettone, 2015; McKinley, 2002; Chhabra, 2006; Mishra S, 2012; Li et al., 2015). The viscoelastic properties of the fluid were typically characterized in terms of Deborah number (De, the ratio of fluid relaxation time to the flow time-scale) and Weissenberg number (We) which is the ratio of the elastic forces to the viscous forces of the fluid (D'Avino and Maffettone, 2015). In general, the influence of these parameters on the kinematics and dynamics of particles was investigated based on the terminal settling velocity, St, translation, rotation, and lift and drag force of individual solid particles at low Re.

In the case of non-Newtonian flows with a large number of suspended particles, previous investigations have mostly focused on the distribution of particles in terms of their migration, alignment, and clustering in the low Re regime, where inertia is negligible and fluid elasticity is dominant (D'Avino and Maffettone, 2015). At low Re channel flows, Karnis and Mason (1966) reported particle migration toward the centerline for viscoelastic fluids with constant viscosity while Gauthier et al. (1971) reported particle migration toward the walls for shear-thinning fluids. The alignment of particles at the channel centreline (known as "focusing") has been observed in microchannels at $0 < Re < 1$ and $0 < We < 250$ (Yang et al., 2011; Kang et al., 2013; Seo et al., 2014), and even at higher Re of about 2000 for $We \approx 200$ (Lim et al., 2014). In spite of the great number of studies on particle motion in laminar and transitional non-Newtonian flows, the motion of particles in turbulent non-Newtonian flows with stronger inertial effects has not been investigated yet.

In Newtonian turbulent wall flows, the interaction of near-wall turbulent structures and particles significantly affects the kinematics, dispersion, and clustering of the particles. Due to gravity, inertial particles tend to proceed toward the lower wall in horizontal flows. The particles move from the outer layer into the inner layer where they are either farther transported toward the wall by sweep motions (Sumer and Deigaard, 1981; Marchioli and Soldati, 2002), or sent back to the outer layer by ejection motions of the liquid phase (Marchioli and Soldati, 2002; Kiger and Pan, 2002; Soldati and Marchioli, 2009). The particles that are carried by the sweep motions toward the wall may collide with the wall and bounce off to higher layers if they have enough momentum (Soldati, 2005); otherwise, they get trapped in low-speed streaks (Pedinotti et al., 1992; Kaftori et al., 1995a,b). Inertial particles that are smaller than the Kolmogorov scale typically do not concentrate in the high-speed streaks because of the rotational motion of these turbulent structures (Pedinotti et al., 1992). The small particles often cluster in low-speed streaks and remain there until they are propelled away from the wall by strong enough ejection motions (Marchioli and Soldati, 2002; Soldati, 2005). Smaller particles with small St usually stay in the vicinity of the wall for a shorter time since they can be transported away from the wall by weaker ejection motions (Soldati,

2005). Therefore, in turbulent Newtonian flows, sweep and ejection motions are the main turbulent structures which disperse the particles, depending on their size and St.

In a non-Newtonian flow, the near-wall turbulent structures are modified due to the fluid's rheology (Warholic et al., 2001). The addition of drag-reducing polymers decreases turbulent kinetic energy and Reynolds shear stress (Warholic et al., 1999), thickens and stabilizes the low/high-speed streaks (White et al., 2004; White and Mungal, 2008), and increases their spanwise spacing (White et al., 2004). Polymer additives also attenuate the near-wall quasi-streamwise vortices, reduce their number (Dubief et al., 2004; Kim et al., 2007; White and Mungal, 2008), and make them longer (Kim et al., 2007). The ejection and sweep motions also become weaker and less frequent (Kim et al., 2007; Corredor et al., 2015). In general, this suppression of turbulent structures disrupts the regeneration cycle of wall turbulence (Karniadakis and Choi, 2003; Dubief et al., 2004). Since fluid forces have a significant effect on kinematics and dispersion of suspended particles, changing turbulent structures by polymer additives is expected to also affect particles motion.

In light of the literature reviewed, the objective of the investigations in this chapter is to experimentally characterize the kinematics of spherical particles and their dispersion in a drag-reduced turbulent channel flow of a polymer solution. To achieve this objective, trajectories of particles is determined using 2D-LPT, discussed in Section 4.1 along with its uncertainty, in the turbulent flow of water (Newtonian) and the polymer solution (non-Newtonian). The particle trajectories are used to investigate the influence of the polymer additive on wall-normal distribution, streamwise and wall-normal velocities, Reynolds stresses, and the transport angle of the particles in the near-wall region. The influence of the polymer additive on the ejection and sweep motions of the particles was investigated by applying a quadrant analysis.

The flow facility used for performing the experiments of this chapter was explained in Section 3.1. The experimental design of this chapter is presented in Section 8.2. The accuracy of the measurement system is evaluated in Section 8.3.1 by comparing the measurements in the unladen Newtonian flow with the literature. The motion of the particles

in Newtonian and non-Newtonian flows are investigated in Section 8.3.2.

8.2 Experimental design

Four turbulent flows were investigated in the experiments of this chapter: unladen water flow (Newtonian); unladen polymeric flow (non-Newtonian); particle-laden water flow (Newtonian); and particle-laden polymeric flow (non-Newtonian). All the experiments were performed at a constant temperature of 25° and a constant mass flow rate of 3.66 kg/s equivalent to Newtonian Re_{H0} of 34,300, based on the channel height, bulk velocity across the channel (U_b = 2.04 m/s), and viscosity of water. For the non-Newtonian experiments, a 90 ppm solution of SF was prepared as discussed in Section 3.2. Based on the pressure measurement at the mass flow rate of 3.66 kg/s, the average $DR\%$ was ≈66% in 30 minutes, which is considered as high drag reduction regime (Warholic et al., 1999), and its degradation was ≈3.7%.

The average dynamic viscosity at the wall (μ_w) in turbulent flows can be estimated as $\mu_w = \tau_w/\dot{\gamma}_w$, where τ_w and $\dot{\gamma}_w$ are the average shear stress and shear rate at the wall, respectively. In this chapter, the subscript 'w' refers to parameters estimated at the wall. The $\dot{\gamma}_w$ of the polymeric flow was determined from the wall-normal velocity profile measured by 2D-LPT, as detailed later in Section 8.3.1. The wall shear stress associated with this $\dot{\gamma}_w$ was determined based on the Ostwald-de Waele model. Having $\dot{\gamma}_w$ and τ_w, the associated kinematic viscosity at the wall (ν_w) was estimated for the polymeric flow and is shown in Table 8.1. The viscosity of a power-law fluid in a channel flow is at its minimum at the wall where average $\dot{\gamma}$ is maximum, and at its maximum at the centerline of the channel, where average $\dot{\gamma}$ is a minimum. The friction velocity (u_τ) and wall unit (λ) were also estimated from the 2D-LPT measurement and are presented in Table 8.1. The time scale of turbulent flows was estimated at the wall as $t_\tau = \nu_w/u_\tau^2$ and the friction Reynolds number was determined as $Re_\tau = u_\tau H/\nu_w$.

The particle-laden flows consisted of G-250 particles at a volumetric concentration of 0.05% suspended in water (Newtonian) and in the 90 ppm SF solution (non-Newtonian).

Fluid	$\dot{\gamma}_w$ $1/s$	ν_w $\times 10^6 m^2 s$	u_τ m/s	λ μm	t_τ μs	Re_τ
water	11500	0.893	0.101	8.9	89	840
SF solution	2260	1.330	0.054	24.3	443	309

Table 8.1: The inner scaling of the unladen turbulent water and polymeric flows. The shear rate at the wall and inner scaling were calculated using the mean velocity profiles from 2D-LPT.

The properties of the particles used in the particle-laden experiments of this chapter are presented in Table 8.2. The V_t of particles suspended in the Newtonian flow was determined using Equation 2.11. For the Newtonian flow, ν does not depend on $\dot{\gamma}$. Therefore, the Re_{pt} and t_p presented in Table 8.2 for the particle-laden water flow are constant in different wall-normal locations (y). The St^+ of these particles is also presented in the table.

The drag coefficient of a spherical particle in a power-law fluid is typically estimated based on its Reynolds number in that fluid which is defined as (Chhabra and Richardson, 1999)

$$Re_{pl} = \frac{\rho_f V_t^{(2-n)} d_p^n}{K}, \tag{8.1}$$

where K and n are the flow consistency and behavior indices of the power-law fluid, respectively. Based on the method presented by (Chhabra and Richardson, 1999), the V_t of particles in the SF solution was 0.0158 m/s and their Re_{pl} was 1.28. However, this method does not consider fluid elasticity and may overestimate V_t (Arnipally and Kuru, 2017). To determine V_t of the particles in the SF solution, a particle was released in the middle of a $8 \times 8 \times 8$ cm^3 container filled with the 90 ppm SF solution. The particle's velocity was measured in a 5×5 mm^2 field-of-view, which was 20 mm away from the bottom of the container. The images were recorded at digital resolution of 2.95 μm/pix at 2 kHz frequency. The uncertainty was 6×10^{-4} m/s based on 0.1 pix uncertainty in detection of particle location. A negligible variation of particle's velocity was observed within the field-of-view, which indicates that the particle has reached its terminal settling velocity. The average V_t

from five tests was 0.011 m/s with a standard deviation of 0.002 m/s, which resulted in Re_{pt} of 2.27 based on μ_w. These values of V_t and Re_{pt} are presented in Table 8.2 along with the associated t_p and St^+ for particles in the polymeric flow based on μ_w.

The Rouse number for the particles in water ($\kappa = 0.41$) and polymeric flows ($\kappa = 0.08$) is also presented in Table 8.2. The particles in the polymeric flow have a larger Ro than in water flow, showing reduction of turbulence contribution to particle suspension. The pressure measurement in the particle-laden polymeric flow experiment showed $DR\%$ of about 61% which is 5% less than the unladen polymeric flow.

Fluid	V_t m/s	Re_{pt}	t_p ms	St^+	Ro
water	0.070	17.78	3.40	39.1	1.70
SF solution	0.011	2.27	4.05	9.1	2.34

Table 8.2: Properties of the G-250 particles in the particle-laden experiments, calculated based on the d_{50} of the particles. The Re_{pt}, t_p, and St^+ for the SF solution are determined based on the viscosity at the wall.

8.3 Results and discussion

In this section, first, the uncertainty of the 2D-LPT is evaluated by comparing its results in water with the DNS of Hoyas and Jiménez (2008) at Re_τ= 934. Next, the velocity field and turbulence statistics of the unladen water and polymeric flows are compared. Finally, the average velocity and Reynolds stresses of the particles in water and polymeric flows are scrutinized. The wall-normal distance, averaged velocities, and the Reynolds stresses presented in this section are normalized by either the inner scaling of the unladen water flow (presented with subscript "0") or inner scaling of the corresponding unladen counterpart (presented without subscript "0").

8.3.1 Unladen turbulent flow

The velocity statistics of unladen water and polymeric flows are presented in this section. The bin size for averaging 2D-LPT data of the unladen flows is equal to λ of unladen water flow ($\approx 0.001H$) in the y-direction. The average streamwise velocity, $\langle U \rangle$, for water at $Re_\tau = 840$, polymeric flow (at the same mass flow rate), and the DNS of Hoyas and Jiménez (2008) at $Re_\tau = 934$ are compared in Figure 8.1 in a semi-logarithmic presentation. The $\langle U \rangle$ profiles for water and polymeric flows are normalized by their corresponding friction velocities, $U^+ = \langle U \rangle / u_\tau$, and shown as functions of wall-normal distance also normalized by the corresponding wall units $y^+ = y/\lambda$. The logarithmic law of the wall with $\kappa = 0.4$ and $B = 5.2$ is also presented in this figure. The 2D-LPT measurement of U^+ for water agrees with the DNS from $y^+ \approx 4$ up to the border of the field of view at $y^+ \approx 550$ in the log-layer, which shows the accuracy of the 2D-LPT. The overlap with the log law also indicates the fully developed state of the turbulent channel flow (Bailey et al., 2014).

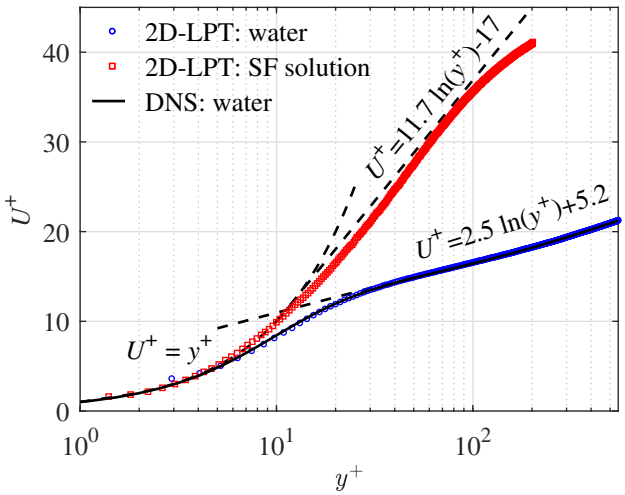

Figure 8.1: Effect of the SF solution on the U^+ profile as a function of y^+. The dashed-lines show $U^+ = y^+$, the log-law for Newtonian fluid flows, $U^+ = 2.5 \ln(y^+) + 5.5$, and Virk's asymptote (Virk et al., 1970), $U^+ = 11.7 \ln(y^+) - 17$. The solid line shows the DNS of Hoyas and Jiménez (2008) at $Re_\tau = 934$ for water.

The U^+ profile of the polymeric flow follows the $U^+ = y^+$ line up to $y^+ \approx 10$. Beyond this location, the profile follows Virk's asymptote (Virk et al., 1970), $U^+ = 11.7 \ln(y^+) - 17$, which shows that the polymeric flow is at the maximum drag reduction regime. The $DR\%$

of the polymer solution can also be calculated as $DR\% = (1-\tau_{\mathrm{w}}^{\mathrm{p}}/\tau_{\mathrm{w}}^{\mathrm{w}})\times 100$, where $\tau_{\mathrm{w}}^{\mathrm{w}}$ and $\tau_{\mathrm{w}}^{\mathrm{p}}$ are the shear stresses of water and the polymeric flows at the wall, estimated from their $\langle U\rangle$ profiles, respectively. Based on the $\dot{\gamma}_{\mathrm{w}}$ and ν_{w} of water and the polymeric flows (see Table 8.1), the $\tau_{\mathrm{w}}^{\mathrm{w}}$ and $\tau_{\mathrm{w}}^{\mathrm{p}}$ are about 10 and 3 Pa, respectively. Therefore, the $DR\%$ of the SF solution based on 2D-LPT is about 70%, which is close to $DR\% = 66\%$ obtained from the pressure drop measurement. The polymeric flow profile deviates from the Virk's asymptote at $y^+ \approx 110$ and follows a log law region, which is called "Newtonian plug" (Procaccia et al., 2008). This shows that the buffer layer, the region between viscous sublayer and log-layer, which starts at $y^+ \approx 10$ ($y/H \approx 0.032$), ends at $y^+ \approx 110$ ($y/H \approx 0.356$) for the polymeric flow. The trend of polymeric flow profile in Figure 8.1 is consistent with the trend of semi-logarithmic U^+-y^+ profile for a polymer solution with $DR\%$ of 69% presented by Warholic et al. (1999).

The thickness of the viscous sublayer, the region where $U^+ = y^+$, is about $0.006H$ ($y^+ \approx 5$) in water flow, increasing to $0.032H$ ($y^+ \approx 10$) in the polymeric flow. The buffer layer thickness also increases from about $0.017H$ ($\Delta y^+ \approx 15$) in water flow to $0.324H$ ($\Delta y^+ \approx 100$) in the polymeric flow. The polymer additive also reduces u_τ (see Table 8.1) and $\langle U\rangle$ near the wall and increases $\langle U\rangle$ away from the wall. The reduction of u_τ and increment of $\langle U\rangle$ in the log region shifts the log-layer profile upward with respect to water flow, as seen in Figure 8.1.

The streamwise, wall-normal, and shear Reynolds stresses ($\langle u^2\rangle$, $\langle v^2\rangle$, and $\langle uv\rangle$, respectively) in unladen Newtonian and non-Newtonian flows are presented in Figure 8.2(a). The Reynolds stresses for both flows are normalized by friction velocity of the unladen water flow ($u_{\tau 0}$). The wall-normal distance is non-dimensionalized by the wall units of water (λ_0) and polymeric flow (λ_1) and presented as y_0^+ and y_1^+ at the lower and upper horizontal axes, respectively. The Reynolds stresses for water at $Re_\tau = 840$ are also compared with the DNS of Newtonian channel flow at $Re_\tau = 934$ by Hoyas and Jiménez (2008). The $\langle u^2\rangle/u_{\tau 0}^2$ peak for water from 2D-LPT is about 2% lower than the DNS. The maximum magnitudes of $\langle v^2\rangle/u_{\tau 0}^2$ and $\langle uv\rangle/u_{\tau 0}^2$ are also about 11% and 8% less than the DNS. These differences

are associated with the lower Re_τ of the experiment, which causes a thicker inner layer and slightly lower Reynolds stresses.

As seen in Figure 8.2(a), the maximum value of $\langle u^2 \rangle$ of the polymeric flow is about 50% less than that of water. The $\langle v^2 \rangle$ and $\langle uv \rangle$ profiles of the polymeric flow, which almost overlap with each other in Figure 8.2(a), are significantly less than water (almost zero in the measurement domain). The effect of SF solution on the Reynolds stresses is consistent with the results presented by Warholic et al. (1999) at a high drag reduction regime ($DR\% > 35\%$). At $DR\%$ of 69%, they observed about 40, 85, and 95% reduction in maximum magnitudes of $\langle u^2 \rangle$, $\langle v^2 \rangle$, and $\langle uv \rangle$ profiles, respectively. The measurement also shows that adding the SF polymer to the flow shifts the $\langle u^2 \rangle$ peak away from the wall; the $\langle u^2 \rangle$ profile peaks at $y_0^+ \approx 15$ ($y/H = 0.017$) in water and at $y_0^+ \approx 115$ ($y/H = 0.133$) in the polymeric flow. This is due to a thicker viscous sublayer and buffer layer in the channel flow of the SF solution (Warholic et al., 1999, 2001; Mohammadtabar et al., 2017).

The Reynolds stresses of unladen Newtonian and non-Newtonian flows are also normalized by their corresponding inner scaling and presented in Figure 8.2(b). The polymeric flow has a larger $\langle u^2 \rangle / u_\tau^2$ and smaller $\langle v^2 \rangle / u_\tau^2$ and $\langle uv \rangle / u_\tau^2$ than water, which has a similar flow rate but a higher Re_τ of 840. This trend is consistent with the experimental results of Warholic et al. (2001) and DNS results of Dubief et al. (2005) at a high drag reduction regime. It is also observed that Reynolds stresses of the polymeric flow at $Re_\tau = 309$ are significantly different from those of DNS of Newtonian turbulent channel flow at similar Re_τ of 298 from Iwamoto et al. (2002). This shows that the change in Reynolds stresses of the polymeric flow with respect to the water is not simply due to the reduction of Re_τ.

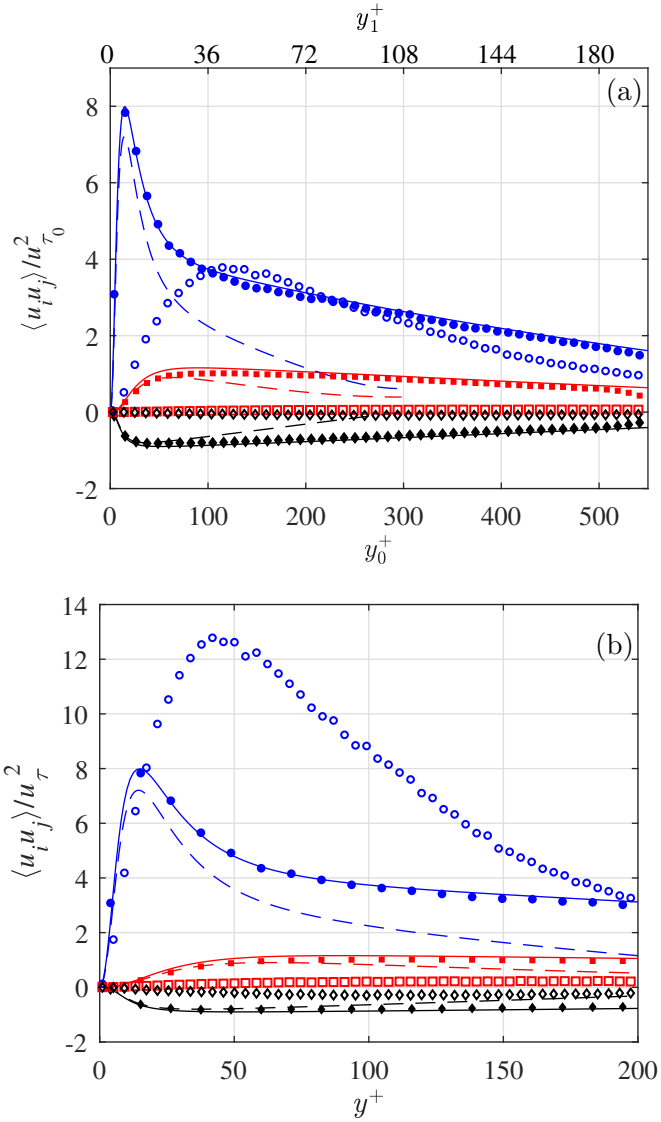

Figure 8.2: Profiles of $\langle u^2 \rangle$ (blue circles), $\langle v^2 \rangle$ (red squares), and $\langle uv \rangle$ (black diamonds) for the Newtonian (filled symbols) and non-Newtonian (open symbols) flows. The profiles are normalized by (a) the inner scaling of water flow and (b) their corresponding inner scaling. Lines show the DNS of Newtonian channel flow at Re_τ=934 by Hoyas and Jiménez (2008) (solid lines) and at Re_τ=298 by Iwamoto et al. (2002) (dashed lines). Only one of every ten experimental data points is presented for clarity.

8.3.2 Particle-laden turbulent flow

The velocity field and the motion of the particles in water and the polymeric flows at a volumetric concentration of 0.05% are investigated in this section. The wall-normal location

and velocity statistics are normalized by the inner scaling of the unladen water flow.

8.3.2.1 Near-wall number density distribution of particles

The number density distribution of the particles in the near-wall region of $y < 0.64H$ for the water and polymeric flows is presented in Figure 8.3. The averaging is carried out using a bin size of 0.5 mm, and the profiles are normalized by dividing the number of particles in each bin (N) by the average number of particles per bin for water ($\bar{N}_0$). Normalization using a common value is chosen here to show the effect of the SF solution on the near-wall particle concentration. In this analysis, all the particle trajectories are considered without any limitation on trajectory length. As Figure 8.3 shows, $N/\bar{N}_0$ increases with reducing y_0^+. This shows that the particles gradually settle in water due to gravity, although turbulence dispersion counteracts and tries to suspend the particles. Since the number of particles in the measurement domain for water is more than the number of particles in the polymeric flow, $N/\bar{N}_0$ is less than one across the measurement domain for the polymeric flow. The suspension of the particles by turbulence in the polymeric flow is expected to be smaller than water flow due to the increase of R (see Table 8.2) and the negligible $\langle v^2 \rangle$ and $\langle uv \rangle$, as observed in Figure 8.2. However, a significant reduction of $N/\bar{N}_0$ is observed in the near-wall region, and the distribution of the particles is more uniform. For particles in the polymeric flow, an increase of $N/\bar{N}_0$ is only observed at $y_1^+ < 36$ ($y < 0.1H$). The settling velocity of the particles in the polymeric flow is smaller than in the water flow due to the larger μ of the polymer solution. Therefore, based on settling velocity, the particles in the polymeric flow need a longer time and streamwise distance to accumulate in the vicinity of the wall compared with the particles in water flow. It is also important to note that the settling velocity in the polymeric flow depends on local viscosity, which is a function of $\dot{\gamma}$. In the polymeric flow, particles settling velocity decreases with an increase of y; therefore, the larger near-wall settling velocity has slightly accumulated the particles at $y_0^+ < 100$. This observation also shows that, in polymer drag reduced flows, although turbulence dispersion is small, inertial particles may not accumulate in the near-wall region due to their smaller

settling velocity when they are away from the wall. In addition, using DNS, Huang et al. (1997) showed that the inertial particles in viscoelastic fluids tend to move away from the wall. They showed that when $\beta = d_p/(2H)$ is small (β was 0.025 in their study while it is 0.018 in the current study) particles tend to move toward the region with lower $\dot{\gamma}$ due to normal stresses of the viscoelastic fluid, which are induced by the gradient of the velocity profile.

The important observation here is the small concentration of the particles near the lower wall of the channel, which reduces the probability for the collision of the particles with the wall in the polymeric flow. This suggests a smaller wear rate and energy loss in particle-laden flows with drag-reducing polymers. To the authors' knowledge, the reduction of particle concentration in the near-wall region of viscoelastic flows, and their migration toward the center of channel, were only reported in microchannels, and for laminar or transitional flows (Yang et al., 2011; Kang et al., 2013; Lim et al., 2014; Huang et al., 1997; Di Carlo et al., 2007; Leshansky et al., 2007; D'Avino et al., 2012; Del Giudice et al., 2013; Ciftlik et al., 2013).

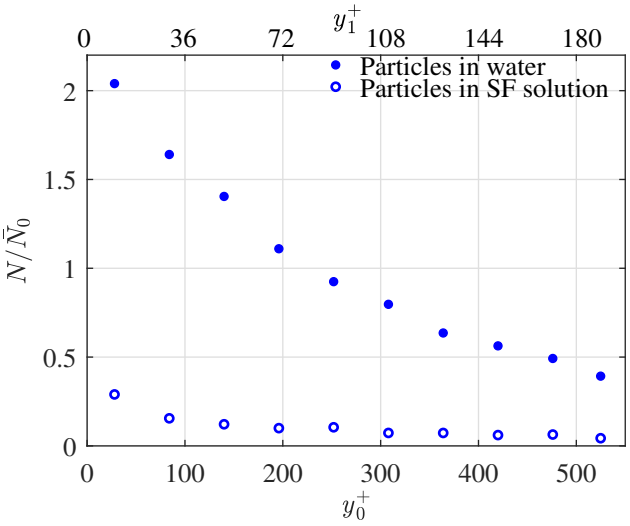

Figure 8.3: The effect of SF solution on the number density distribution of the particles.

8.3.2.2 Average streamwise velocity of particles

The profiles of $\langle U \rangle$ for the fluid and particles in water and polymeric flows are normalized by $u_{\tau 0}$, and presented as $U_0^+ = \langle U \rangle / u_{\tau 0}$ in Figure 8.4. For the first data point, which corresponds to an averaging bin from the wall up to $y^+ = 28.8$, the velocity of particles in water is larger than the velocity of the unladen water. This larger velocity of the particles at the wall is because the no-slip boundary condition does not apply to them; particles can slide or roll on the wall. In the log layer ($y_0^+ > 30$), the U_0^+ of the particles is less than the unladen water flow, which is due to the higher inertia of the particles Shokri et al. (2017); Ahmadi et al. (2019).

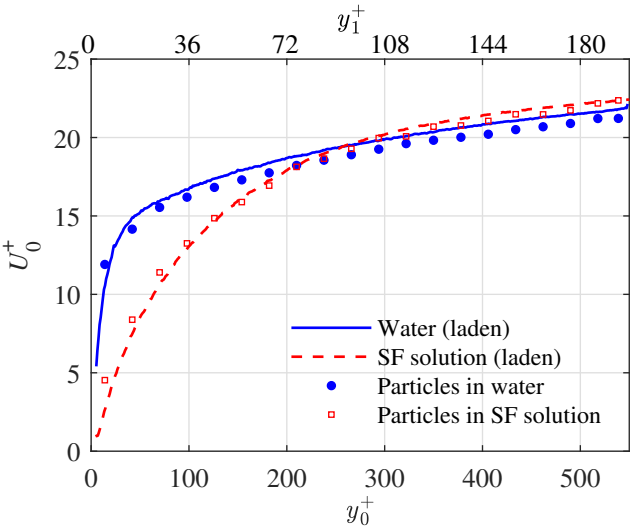

Figure 8.4: Effect of the polymeric flow on the average streamwise velocity profile of the particles. The lines show the normalized average streamwise velocity of the fluid in the particle-laden flows.

The U_0^+ profile of the unladen polymer solution is lower than U_0^+ of water at $y_0^+ < 300$ ($y/H < 0.348$). This wall-normal range extends to the border of the buffer layer for the polymeric flow. Since the particles absorb their kinematic energy from the carrier phase, the particles also have a smaller velocity in this region. The smaller velocity of particles near the wall reduces the momentum exchange and the tangential force that is exerted on the wall during their collision with the wall. In the viscous sublayer, and most of the buffer layer of the polymeric flow, the velocity of the particles is slightly larger than its unladen

counterpart.

8.3.2.3 Reynolds stresses of particles

The effect of the polymer solution on the Reynolds stresses of the particles is shown in Figure 8.5, obtained by averaging PTV data using a 0.5 mm bin size. The $\langle u^2 \rangle$ profile of the particles in water is maximum at the first bin ($y_0^+ = 14.4$), where the maximum value of $\langle u^2 \rangle$ of the unladen water flow was observed in Figure 8.2. As Figure 8.5 shows, the effect of the polymer solution on $\langle u^2 \rangle$ is smaller than its effect on $\langle v^2 \rangle$ and $\langle uv \rangle$. This is similar to the effect of the SF solution on the $\langle v^2 \rangle$ and $\langle uv \rangle$ profiles of the unladen flow (see Figure 8.2). The reduction of $\langle uv \rangle$ of the particles shows weaker sweep and ejection motions, which are the major mechanisms for wall-normal dispersion of the particles Kiger and Pan (2002). Therefore, the trajectory of the particles in the polymeric flow is relatively aligned in the streamwise direction. This is observed in the sample particle trajectories in polymer solution and water in Figure 4.3; the trajectories of the particles in the polymer solution has a smaller displacement in the wall-normal direction. This is expected to reduce the impact angle and collision probability of the particles with the channel wall.

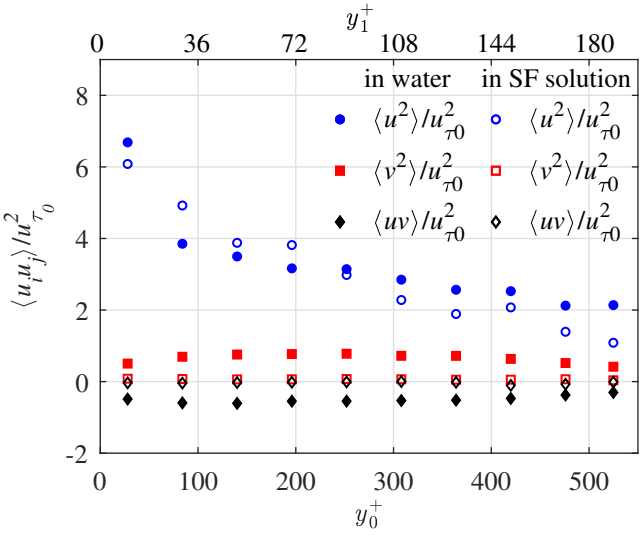

Figure 8.5: Reynolds stresses of the particles in the water and polymeric flow.

8.3.2.4 Near-wall motion of particles

The effect of the polymeric flow on the motion of the inertial particles is investigated here by applying conditional averaging on their instantaneous wall-normal velocity (V). In the discussion, we refer to the particles moving toward the bottom wall ($V < 0$) as downward-moving particles, and the particles moving toward the center of the channel ($V > 0$) as upward-moving particles. The wall-normal velocity of the particles is conditionally averaged based on the V sign (i.e. their motion toward or away from the wall) for the water and polymeric flow. The result is normalized by $u_{\tau 0}$ ($V_0^+ = \langle V \rangle / u_{\tau 0}$) and presented in Figure 8.6. The V_0^+ of the particles in the polymer solution, in terms of both upward and downward motions, is significantly smaller than their velocity in water. The SF solution reduces V_0^+ of the particles with downward motion at $y_0^+ = 14.4$ by about 80%, which is also expected to reduce the wall-collision probability.

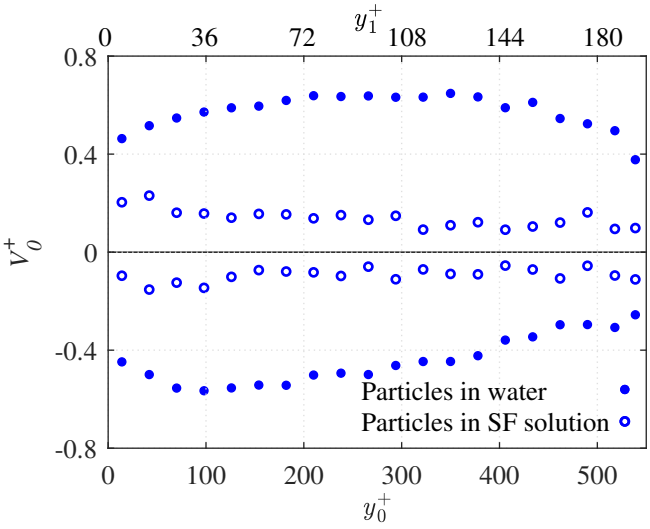

Figure 8.6: Effect of the SF solution on V_0^+ of the particles with upward and downward motions.

The average of the velocity vector magnitude in $x - y$ plane ($|\mathbf{U}_p|$) for the upward and downward moving particles is presented in Figure 8.7 to investigate their momentum. It is observed that the momentum of the particles at $y_0^+ = 14.4$ is reduced by about 60% in the polymeric flow compared with water flow. The reduction of the momentum of particles

near the wall reduces the collision force upon impact with the wall. In water flow, the $|\mathbf{U}_p|$ of downward moving particles is greater than that of the upward moving particles by about $1.2u_{\tau 0}$. This is because the downward moving particles move from a region with a larger $\langle U \rangle$ to a region with a smaller $\langle U \rangle$, transporting the momentum toward the wall. The difference between $|\mathbf{U}_p|$ of downward and upward moving particles also exists in the polymeric flow but it is smaller than the water flow. This is associated with the smaller wall-normal velocity and therefore their smaller wall-normal transport in the polymeric flow.

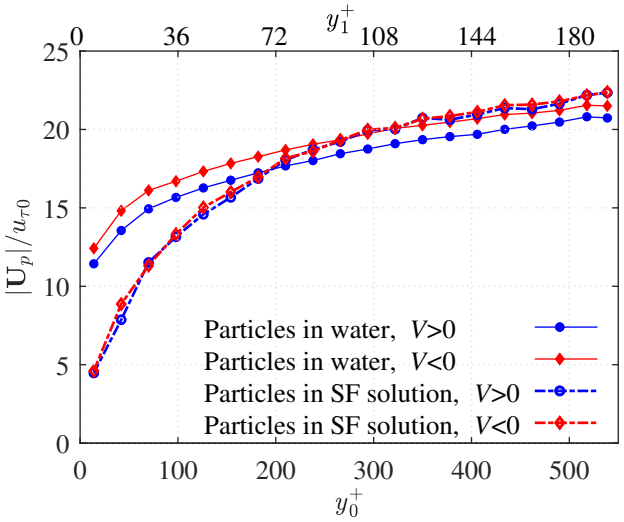

Figure 8.7: The mean velocity of the particles with upward or downward motion in water and polymeric flows.

The motion of the particles is also characterized here using their trajectory angle, $\theta = \tan^{-1}(V/U)$. A downward moving particle has $\theta < 0$ ($V < 0$, $U > 0$) and an upward moving particle has $\theta > 0$ ($V > 0$, $U > 0$). The trajectory angle for the particles is useful for modeling wall-collision and evaluation of numerical simulations of two-phase turbulent channel flows. The trajectory angles of the particles in water and polymeric flows are conditionally averaged based on the sign of V and are presented in Figure 8.8. This figure shows that the average trajectory angle of the particles, $\langle \theta \rangle$, for the downward and upward moving particles in water flow is $\langle \theta \rangle = -2.3°$ and $2.3°$ in the immediate vicinity of the wall at $y_0^+ = 14.4$. In the polymeric flow, these angles are smaller and equal to $-1.2°$ and $2.6°$ for downward and upward particles, respectively. In general, the trajectory angle

of the particles in the polymeric flow is significantly smaller than in the water except for the upward particles at $y_0^+ \approx 14.4$. The smaller trajectory angle for the particles in the polymeric flow is consistent with the previous observation of small wall-normal velocity in Figure 8.5 and Figure 8.6. The $\langle\theta\rangle$ of downward particles at $y_0^+ \approx 14.4$ is reduced by about 45% in the polymeric flow compared with water. This is important in terms of particle-wall collision; the reduction of the impact angle of the particles with the wall, along with the reduction of their momentum (see Figure 8.7) can potentially reduce pipe wear rate in two-phase systems.

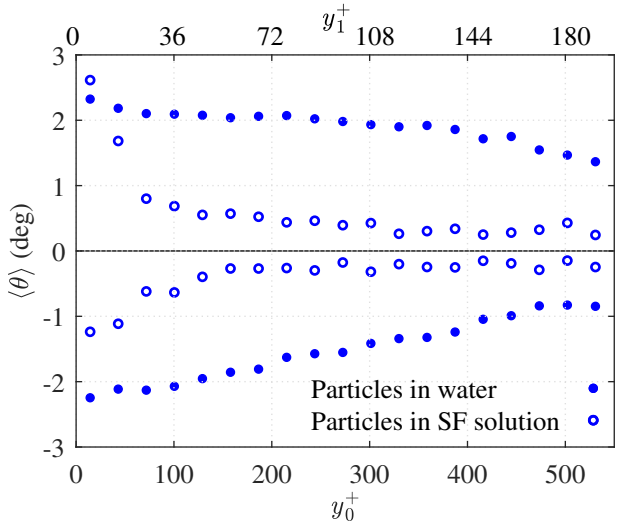

Figure 8.8: The mean trajectory angle of the particles with upward or downward motion.

Quadrant analysis of turbulent fluctuations is carried out to investigate the effect of the SF solution on the ejection and sweep motions of the particles (Wallace, 2016). The joint probability density function of velocity fluctuations for the unladen and laden flows of water and SF solution in three different wall-normal locations is presented in Figure 8.9. The selected locations include $y_0^+ \approx 14.4$, which is at the center of the first bin immediately after the wall, $y_0^+ \approx 100$, the location of maximum $\langle u^2\rangle$ for the unladen SF solution, and $y_0^+ \approx 530$, which is the farthest available data point from the lower channel wall. Each jpdf has four quadrants associated with four different turbulent motions: upward interaction (quadrant 1; $u > 0$, $v > 0$); ejection (quadrant 2; $u < 0$, $v > 0$); downward interaction

(quadrant 3; $u < 0$, $v < 0$); and sweep (quadrant 4; $u > 0$, $v < 0$) Wallace et al. (1972). The total jpdf percentage of each quadrant is also indicated at the corner of each quadrant. In all the plots of Figure 8.9, u and v are normalized by $u_{\tau 0}$.

Comparing the results for unladen water and polymeric flows in the first and second rows of Figure 8.9 shows that the ejection and sweep motions are weaker in the polymeric flow. For example, ejection and sweep motions in the unladen water flow at $y_0^+ \approx 14.4$ (Figure 8.9(a)) are dominant compared with the other quarters and each forms 34% of the motion. However, their contribution to the polymeric flow is smaller, as seen in Figure 8.9(d); ejections form 28% and sweeps form 24% of the motions, similar to the other quadrants. There is also no evidence of strong ejection and sweep motions (large u and v) in Figure 8.9(d, e, and f).

The sweep and ejection motions also dominate the turbulent motions of the particles at $y_0^+ \approx 14.4$ and 100 (see plots (g) and (h) in Figure 8.9), which is consistent with Figure 8.9(a) and (b). However, away from the wall at $y_0^+ \approx 530$, sweep and ejection motions of the particles are weaker and the particles mostly move downward (3^{rd} and 4^{th} quadrants) due to gravity, as seen in Figure 8.9(i). The jpdf contour of the particles in the polymeric flow (4^{th} row of Figure 8.9) shows different behavior compared with the particles in water. At $y_0^+ \approx 14.4$, a large number of particles in the polymer solution have a downward motion, as seen by the greater jpdf of the 3^{rd} and 4^{th} quadrants of Figure 8.9(j). This is because the ejection motion, which is the main mechanism to suspend the particles away from the wall, is weak in the polymeric flow and the motion of particles is dominated by a downward fluctuation due to the effect of gravity. At $y_0^+ \approx 100$ and 530, the trend is opposite and more particles have $v > 0$ in Figure 8.9(k) and (l). The upward motion is associated with the normal stress of the viscoelastic fluids Huang et al. (1997). Therefore, the quadrant analysis shows that the sweep and ejections are not the major mechanisms for wall-normal dispersion of the particles in the polymeric flow.

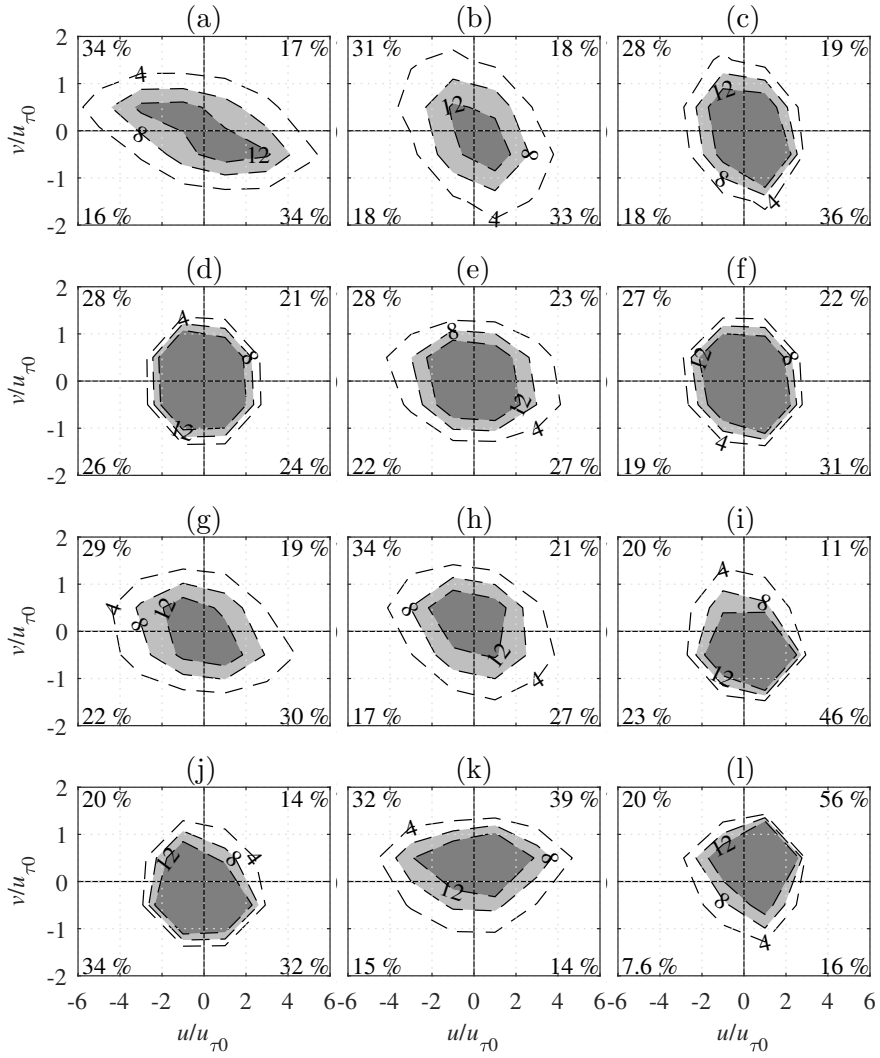

Figure 8.9: The Joint probability density function of normalized velocity fluctuations of unladen water flow (a, b, and c), unladen polymeric flow (d, e, and f), particles in water flow (g, h, and i), and particles in polymeric flow (j, k, and l). The plots in each row correspond to $y_0^+ \approx 14.4$, 100, and 530, from left to right, respectively. The number at the corners of each plot shows the percentage of turbulent motions in the associated quarter. The number on each contour shows the jpdf percentage.

8.4 Summary and conclusion

The motion of G-250 particles with a volumetric concentration of 0.05% in a turbulent flow of drag-reduced polymer solution was investigated using 2D-LPT. A 90 ppm solution of Superfloc (SF) polymer in water with about 66% drag reduction was used as the drag-reducing polymer solution. Experiments were carried out at mass flow rate of 3.66 kg/s for water and the polymer solution, which was equivalent to Reynolds number of 34,300, based on bulk velocity, the height of the channel, and the kinematic viscosity of water. Results showed that the SF solution reduced the number density of the particles and distributed them more evenly, near the channel lower wall, in the wall-normal direction. The SF solution also reduced the average streamwise velocity, $\langle U \rangle$, of the particles close to the wall and increased it away from the wall relative to the $\langle U \rangle$ profile of the particles in water flow. The addition of the polymer to the carrier phase did not change the streamwise Reynolds stress of the particles but it significantly reduced wall-normal and shear Reynolds stresses of the particles. In addition, the average wall-normal velocity of the particles reduced and their trajectory became more aligned with the streamwise direction in the polymeric flow. The momentum of the particles in the immediate vicinity of the wall in polymeric flow was about 60% smaller than in the water flow. The quadrant analysis of particles motion showed that ejection and sweep motions of the particles were attenuated in the polymeric flow and were not a major mechanism for wall-normal dispersion of the particles. The reduction of the number density, trajectory angle with respect to the wall, and the momentum of the particles near the channel wall in the polymeric flow indicate the potential of drag-reducing polymers for reducing erosion in slurry pipes.

Chapter 9

Conclusions and recommendations

The motion of inertial particles in the near-wall non-isotropic Newtonian and non-Newtonian particle-laden turbulent channel flows was experimentally studied in this thesis. In this regard, the distribution, velocity, and acceleration of particles and their interaction with turbulence, other particles, and the wall were analyzed and the effect of Re, C_v, particle size and shape were investigated. The first part of this chapter summarizes the conclusions derived from the outcomes of Chapters 5 to 8 of this thesis. The second part of this chapter offers a few recommendations for further experimental investigations required to better understand the motion of particles in turbulent flows.

9.1 Conclusion

The dynamics and wall-collision of inertial particles in non-isotropic near-wall turbulence were investigated using spherical glass particles (G-125) at a C_v of 0.03% in a turbulent channel flow at $Re_\tau = 410$. The mean acceleration of particles in the streamwise and wall-normal directions showed qualitative relations with the wall-normal variations of $\partial\langle uv\rangle/\partial y$ and $\partial\langle v^2\rangle/\partial y$, respectively. Close to the wall at $y^+ < 20$, particles decelerated on average in the streamwise direction under the effect of viscous forces and their dynamics was dominated by the particles with sweep motions toward the wall which had the largest streamwise deceleration. Further away from the wall at $y^+ > 20$, particles accelerated in the streamwise acceleration under the effect of inertial forces. The streamwise acceleration of particles in the

buffer layer was dominated by the particles with ejection motions and peaked at $y^+ \sim 30$. At a further distance from the wall, the mean streamwise acceleration of particles gradually attenuated and the positive streamwise acceleration of the particles moving away from the wall was balanced by the negative streamwise acceleration of the particles moving towards the wall. The wall-normal acceleration of the particles at $y^+ < 20$ was positive under the effect of the drag force applied on them by ejection motions and the near-wall lift forces. This indicated that close to the wall on average the resultant force acting on the particles pushed them away from the wall. Farther from the wall the gravity became dominant and particles had negative wall-normal acceleration toward the wall. Investigation of the trajectory of particles that collided with the wall showed the longer average wall interaction time and larger e_V for the particles with a small impact angle (less than 1.5°). The interaction time and e_V of the colliding particles reduced by increasing their impact angle.

With increasing Re_τ from 410 to 765, the mean streamwise deceleration of G-125 particles near the wall and their mean streamwise acceleration in the log-layer became larger. The near-wall wall-normal acceleration of particles also increased by increasing Re_τ. The pdfs of A_x/a_x, A_y/a_y, and A_z/a_z were independent of Re_τ away from the wall but close to the wall at $y/H = 0.008$, increasing Re_τ narrowed these pdfs and reduced their values. This effect was more significant for the pdf of A_x/a_x. The Lagrangian velocity and acceleration time scales of particles were also reduced in all directions by increasing Re_τ. The investigation of the trajectory of the particles that interacted with each other showed that increasing Re_τ increased particles' relative velocity while it reduced the PPI rate close to the wall and increased it away from the wall, similar to its effect on the particle number density. The analysis of the trajectory of particles that collided with the wall showed that the impact velocity of particles became larger in all directions by increasing Re_τ while the number of collisions with large impact angle reduced. However, increasing Re_τ did not change the most frequent impact angle of the particles.

With increasing C_v from 0.03% to 0.15%, the mean acceleration of particles reduced in the streamwise direction and increased in the wall-normal direction. The pdfs of A_x/a_x,

A_y/a_y, and A_z/a_z were also independent of C_v away from the wall. Close to the wall at $y/H = 0.008$, the pdfs of A_x/a_x, A_z/a_y did not depend on C_v, however, the pdf of A_y/a_y that became wider by increasing C_v. The Lagrangian velocity and acceleration time scales of particles in all directions were also smaller at the higher C_v. By increasing C_v, the PPI rate was decreased close to the wall and increased away from it. The relative velocity of particles was also higher at the higher C_v. The effect of C_v of the particles relative velocity was reduced by increasing the distance from the wall. The collision of particles with large impact angle with the wall was slightly increased at the higher C_v.

Comparison of the near-wall motion of spherical glass particles (G-250) and non-spherical quartz particles (Q-250) with an almost equal equivalent diameter at $Re_\tau = 770$ and $C_v = 0.01\%$ showed that next to the wall the Q-250 particles had larger number density, mean streamwise velocity, mean streamwise deceleration, and mean wall-normal acceleration. The comparison of PWI characteristics of G-250 and Q-250 particles indicated that Q-250 particles lose less kinetic in the streamwise and wall-normal directions when they interact with the wall.

The effect of particle size on the motion of spherical glass particles with different sizes (G-125, G-250, and G-420 particles) was investigated at $Re_\tau = 770$ and $C_v = 0.01\%$. Results showed that bigger particles had greater mean streamwise velocity next to the wall and smaller streamwise and wall-normal velocity fluctuation. Their streamwise and wall-normal acceleration were also smaller than the smaller particles due to their larger inertia. Bigger particles also had larger impact velocity and smaller momentum loss in the streamwise direction during PWI. However, their wall-normal momentum loss during PWI was larger than the smaller particles.

Investigation of the motion of spherical glass particles (G-250) in drag-reduced turbulent polymeric flow with 66% drag reduction with respect to turbulent water flow with a similar mass flow rate showed that the polymer solution reduced the number density of particles near the channel lower wall and distributed them more evenly in the wall-normal direction. The polymer solution also reduced the mean streamwise velocity of particles close to the

wall and increased it away from the wall. The mean wall-normal velocity of particles was also smaller in the polymeric flow and their trajectories were more aligned with the wall. The polymer solution reduced the momentum of particles in the immediate vicinity of the wall by about 60%. The streamwise fluctuation of particles in the drag-reduced flow was similar to that in the water flow but their wall-normal fluctuation was significantly lower than that in the water flow. The reduction of the particle number density, their trajectory angle with respect to the wall, and their momentum in the vicinity of the wall in the drag-reducing flow showed the potential of polymer solutions for erosion wear reduction in slurry pipes.

9.2 Recommendations for future studies

This thesis provided fundamental information about the dynamics of inertial particles near the wall in turbulent flows and the effect of fluid and particle characteristics on it. However, due to the complex nature of particle-laden turbulent flows, there is still a long way to go to obtain a comprehensive understanding of particle dynamics in these flows and overcome the erosive wear challenge in the slurry pipelines. Experimental studies have an important role in this way to shed light on the complex dynamics of particles in particle-laden turbulent flows and reveal the effect of determinant factors. In this regard, three recommendations are provided below to advance the studies performed in this thesis and fill the gap between outcomes of this research and the needs of the related industries.

9.2.1 Instantaneous measurement of the forces applied on particles near the wall

In this thesis, the near-wall dynamics of inertial particles was investigated by measuring their acceleration through Lagrangian particle tracking. Knowing the particles Lagrangian acceleration tells us about the magnitude and the direction of the instantaneous resultant force acting on the particle. However, the value of the individual forces acting on the particles such as the lift, drag, and Basset forces cannot be measured by Lagrangian tracking of the particles only. To determine these forces, the simultaneous measurement of the

velocity of particles and their surrounding fluid is required that can be performed by adding tracers to particle-laden flows and simultaneously tracking the particles and the tracers around them. Based on the velocity of tracers around each particle and their distance to the center of the particle, one can interpolate the velocity of the fluid at the center of the particle (Traugott and Liberzon, 2017). Having the Lagrangian velocity of the particles and the fluid at the location of the particles, all the terms of the Maxey–Riley equation (Equation 2.15) can be determined and the accuracy of this equation can be verified for different experimental conditions.

9.2.2 Investigation of particles motion at higher concentrations

To detect the Lagrangian trajectory of particles over a longer time and with higher accuracy, the particle-laden experiments of this thesis were performed at very low C_v. For 2D-LPT measurement system with conventional illumination, increasing C_v caused the blockage of the reflected light from the particles and the line-of-sight of the camera. For 2D-LPT measurement system with back-light illumination, a larger number of particles could block the background light and reduction of the contrast required for detecting the boundary of particles. Although using the 3D-LPT measurement system along with STB algorithm allowed for the accurate tracking of a larger number of particles compared to a 2D-LPT system, increasing C_v could reduce the accuracy of this system (Schanz et al., 2016). The order of industrial concentrations of particles in slurry pipes is significantly higher than the concentrations tested in this study. To investigate particles motion in dense particle-laden flows one can use a large number of particles that their refractive index is matched with the carrier fluid along with a few particles with a different refractive index than the fluid. With this technique, Nouri et al. (1987) could measure the velocity of the carrier phase (using tracers) in a particle-laden flow with $C_v = 14\%$.

9.2.3 Characterization of the effect of particle shape on its motion near the wall

It was experimentally proved in this thesis that the shape of particles affects their near-wall dynamics and their collision with the wall. The non-spherical particles that were used in this research had irregular shapes. To characterize the effect of particle shape on its motion in turbulent flows and its collision with the wall, a systematic experimental study of the motion of regularly-shaped particles is necessary. Investigation of the rotational motion of particles was one the objectives of the study that was presented in Chapter 7 of this thesis. This objective was not achieved since it was not possible to accurately follow the major (or minor) axis of the irregularly-shaped particles between two consecutive images. Using regularly-shaped particles such as ellipsoid, disc, and fiber particles, one can improve the process to detect and follow the major axis of particles and determine their rotation. Moreover, the effect of particle shape on the lift and drag forces and the torque on the particles can be studied using the method explained in Section 9.2.1. Results of an experimental investigation of the motion of regularly-shaped particles can be used to validate the numerical simulations (e.g. van Wachem et al. 2015; Zarghami and Padding 2018) and predict the behavior of non-spherical particles with different shapes.

References

J. Abrahamson. Collision rates of small particles in a vigorously turbulent fluid. *Chem. Engng Sci.*, 30(11):1371–1379, 1975.

F. Ahmadi, M. Ebrahimian, R. S. Sanders, and S. Ghaemi. Particle image and tracking velocimetry of solid-liquid turbulence in a horizontal channel flow. *Intl. J. Multiphase Flow*, 112:83–99, 2019.

T. Alam, A. Islam, and Z. N. Farhat. Slurry erosion of pipeline steel: effect of velocity and microstructure. *J. Tribology*, 138(2), 2016.

A. Aliseda, A. Cartellier, F. Hainaux, and J. C. Lasheras. Effect of preferential concentration on the settling velocity of heavy particles in homogeneous isotropic turbulence. *J. Fluid Mech.*, 468:77–105, 2002.

A. M. Ardekani and R. H. Rangel. Numerical investigation of particle–particle and particle–wall collisions in a viscous fluid. *J. Fluid Mech.*, 596:437–466, 2008.

A. M. Ardekani, D. D. Joseph, D. Dunn-Rankin, and R. H. Rangel. Particle-wall collision in a viscoelastic fluid. *J. Fluid Mech.*, 633:475–483, 2009.

S. K. Arnipally and E. Kuru. Settling velocity of particles in viscoelastic fluids: a comparison of the shear viscosity vs elasticity effect. *SPE J*, 23, 2017. doi: 10.2118/187255-PA.

T. J. Atherton and D. J. Kerbyson. Size invariant circle detection. *Image Vision Comput*, 17(11):795–803, 1999.

T. R. Auton, J. C. R. Hunt, and M. Prud'Homme. The faxén formulae for a rigid sphere in an unsteady non-uniform stokes flow. *J. Méc. Théor. Appl.*, 1:143–160, 1983.

T. R. Auton, J. C. R. Hunt, and M. Prud'Homme. The force exerted on a body in inviscid unsteady non-uniform rotational flow. *J. Fluid Mech.*, 197:241–257, 1988.

S. Ayyalasomayajula, A. Gylfason, L. R. Collins, E. Bodenschatz, and Z. Warhaft. Lagrangian measurements of inertial particle accelerations in grid generated wind tunnel turbulence. *Phys. Rev. Lett.*, 97(14):144507, 2006.

S. Ayyalasomayajula, Z. Warhaft, and L. R. Collins. Modeling inertial particle acceleration statistics in isotropic turbulence. *Phys. Fluids*, 20(9):095104, 2008.

S. Bailey, M. Vallikivi, M. Hultmark, and A. Smits. Estimating the value of von kármán's constant in turbulent pipe flow. *J Fluid Mech*, 749:79–98, 2014.

L. Baker, A. Frankel, A. Mani, and F. Coletti. Coherent clusters of inertial particles in homogeneous turbulence. *J. Fluid Mech.*, 833:364–398, 2017.

D. Barros, B. Hiltbrand, and E. K. Longmire. Measurement of the translation and rotation of a sphere in fluid flow. *Exp. Fluids*, 59(6):104, 2018.

A. B. Basset. *A treatise on hydrodynamics: with numerous examples*, volume 2. Deighton, Bell and Company, 1888.

J. Bec, L. Biferale, G. Boffetta, A. Celani, M. Cencini, A. Lanotte, S. Musacchio, and F. Toschi. Acceleration statistics of heavy particles in turbulence. *J. Fluid Mech.*, 550: 349–358, 2006.

J. Borée and N. Caraman. Dilute bidispersed tube flow: Role of interclass collisions at increased loadings. *Phys. Fluids*, 17(5):055108, 2005.

J. Boussinesq. *Théorie analytique de la chaleur mise en harmonie avec la thermodynamique et avec la théorie mécanique de la lumiére*, volume 2. Gauthier-Villars, 1903.

H. Brenner. The stokes resistance of an arbitrary particle—iv arbitrary fields of flow. *Chem. Eng. Sci.*, 19(10):703–727, 1964.

E. Calzavarini, R. Volk, M. Bourgoin, E. Lévêque, J. F. Pinton, and F. Toschi. Acceleration statistics of finite-sized particles in turbulent flow: the role of faxén forces. *J. Fluid Mech.*, 630:179–189, 2009.

E. Calzavarini, R. Volk, E. Lévêque, J.-F. Pinton, and F. Toschi. Impact of trailing wake drag on the statistical properties and dynamics of finite-sized particle in turbulence. *Physica D*, 241(3):237–244, 2012.

Y. A. Çencel and J. M. Cimbala. Fluid mechanics–fundamentals and applications. 2006.

M. Cencini, J. Bec, L. Biferale, G. Boffetta, A. Celani, A. S. Lanotte, S. Musacchio, and F. Toschi. Dynamics and statistics of heavy particles in turbulent flows. *J. Turbul.*, (7): N36, 2006.

N. R. Challabotla, L. Zhao, and H. I. Andersson. Orientation and rotation of inertial disk particles in wall turbulence. *J. Fluid Mech.*, 766, 2015.

L. Chen, S. Coleman, J. Vassilicos, and Z. Hu. Acceleration in turbulent channel flow. *J. Turbul*, (11):N41, 2010.

P. Cherukat and J. B. McLaughlin. The inertial lift on a rigid sphere in a linear shear flow field near a flat wall. *J. Fluid Mech.*, 263:1–18, 1994.

R. Chhabra. *Bubbles, drops, and particles in non-Newtonian fluids*. CRC press, 2006.

R. Chhabra and J. Richardson. *Non-Newtonian flow in the process industries*. Butterworth-Heinemann, 1999.

A. Ciftlik, M. Ettori, and M. Gijs. High throughput-per-footprint inertial focusing. *Small*, 9(16):2764–2773, 2013.

F. Corredor, M. Bizhani, and E. Kuru. Experimental investigation of drag reducing fluid flow in annular geometry using particle image velocimetry technique. *J Fluids Eng*, 137 (8):081103, 2015.

S. Corrsin and J. Lumley. On the equation of motion for a particle in turbulent fluid. *Applied Scientific Research*, 6(2):114–116, 1956.

P. Costa, F. Picano, L. Brandt, and W. Breugem. Effects of the finite particle size in turbulent wall-bounded flows of dense suspensions. *J. Fluid Mech.*, 843:450–478, 2018.

P. Costa, L. Brandt, and F. Picano. Interface-resolved simulations of small inertial particles in turbulent channel flow. *J. Fluid Mech.*, 883:A54, 2020.

J. M. Coulson, J. F. Richardson, J. R. Backhurst, and J. H. Harker. *Chemical Engineering: Fluid flow, heat transfer and mass transfer*, volume 1. Butterworth-Heinemann, 1999.

C. Crowe, J. Schwarzkopf, M. Sommerfeld, and Y. Tsuji. *Multiphase flows with droplets and particles*. CRC Press, 2012.

A. Daitche. On the role of the history force for inertial particles in turbulence. *J. Fluid Mech.*, 782:567–593, 2015.

G. D'Avino and P. Maffettone. Particle dynamics in viscoelastic liquids. *J Non-Newton Fluid*, 215:80–104, 2015.

G. D'Avino, G. Romeo, M. Villone, F. Greco, P. Netti, and P. Maffettone. Single line particle focusing induced by viscoelasticity of the suspending liquid: theory, experiments and simulations to design a micropipe flow-focuser. *Lab on a Chip*, 12(9):1638–1645, 2012.

F. Del Giudice, G. Romeo, G. D'Avino, F. Greco, P. A. Netti, and P. Maffettone. Particle alignment in a viscoelastic liquid flowing in a square-shaped microchannel. *Lab on a Chip*, 13(21):4263–4271, 2013.

D. Di Carlo, D. Irimia, R. Tompkins, and M. Toner. Continuous inertial focusing, ordering, and separation of particles in microchannels. *P Natl A Sci USA*, 104(48):18892–18897, 2007.

D. A. Drew and S. Passman. *Theory of multicomponent fluids*. Springer, 2006.

Y. Dubief, C. White, V. Terrapon, E. Shaqfeh, P. Moin, and S. Lele. On the coherent drag-reducing and turbulence-enhancing behaviour of polymers in wall flows. *J Fluid Mech*, 514:271–280, 2004.

Y. Dubief, V. Terrapon, C. White, E. Shaqfeh, P. Moin, and S. Lele. New answers on the interaction between polymers and vortices in turbulent flows. *Flow Turb Combust*, 74(4): 311–329, 2005.

J. K. Eaton and J. Fessler. Preferential concentration of particles by turbulence. *Intl J. Multiphase Flow*, 20:169–209, 1994.

M. Ebrahimian, R. S. Sanders, and S. Ghaemi. Dynamics and wall collision of inertial particles in a solid–liquid turbulent channel flow. *J. Fluid Mech.*, 881:872–905, 2019.

S. Elghobashi. On predicting particle-laden turbulent flows. *Appl. Sci. Res.*, 52(4):309–329, 1994.

G. E. Elsinga, F. Scarano, B. Wieneke, and B. W. Van Oudheusden. Tomographic particle image velocimetry. *Exp. Fluids*, 41(6):933–947, 2006.

E. Falcon, C. Laroche, S. Fauve, and C. Coste. Behavior of one inelastic ball bouncing repeatedly off the ground. *The European Physical Journal B-Condensed Matter and Complex Systems*, 3(1):45–57, 1998.

H. Faxén. Der widerstand gegen die bewegung einer starren kugel in einer zähen flüssigkeit, die zwischen zwei parallelen ebenen wänden eingeschlossen ist. *Annalen der Physik*, 373 (10):89–119, 1922.

J. Feng, H. H. Hu, and D. D. Joseph. Direct simulation of initial value problems for the motion of solid bodies in a newtonian fluid. part 2. couette and poiseuille flows. *J. Fluid Mech.*, 277:271–301, 1994.

K. O. Fong, O. Amili, and F. Coletti. Velocity and spatial distribution of inertial particles in a turbulent channel flow. *J. Fluid Mech.*, 872:367–406, 2019.

N. A. Fuchs. *The mechanics of aerosols*. Pergamon press, 1964.

M. Gad-el Hak and P. R. Bandyopadhyay. Reynolds number effects in wall-bounded turbulent flows. *Appl. Mech. Rev.*, 47(8):307–365, 1994.

G. H. Ganser. A rational approach to drag prediction of spherical and nonspherical particles. *Powder Technol.*, 77(2):143–152, 1993.

F. Gauthier, H. Goldsmith, and S. Mason. Particle motions in non-newtonian media. II. Poiseuille flow. *T Soc Rheol*, 15(2):297–330, 1971.

S. Gerashchenko, N. S. Sharp, S. Neuscamman, and Z. Warhaft. Lagrangian measurements of inertial particle accelerations in a turbulent boundary layer. *J. Fluid Mech.*, 617: 255–281, 2008.

S. Gesemann, F. Huhn, D. Schanz, and A. Schröder. From noisy particle tracks to velocity, acceleration and pressure fields using b-splines and penalties. In *18th International Symposium on the Applications of Laser and Imaging Techniques to Fluid Mechanics (Lisbon, Portugal, 4-–7 July)*. Springer Verlag, 2016.

S. Ghaemi and F. Scarano. Multi-pass light amplification for tomographic particle image velocimetry applications. *Meas. Sci. Technol.*, 21(12):127002, 2010.

P. Gondret, M. Lance, and L. Petit. Bouncing motion of spherical particles in fluids. *Phys. Fluids*, 14(2):643–652, 2002.

P. S. Goswami and V. Kumaran. Particle dynamics in a turbulent particle–gas suspension at high stokes number. part 1. velocity and acceleration distributions. *J. Fluid Mech.*, 646:59–90, 2010.

R. Gupta, S. Singh, and V. Sehadri. Prediction of uneven wear in a slurry pipeline on the basis of measurements in a pot tester. *Wear*, 184(2):169–178, 1995.

E. Hatschek. An introduction to industrial rheology. by GW Scott Blair. *J Phys Chem*, 43 (3):395–395, 1939.

G. Hetsroni. Particles-turbulence interaction. *Intl J. Multiphase Flow*, 15(5):735–746, 1989.

W. C. Hinds. *Aerosol technology: properties, behavior, and measurement of airborne particles*. John Wiley & Sons, 1999.

S. Hoyas and J. Jiménez. Reynolds number effects on the Reynolds-stress budgets in turbulent channels. *Phys Fluids*, 20(10):101511, 2008.

P. Y. Huang, J. Feng, H. H. Hu, and D. D. Joseph. Direct simulation of the motion of solid particles in couette and poiseuille flows of viscoelastic fluids. *J Fluid Mech*, 343:73–94, 1997.

P. J. Ireland, A. D. Bragg, and L. R. Collins. The effect of reynolds number on inertial particle dynamics in isotropic turbulence. part 1. simulations without gravitational effects. *J. Fluid Mech.*, 796:617–658, 2016a.

P. J. Ireland, A. D. Bragg, and L. R. Collins. The effect of reynolds number on inertial particle dynamics in isotropic turbulence. part 2. simulations with gravitational effects. *J. Fluid Mech.*, 796:659–711, 2016b.

K. Iwamoto, Y. Suzuki, and N. Kasagi. Reynolds number effect on wall turbulence: toward effective feedback control. *Int J Heat Fluid Flow*, 23(5):678–689, 2002.

S. Jain, S. Somasundaram, and T. N. C. Anand. A fluorescent laser-diffuser arrangement for uniform backlighting. *Meas. Sci. Technol.*, 27(2):025406, 2016.

G. B. Jeffery. The motion of ellipsoidal particles immersed in a viscous fluid. *Proceedings of the Royal Society of London. Series A, Containing papers of a mathematical and physical character*, 102(715):161–179, 1922.

B. R. Jennings and K. Parslow. Particle size measurement: the equivalent spherical diameter. volume 419, pages 137–149. The Royal Society London, 1988.

G. G. Joseph and M. L. Hunt. Oblique particle–wall collisions in a liquid. *J. Fluid Mech.*, 510:71–93, 2004.

G. G. Joseph, R. Zenit, M. L. Hunt, and A. M. Rosenwinkel. Particle–wall collisions in a viscous fluid. *J. Fluid Mech.*, 433:329–346, 2001.

D. Kaftori, G. Hetsroni, and S. Banerjee. Particle behavior in the turbulent boundary layer. I. motion, deposition, and entrainment. *Physics of Fluids*, 7(5):1095–1106, 1995a.

D. Kaftori, G. Hetsroni, and S. Banerjee. Particle behavior in the turbulent boundary layer. II. velocity and distribution profiles. *Phys Fluids*, 7(5):1107–1121, 1995b.

C. J. Kähler, S. Scharnowski, and C. Cierpka. On the uncertainty of digital PIV and PTV near walls. *Exp Fluids*, 52(6):1641–1656, 2012.

K. Kang, S. S. Lee, K. Hyun, S. J. Lee, and J. M. Kim. DNA-based highly tunable particle focuser. *Nat Commun*, 4:2567, 2013.

A. J. Karabelas. An experimental study of pipe erosion by turbulent slurry flow. *Proc. HT5*, pages 47–61, 1978.

G. E. Karniadakis and K. Choi. Mechanisms on transverse motions in turbulent wall flows. *Annu Rev Fluid Mech*, 35(1):45–62, 2003.

A. Karnis and S. G. Mason. Particle motions in sheared suspensions. xix. viscoelastic media. *T Soc Rheol*, 10(2):571–592, 1966.

M. H. Kasbaoui, D. L. Koch, and O. Desjardins. The rapid distortion of two-way coupled particle-laden turbulence. *J. Fluid Mech.*, 877:82–104, 2019.

D. Kaushal, K. Sato, T. Toyota, K. Funatsu, and Y. Tomita. Effect of particle size distribution on pressure drop and concentration profile in pipeline flow of highly concentrated slurry. *Int J Multiphase Flow*, 31(7):809–823, 2005.

K. T. Kiger and C. Pan. Suspension and turbulence modification effects of solid particulates on a horizontal turbulent channel flow. *J. Turbulence*, 3(19):1–17, 2002.

I. Kim, S. Elghobashi, and W. A. Sirignano. On the equation for spherical-particle motion: effect of reynolds and acceleration numbers. *J. Fluid Mech.*, 367:221–253, 1998.

J. Kim. On the structure of pressure fluctuations in simulated turbulent channel flow. *J. Fluid Mech.*, 205:421–451, 1989.

J. Kim and S. Balachandar. Mean and fluctuating components of drag and lift forces on an isolated finite-sized particle in turbulence. *Theor. Comput. Fluid Dyn.*, 26:185–204, 01 2012. doi: 10.1007/s00162-010-0219-1.

J. Kim, P. Moin, and R. Moser. Turbulence statistics in fully developed channel flow at low reynolds number. *J. Fluid Mech.*, 177:133–166, 1987.

K. Kim, C.-F. Li, R. Sureshkumar, S. Balachandar, and R. J. Adrian. Effects of polymer stresses on eddy structures in drag-reduced turbulent channel flow. *J Fluid Mech*, 584: 281–299, 2007.

A. N. Kolmogorov. Energy dissipation in locally isotropic turbulence. In *Dokl. Akad. Nauk. SSSR*, volume 32, pages 19–21, 1941a.

A. N. Kolmogorov. The local structure of turbulence in incompressible viscous fluid for very large reynolds numbers. *Dokl. Akad. Nauk. SSSR*, 30:301–305, 1941b.

T. H. Kosel. Solid particle erosion. *ASM handbook*, 18:199–213, 1992.

P. Kosinski and A. C. Hoffmann. Extension of the hard-sphere particle-wall collision model to account for particle deposition. *Phys. Rev. E*, 79(6):061302, 2009.

J. D. Kulick, J. R. Fessler, and J. K. Eaton. Particle response and turbulence modification in fully developed channel flow. *J. Fluid Mech.*, 277:109–134, 1994.

J. Kussin and M. Sommerfeld. Experimental studies on particle behaviour and turbulence modification in horizontal channel flow with different wall roughness. *Exp. Fluids*, 33(1): 143–159, 2002.

S. Laín, M. Sommerfeld, and J. Kussin. Experimental studies and modelling of four-way coupling in particle-laden horizontal channel flow. *Intl. J. Heat Fluid flow*, 23(5):647–656, 2002.

V. Lavezzo, A. Soldati, S. Gerashchenko, Z. Warhaft, and L. R. Collins. On the role of gravity and shear on inertial particle accelerations in near-wall turbulence. *J. Fluid Mech.*, 658:229–246, 2010.

C. Lee, K. Yeo, and J. I. Choi. Intermittent nature of acceleration in near wall turbulence. *Phys. Rev. Lett.*, 92(14):144502, 2004.

J. Lee and C. Lee. The effect of wall-normal gravity on particle-laden near-wall turbulence. *J. Fluid Mech.*, 873:475–507, 2019.

S. Lee and C. Lee. Intermittency of acceleration in isotropic turbulence. *Phys. Rev. E*, 71 (5):056310, 2005.

D. Legendre, R. Zenit, C. Daniel, and P. Guiraud. A note on the modelling of the bouncing of spherical drops or solid spheres on a wall in viscous fluid. *Chem. Engng Sci.*, 61(11): 3543–3549, 2006.

J. Lelouvetel, F. Bigillon, D. Doppler, I. Vinkovic, and J. Y. Champagne. Experimental investigation of ejections and sweeps involved in particle suspension. *Water Resources Research*, 45(2), 2009.

A. M. Leshansky, A. Bransky, N. Korin, and U. Dinnar. Tunable nonlinear viscoelastic focusing in a microfluidic device. *Phys Rev Lett*, 98(23):234501, 2007.

G. Li, G. H. McKinley, and A. M. Ardekani. Dynamics of particle migration in channel flow of viscoelastic fluids. *J Fluid Mech*, 785:486–505, 2015.

J. Li, H. Wang, Z. Liu, S. Chen, and C. Zheng. An experimental study on turbulence modification in the near-wall boundary layer of a dilute gas-particle channel flow. *Experiments in fluids*, 53(5):1385–1403, 2012.

Z. Li, J. Wei, and B. Yu. Direct numerical study on effect of interparticle collision in particle-laden turbulence. *AIAA*, pages 3212–3222, 2016.

E. J. Lim, T. J. Ober, J. F. Edd, S. P. Desai, D. Neal, K. W. Bong, P. S. Doyle, G. H. McKinley, and M. Toner. Inertio-elastic focusing of bioparticles in microchannels at high throughput. *Nature Commun*, 5:4120, 2014.

J. H. Lin and K. C. Chang. Particle dispersion simulation in turbulent flow due to particle-particle and particle-wall collisions. *J. Mech.*, 32(2):237–244, 2016.

T. S. Luchik and W. G. Tiederman. Turbulent structure in low-concentration drag-reducing channel flows. *J Fluid Mech*, 190:241–263, 1988.

N. Lukerchenko, Y. Kvurt, Z. Chara, and P. Vlasak. Collision of a rotating spherical particle with flat wall in liquid. *Engineering Mechanics*, page 306, 2012.

K. Luo, C. Hu, F. Wu, and J. Fan. Direct numerical simulation of turbulent boundary layer with fully resolved particles at low volume fraction. *Phys. Fluids*, 29(5):053301, 2017.

C. Marchioli and A. Soldati. Mechanisms for particle transfer and segregation in a turbulent boundary layer. *J. Fluid Mech.*, 468:283–315, 2002.

C. Marchioli and A. Soldati. Rotation statistics of fibers in wall shear turbulence. *Acta Mechanica*, 224(10):2311–2329, 2013.

C. Marchioli, A. Soldati, J. G. M. Kuerten, B. Arcen, A. Taniere, G. Goldensoph, K. D. Squires, M. F. Cargnelutti, and L. M. Portela. Statistics of particle dispersion in direct numerical simulations of wall-bounded turbulence: Results of an international collaborative benchmark test. *Intl. J. Multiphase Flow*, 34(9):879–893, 2008.

M. R. Maxey and J. J. Riley. Equation of motion for a small rigid sphere in a nonuniform flow. *Phys. Fluids*, 26(4):883–889, 1983.

G. H. McKinley. Steady and transient motion of spherical particles in viscoelastic liquids. In D. D. Kee and R. P. Chhabra, editors, *Transport Processes in Bubble, Drops, and Particles*, pages 338–375. New York: Taylor & Francis, 2002.

M. Mehrabadi, J. A. K. Horwitz, S. Subramaniam, and A. Mani. A direct comparison of particle-resolved and point-particle methods in decaying turbulence. *J. Fluid Mech.*, 850: 336–369, 2018.

R. Mei and R. J. Adrian. Flow past a sphere with an oscillation in the free-stream velocity and unsteady drag at finite reynolds number. *J. Fluid Mech.*, 237:323–341, 1992.

R. Mei, C. J. Lawrence, and R. J. Adrian. Unsteady drag on a sphere at finite reynolds number with small fluctuations in the free-stream velocity. *J. Fluid Mech.*, 233:613–631, 1991.

Y. Meller and A. Liberzon. Particle–fluid interaction forces as the source of acceleration pdf invariance in particle size. *Intl J. Multiphase Flow*, 76:22–31, 2015.

A. A. Mishra S, Chandra H. Solid liquid non-Newtonian fluid flow in pipe: a review. *Acta Mech Slovaca*, 16(2):62–73, 2012.

M. Mohammadtabar, R. S. Sanders, and S. Ghaemi. Turbulent structures of non-newtonian solutions containing rigid polymers. *Phys Fluids*, 29(10):103101, 2017.

W. A. M. Morgado and I. Oppenheim. Energy dissipation for quasielastic granular particle collisions. *Phys Rev E*, 55:1940–1945, Feb 1997. doi: 10.1103/PhysRevE.55.1940.

R. D. Moser, J. Kim, and N. N. Mansour. Direct numerical simulation of turbulent channel flow up to re τ= 590. *Phys. fluids*, 11(4):943–945, 1999.

H. Nasr and G. Ahmadi. The effect of two-way coupling and inter-particle collisions on turbulence modulation in a vertical channel flow. *Intl J. Heat Fluid Flow*, 28(6):1507–1517, 2007.

A. Neville, F. Reza, et al. Erosion-corrosion of cast white irons for application in the oilsands industry. In *CORROSION 2007*. NACE International, 2007.

Y. Q. Nguyen and J. C. Wells. Effects of surface roughness on rebound strength in particle-wall collisions in air and liquids. In *ASME 2005 Fluids Engineering Division Summer Meeting*, pages 937–942. American Society of Mechanical Engineers, 2005.

Y. Ninto and M. H. Garcia. Experiments on particle—turbulence interactions in the near–wall region of an open channel flow: implications for sediment transport. *J. Fluid Mech.*, 326:285–319, 1996.

J. M. Nouri, J. H. Whitelaw, and M. Yianneskis. Particle motion and turbulence in dense two-phase flows. *Intl. J. Multiphase Flow*, 13(6):729–739, 1987.

K. Ohmi and H. Li. Particle-tracking velocimetry with new algorithms. *Meas Sci Tech*, 11 (6):603, 2000.

P. C. Okonkwo, R. A. Shakoor, E. Ahmed, and A. M. A. Mohamed. Erosive wear performance of api x42 pipeline steel. *Eng. Failure Analysis*, 60:86–95, 2016.

C. W. Oseen. Recent methods and results in hydrodynamics. *Leipzig: Akademische Verlagsgesellschaft mb H.*, 1927.

R. Ouchene, M. Khalij, B. Arcen, and A. Tanière. A new set of correlations of drag, lift and torque coefficients for non-spherical particles and large reynolds numbers. *Powder Technol.*, 303:33–43, 2016.

L. L. Parent and D. Y. Li. Wear of hydrotransport lines in athabasca oil sands. *Wear*, 301 (1-2):477–482, 2013.

S. Parsa and G. A. Voth. Inertial range scaling in rotations of long rods in turbulence. *Phys. Rev. Lett.*, 112(2):024501, 2014.

S. Parsa, E. Calzavarini, F. Toschi, and G. A. Voth. Rotation rate of rods in turbulent fluid flow. *Phys. Rev. Lett.*, 109(13):134501, 2012.

S. Pedinotti, G. Mariotti, and S. Banerjee. Direct numerical simulation of particle behaviour in the wall region of turbulent flows in horizontal channels. *Int J of Multiphase Flow*, 18 (6):927–941, 1992.

C. Peskin. Flow patterns around heart valves: A numerical method. *J. Comput. Phys.*, 10 (2):252 – 271, 1972.

S. B. Pope. *Turbulent Flows*. Cambridge University Press, 2000. doi: 10.1017/CBO9780511840531.

I. Procaccia, V. S. L'vov, and R. Benzi. Colloquium: Theory of drag reduction by polymers in wall-bounded turbulence. *Rev Modern Phys*, 80(1):225, 2008.

N. M. Qureshi, M. Bourgoin, C. Baudet, A. Cartellier, and Y. Gagne. Turbulent transport of material particles: an experimental study of finite size effects. *Phys. Rev. Lett.*, 99(18): 184502, 2007.

N. M. Qureshi, U. Arrieta, C. Baudet, A. Cartellier, Y. Gagne, and M. Bourgoin. Acceleration statistics of inertial particles in turbulent flow. *The European Physical Journal B*, 66(4):531–536, 2008.

C. S. Ramesh, R. Keshavamurthy, B. H. Channabasappa, and S. Pramod. Influence of heat treatment on slurry erosive wear resistance of al6061 alloy. *Materials & Design*, 30(9): 3713–3722, 2009.

M. Righetti and G. P. Romano. Particle–fluid interactions in a plane near-wall turbulent flow. *J. Fluid Mech.*, 505:93–121, 2004.

H. Rouse. Modern conceptions of the mechanics of fluid turbulence. *T A Soc Civ Eng*, 102: 463—-554, 1937.

W. A. Rowin, R. S. Sanders, and S. Ghaemi. A recipe for optimum mixing of polymer drag reducers. *J Fluids Eng*, 140(11):111402, 2018.

S. I. Rubinow and J. B. Keller. The transverse force on a spinning sphere moving in a viscous fluid. *J. Fluid Mech.*, 11(3):447–459, 1961.

P. G. Saffman. The lift on a small sphere in a slow shear flow. *J. Fluid Mech.*, 22(2): 385–400, 1965.

P. G. F. Saffman and J. S. Turner. On the collision of drops in turbulent clouds. *J. Fluid Mech.*, 1(1):16–30, 1956.

J. P. L. C. Salazar and L. R. Collins. Inertial particle relative velocity statistics in homogeneous isotropic turbulence. *J. Fluid Mech.*, 696:45–66, 2012.

A. D. Salman, A. Verba, Z. Lukenics, and M. Szabo. Effects of impact velocity and angle on collision. *Periodica Polytechnica*, 35(1-2):43–51, 1989.

B. L. Sawford. Reynolds number effects in lagrangian stochastic models of turbulent dispersion. *Physics of Fluids A: Fluid Dynamics*, 3(6):1577–1586, 1991.

K. P. Schade and G. Wozniak. Experimental investigation of the particle-wall-impact under particular consideration of the wall surface influence on the particle trajectory and the transition between sliding and adhering impact. *PAMM*, 10(1):451–452, 2010.

D. Schanz, S. Gesemann, and A. Schröder. Shake-the-box: Lagrangian particle tracking at high particle image densities. *Exp. Fluids*, 57(5):70, Apr 2016. ISSN 1432-1114. doi: 10.1007/s00348-016-2157-1.

K. W. Seo, Y. J. Kang, and S. J. Lee. Lateral migration and focusing of microspheres in a microchannel flow of viscoelastic fluids. *Phys Fluids*, 26(6):063301, 2014.

X. Shao, T. Wu, and Z. Yu. Fully resolved numerical simulation of particle-laden turbulent flow in a horizontal channel at a low reynolds number. *J. Fluid Mech.*, 693:319–344, 2012.

R. Shokri, S. Ghaemi, D. S. Nobes, and R. S. Sanders. Investigation of particle-laden turbulent pipe flow at high-reynolds-number using particle image/tracking velocimetry (piv/ptv). *Intl J. Multiphase Flow*, 89:136–149, 2017.

A. Soldati. Particles turbulence interactions in boundary layers. *Z. Angew. Math. Mech. J. Appl. Math. Mech.*, 85(10):683–699, 2005.

A. Soldati and C. Marchioli. Physics and modelling of turbulent particle deposition and entrainment: Review of a systematic study. *Int J Multiphase Flow*, 35(9):827–839, 2009.

M. Sommerfeld. Modelling of particle-wall collisions in confined gas-particle flows. *Intl. J. Multiphase Flow*, 18(6):905–926, 1992.

M. Sommerfeld. Kinetic simulations for analysing the wall collision process of non-spherical particles. In *ASME 2002 Joint US-European Fluids Engineering Division Conference*, pages 539–547. American Society of Mechanical Engineers, 2002.

M. Sommerfeld. Analysis of collision effects for turbulent gas–particle flow in a horizontal channel: Part i. particle transport. *Intl. J. Multiphase Flow*, 29(4):675–699, 2003.

M. Sommerfeld and N. Huber. Experimental analysis and modelling of particle-wall collisions. *Intl J. multiphase flow*, 25(6-7):1457–1489, 1999.

M. Sommerfeld and S. Lain. Stochastic modelling for capturing the behaviour of irregular-shaped non-spherical particles in confined turbulent flows. *Powder Technol*, 332:253–264, 2018.

K. D. Squires and J. K. Eaton. Preferential concentration of particles by turbulence. *Phys. Fluids A: Fluid Dynamics*, 3(5):1169–1178, 1991.

N. Stelzenmuller, J. I. Polanco, L. Vignal, I. Vinkovic, and N. Mordant. Lagrangian acceleration statistics in a turbulent channel flow. *Phys. Rev. Fluids*, 2(5):054602, 2017.

A. Stocchino and M. Guala. Particle-wall collision in shear thinning fluids. *Exp. Fluids*, 38 (4):476–484, 2005.

G. G. Stokes. On the effect of the internal friction of fluids on the motion of pendulums. *Trans. Cambridge Phil. Soc.*, 9:8, 1851.

B. M. Sumer and R. Deigaard. Particle motions near the bottom in turbulent flow in an open channel. Part 2. *J Fluid Mech*, 109:311–337, 1981.

S. Sundaram and L. R. Collins. Collision statistics in an isotropic particle-laden turbulent suspension. part 1. direct numerical simulations. *J. Fluid Mech.*, 335:75–109, 1997.

M. Tanahashi, S.-J. Kang, T. Miyamoto, S. Shiokawa, and T. Miyauchi. Scaling law of fine scale eddies in turbulent channel flows up to $Re_\tau = 800$. *Intl. J. Heat Fluid Flow*, 25(3): 331–340, 2004.

A. Taniere, B. Oesterle, and J. C. Monnier. On the behaviour of solid particles in a horizontal boundary layer with turbulence and saltation effects. *Experiments in Fluids*, 23(6):463–471, 1997.

G. B. Tatterson. *Fluid mixing and gas dispersion in agitated tanks*. McGraw-Hill Companies, 1991.

G. I. Taylor. Diffusion by Continuous Movements. *Proceedings of the London Mathematical Society*, s2-20(1):196–212, 01 1921. ISSN 0024-6115. doi: 10.1112/plms/s2-20.1.196.

G. I. Taylor. Stability of a viscous liquid contained between two rotating cylinders. *Phil Trans R Soc London*, 223:289–343, 1923.

H. Tennekes and J. L. Lumley. *A first course in turbulence*. MIT press, 1972.

H. Traugott and A. Liberzon. Experimental study of forces on freely moving spherical particles during resuspension into turbulent flow. *Intl. J. Multiphase Flow*, 88:167–178, 2017.

Y. Tsuji, Y. Morikawa, T. Tanaka, N. Nakatsukasa, and M. Nakatani. Numerical simulation of gas-solid two-phase flow in a two-dimensional horizontal channel. *Intl J. Multiphase Flow*, 13(5):671–684, 1987.

M. Uhlmann. Interface-resolved direct numerical simulation of vertical particulate channel flow in the turbulent regime. *Phys. Fluids*, 20(5):053305, 2008.

B. van Wachem, M. Zastawny, F. Zhao, and G. Mallouppas. Modelling of gas–solid turbulent channel flow with non-spherical particles with large stokes numbers. *Intl. J. Multiphase Flow*, 68:80–92, 2015.

A. Y. Varaksin, Y. V. Polezhaev, and A. F. Polyakov. Effect of particle concentration on fluctuating velocity of the disperse phase for turbulent pipe flow. *Intl. J. Heat Fluid Flow*, 21(5):562–567, 2000.

R. Vinuesa, A. Noorani, A. Lozano-Durán, G. K. E. Khoury, P. Schlatter, P. F. Fischer, and H. M. Nagib. Aspect ratio effects in turbulent duct flows studied through direct numerical simulation. *J. Turbul.*, 15(10):677–706, 2014.

P. S. Virk, H. S. Mickley, and K. A. Smith. The ultimate asymptote and mean flow structure in toms' phenomenon. *J Appl Mech*, 37(2):488–493, 1970.

R. Volk, E. Calzavarini, G. Verhille, D. Lohse, N. Mordant, J. F. Pinton, and F. Toschi. Acceleration of heavy and light particles in turbulence: comparison between experiments and direct numerical simulations. *Physica D*, 237(14-17):2084–2089, 2008.

G. A. Voth, A. la Porta, A. M. Crawford, J. Alexander, and E. Bodenschatz. Measurement of particle accelerations in fully developed turbulence. *J. Fluid Mech.*, 469:121–160, 2002.

A. W. Vreman. Turbulence characteristics of particle-laden pipe flow. *J. Fluid Mech.*, 584: 235–279, 2007.

H. Wadell. Volume, shape, and roundness of rock particles. *J Geology*, 40(5):443–451, 1932.

H. Wadell. The coefficient of resistance as a function of reynolds number for solids of various shapes. *Journal of the Franklin Institute*, 217(4):459–490, 1934.

J. M. Wallace. Quadrant analysis in turbulence research: history and evolution. *Annu Rev Fluid Mech*, 48:131–158, 2016.

J. M. Wallace, H. Eckelmann, and R. S. Brodkey. The wall region in turbulent shear flow. *J. Fluid Mech.*, 54(1):39–48, 1972.

L. Wang, A. S. Wexler, and Y. Zhou. Statistical mechanical description and modelling of turbulent collision of inertial particles. *J. Fluid Mech.*, 415:117–153, 2000.

M. D. Warholic, H. Massah, and T. J. Hanratty. Influence of drag-reducing polymers on turbulence: effects of reynolds number, concentration and mixing. *Exp Fluids*, 27(5): 461–472, 1999.

M. D. Warholic, D. K. Heist, M. Katcher, and T. J. Hanratty. A study with particle-image velocimetry of the influence of drag-reducing polymers on the structure of turbulence. *Exp Fluids*, 31(5):474–483, 2001.

E. J. Wasp, J. P. Kenny, and R. L. Gandhi. Solid–liquid flow: slurry pipeline transportation. [pumps, valves, mechanical equipment, economics]. *Ser. Bulk Mater. Handl.; (USA)*, 1:4, 1 1977.

C. M. White and M. G. Mungal. Mechanics and prediction of turbulent drag reduction with polymer additives. *Annu Rev Fluid Mech*, 40:235–256, 2008.

C. M. White, V. S. R. Somandepalli, and M. G. Mungal. The turbulence structure of drag-reduced boundary layer flow. *Exp Fluids*, 36(1):62–69, 2004.

B. Wieneke. Volume self-calibration for 3d particle image velocimetry. *Exp. Fluids*, 45(4): 549–556, 2008.

B. Wieneke. Iterative reconstruction of volumetric particle distribution. *Meas. Sci. Technol.*, 24(2):024008, 2013.

N. Wiener. Extrapolation, interpolation, and smoothing of stationary time series, vol. 2, 1949.

Y. Yamamoto, M. Potthoff, T. Tanaka, T. Kajishima, and Y. Tsuji. Large-eddy simulation of turbulent gas–particle flow in a vertical channel: effect of considering inter-particle collisions. *J. Fluid Mech.*, 442:303–334, 2001.

S. Yang, J. Y. Kim, S. J. Lee, S. S. Lee, and J. M. Kim. Sheathless elasto-inertial particle focusing and continuous separation in a straight rectangular microchannel. *Lab on a Chip*, 11(2):266–273, 2011.

K. Yeo, B. G. Kim, and C. Lee. On the near-wall characteristics of acceleration in turbulence. *J. Fluid Mech.*, 659:405–419, 2010.

W. Yu, I. Vinkovic, and M. Buffat. Acceleration statistics of finite-size particles in turbulent channel flow in the absence of gravity. *Flow Turbul. Combust.*, 96(1):183–205, 2016.

Z. Yu, Z. Lin, X. Shao, and L. P. Wang. Effects of particle-fluid density ratio on the interactions between the turbulent channel flow and finite-size particles. *Phys. Rev. E*, 96(3):033102, 2017.

H. K. Yuen, J. Princen, J. Illingworth, and J. Kittler. Comparative study of Hough transform methods for circle finding. *Image Vision Comput*, 8(1):71–77, 1990.

S. Yuu. Collision rate of small particles in a homogeneous and isotropic turbulence. *AIChE journal*, 30(5):802–807, 1984.

L. I. Zaichik and V. M. Alipchenkov. Acceleration of heavy particles in isotropic turbulence. *Intl. J. Multiphase Flow*, 34(9):865–868, 2008.

R. Zamansky, I. Vinkovic, and M. Gorokhovski. Acceleration statistics of solid particles in turbulent channel flow. *Phys. Fluids*, 23(11):113304, 2011.

A. Zarghami and J. T. Padding. Drag, lift and torque acting on a two-dimensional non-spherical particle near a wall. *Adv. Powder Technol.*, 29(6):1507–1517, 2018.

M. Zastawny, G. Mallouppas, F. Zhao, and B. Van Wachem. Derivation of drag and lift force and torque coefficients for non-spherical particles in flows. *Intl. J. Multiphase Flow*, 39:227–239, 2012.

F. Zhao, W. K. George, and B. G. M. Van Wachem. Four-way coupled simulations of small particles in turbulent channel flow: The effects of particle shape and stokes number. *Phys. Fluids*, 27(8):083301, 2015.

L. Zhao, C. Marchioli, and H. I. Andersson. Slip velocity of rigid fibers in turbulent channel flow. *Phys. Fluids*, 26(6):063302, 2014.

L. H. Zhao, C. Marchioli, and H. I. Andersson. Stokes number effects on particle slip velocity in wall-bounded turbulence and implications for dispersion models. *Phys. Fluids*, 24(2): 021705, 2012.

J. Zheng and R. Hryciw. Traditional soil particle sphericity, roundness and surface roughness by computational geometry. *Géotechnique*, 65(6):494–506, 2015.